ΕΛΛΗΝΙΚΗ ΔΗΜΟΚΡΑΤΙΑ

ΠΑΝΕΠΙΣΤΗΜΙΟ ΙΩΑΝΝΙΝΩΝ

ΠΟΛΥΤΕΧΝΙΚΗ ΣΧΟΛΗ

ΤΜΗΜΑ ΜΗΧΑΝΙΚΩΝ ΕΠΙΣΤΗΜΗΣ ΥΛΙΚΩΝ

ΠΡΟΓΡΑΜΜΑ ΜΕΤΑΠΤΥΧΙΑΚΩΝ ΣΠΟΥΔΩΝ

«ΠΡΟΗΓΜΕΝΑ ΥΛΙΚΑ»

ΜΕΤΑΠΤΥΧΙΑΚΗ ΔΙΑΤΡΙΒΗ

Γρηγόριος Γρηγοριάδης

ΜΟΝΤΕΛΟΠΟΙΗΣΗ ΤΗΣ ΡΟΗΣ ΤΟΥ ΑΙΜΑΤΟΣ ΣΤΟΝ ΑΡΙΣΤΕΡΟ ΚΟΛΠΟ

ΙΩΑΝΝΙΝΑ, 2020

HELINIC REPUBLIC

UNIVERSITY OF IOANNINA

SCHOOL OF ENGINEERING

DEPARTMENT OF MATERIALS SCIENCE ENGINEERING

POSTGRADUATE PROGRAMME

"ADVANCED MATERIALS"

MASTER THESIS

Grigorios Grigoriadis

BLOOD FLOW MODELING AT THE LEFT ATRIUM

ΙΩΑΝΝΙΝΑ, 2020

Η παρούσα Μεταπτυχιακή Διατριβή εκπονήθηκε στο πλαίσιο των σπουδών για την απόκτηση του Μεταπτυχιακού Διπλώματος Ειδίκευσης στην εξειδίκευση:

“Βιοϋλικά και Βιοϊατρική Τεχνολογία”

που απονέμει το Τμήμα Μηχανικών Επιστήμης Υλικών του Πανεπιστημίου Ιωαννίνων.

Εγκρίθηκε την ……21/7/2020……..από την εξεταστική επιτροπή:

Καθ. Δημήτριος Ι. Φωτιάδης, Τμήμα Μηχανικών Επιστήμης Υλικών, Πολυτεχνική Σχολή, Πανεπιστήμιο Ιωαννίνων, **Επιβλέπων**.

Αναπληρώτρια Καθηγήτρια Αικατερίνη Κ. Νάκα, Τμήμα Ιατρικής σχολής, Σχολή Επιστημών Υγείας, Πανεπιστήμιο Ιωαννίνων.

Αναπληρωτής Καθηγητής Λεωνίδας Ν. Γεργίδης, Τμήμα Μηχανικών Επιστήμης Υλικών, Πολυτεχνική Σχολή, Πανεπιστήμιο Ιωαννίνων.

ΥΠΕΥΘΥΝΗ ΔΗΛΩΣΗ

"Δηλώνω υπεύθυνα ότι η παρούσα διατριβή εκπονήθηκε κάτω από τους διεθνείς ηθικούς και ακαδημαϊκούς κανόνες δεοντολογίας και προστασίας της πνευματικής ιδιοκτησίας. Σύμφωνα με τους κανόνες αυτούς, δεν έχω προβεί σε ιδιοποίηση ξένου επιστημονικού έργου και έχω πλήρως αναφέρει τις πηγές που χρησιμοποίησα στην εργασία αυτή."

(Υπογραφή υποψηφίου)

To my family

This master thesis is submitted to the Department of Materials Science and Engineering, University of Ioannina (UoI) for the master's degree (MSc) in technologies of Advanced Materials.

Acknowledgements

There are many people I would like to thank and that should be acknowledged for their contribution during my work.

Foremost, **my family** for the valuable support they have provided me through all these years.

My **supervisor Prof. Dimitrios I. Fotiadis** for giving me the opportunity to lead this research and explore the cardiovascular field through my master's thesis, his guidance and the confidence he showed me since my B.Sc. degree.

Dr. Ioanna Kosmidou from CRF for her guidance and **Dr. Christopher Ellis** from Vanderbilt University Medical Center for his collaboration to this research and of course for providing us the clinical data to develop this study.

I am also very grateful to **Dr. Antonis Sakellarios and Dr. Nikolaos** Tachos for their contribution and their mentorship during the all the time of this research.

Associate Professor Katerina K. Naka from the Medical School of University of Ioannina, for her decisive guidance and her appreciated support to me through this research.

Associate Professor Leonidas N. Gergidis for accepting to evaluate the work presented in this thesis.

During my master thesis I was employed as a junior researcher on the European Union's Horizon 2020 research and innovation programme SILICOFCM "In Silico trials for drug tracing the effects of sarcomeric protein mutations leading to familial cardiomyopathy" under grant agreement No 777204

Ioannina, July 2020

Grigoris Grigoriadis.

Abstract

The cardiovascular system is a complex system which performs inextinguishable powerful tasks essential for life. Many deaths from cardiovascular diseases would occur as the result of heart attack, coronary artery disease or stroke. Coronary heart disease and strokes have the highest mortality rate than any other disease. Moreover, the technological advancements in medical imaging technologies, have helped to detect both anatomical and physiological abnormalities. Detailed information about the cardiac functionality have become faster and more feasible, providing a variety of outcomes with functional and anatomical information. Although in this study we focus to use mostly blood flow patterns to investigate blood flow and CT images to obtain the computational domains.

At the upper left side of the heart the left atrium and left atrial appendage are interlinked cardiac cavities. The atrium is a structure with multiple inlets at the insertion of the pulmonary veins, a single outlet at the mitral valve orifice and the presence of the left atrium appendage, a highly complex blind-ended structure on the anterior-lateral wall of the left atrium whose anatomical shape is highly variable. The significance of the atrium and appendage in several clinical conditions, such as atrial fibrillation or valvular disease is critical. Studies have constituted the appendage as one of the most significant sources of cardioembolic events, predominantly in patients with atrial fibrillation but also in other types of cardiac dysfunctionalities.

In this thesis, we developed and analyzed 13 different patient-specific 3D anatomical models of the left atrium, which will be used to analyze the blood flow through In-silico simulations. The study of the blood's hemodynamic parameters will be able to shed light into atrium's and appendage's functionality. Specially we focused on appendage's impact on thrombus formation by implementing local hemodynamics at the left atrium and the left atrial appendage using computational fluid dynamics. The aim of this thesis is to describe a novel approach using computational fluid dynamics, to analyze/describe the hemodynamic behavior at the left atrium and left atrium appendage, according to different anatomical morphologies and fluid velocities. This thesis focuses to study the blood flow inside the atrium and the velocity distribution at the appendage cavity. A 3D semi-automated reconstruction approach used to segment and reconstruct left atrium 3D geometries and obtain the computational domain. This aspect of coupling computational fluid dynamics with medical imaging makes it possible to reconstruct patient-specific models. Cardiac computed tomography scans used from 13 different patients. The target is to obtain as much as possible reliable and accurate 3D models for reliable visual representations. We applied boundary conditions extracted from patients-specific clinical data. Mostly, velocity data used as inputs to parameterize the models and validate them. In-vitro patient-specific velocity data obtained from Transesophageal

Echocardiography (TEE) used, to be digitized and obtain the appropriate profiles. Five different velocity profiles simulated to each patient case, representing one normal condition and four abnormal. Simulations varied significantly according to left atrium Appendage. Wall Shear Stress (WSS) calculations were performed, in order to correlate the velocities with wall shear stress and the resulting thrombus formation inside the appendage cavity. A further goal of this thesis is to provide subject-specific models with potential effort to professional clinicians in decision-making.

Key words: Left Atrium (LA), Left Atrial Appendage (LAA), Blood Flow Modeling, Wall Shear Stress (WSS), CFD, Appendage Morphologies, Thrombus formation.

Περίληψη

Το καρδιαγγειακό σύστημα είναι ένα πολύπλοκο σύστημα που εκτελεί αδιάπαυστα απαιτητικά καθήκοντα απαραίτητα για την ζωή. Πολλοί θάνατοι ευθύνονται σε καρδιαγγειακές παθήσεις που προκύπτουν ως αποτέλεσμα καρδιακής προσβολής, στεφανιαίας νόσου ή εγκεφαλικού επεισοδίου. Η στεφανιαία νόσος και τα εγκεφαλικά επεισόδιά έχουν το υψηλότερο ποσοστό θνησιμότητας από οποιαδήποτε άλλη ασθένεια. Ωστόσο, οι τεχνολογικές εξελίξεις με εφαρμογή στην ιατρική, έχουν αναπτυχθεί ραγδαία με αποτέλεσμα την υποβοήθηση των κλινικών για ακριβέστερη διάγνωση. Πλέον είναι διαθέσιμες λεπτομερής απεικονιστικές τεχνικές, οι οποίες προσφέρουν πληροφορίες σχετικά με την καρδιακή λειτουργικότητα και την ανατομία.

Ο αριστερός κόλπος είναι μια δομή με πολλαπλές εισόδους (πνευμονικές φλέβες) και μια έξοδο (μιτροειδής βαλβίδα). Επίσης, προσκολλημένο στο πρόσθιο-πλευρικό τοίχωμα του αριστερού κόλπου βρίσκεται το αριστερό ωτίο, μια δύσμορφη κοιλότητα η οποία ευθύνεται για την δημιουργία θρόμβων. Ιδιαιτέρως έχει αποδειχθεί πως σε περιπτώσεις κολπικής μαρμαρυγής τα ποσοστά δημιουργίας θρόμβου αυξάνονται καθώς επηρεάζεται η συσταλτικότητα και η ροή του αίματος δυσχεραίνει.

Η παρούσα μεταπτυχιακή μελέτη εστιάζει στην ανάπτυξη ενός αλγορίθμου για την ημι-αυτόματη τμηματοποίηση του αριστερού κόλπου. Στη συνέχεια, θα ανακατασκευαστούν οι τρισδιάστατες γεωμετρίες οι οποίες θα χρησιμοποιηθούν για την διερεύνηση των αιμοδυναμικών παραμέτρων του αριστερού κόλπου, χρησιμοποιώντας την μέθοδο της υπολογιστικής ρευστομηχανικής. Για τον σκοπό της τμηματοποίησης και της ανακατασκευής θα χρησιμοποιηθούν δεδομένα αξονικής τομογραφίας, τα οποία θα επεξεργαστούν με κλασικές μεθόδους επεξεργασίας εικόνας. Σκοπός είναι η επίτευξη ακρίβειας στις γεωμετρίες, έτσι ώστε να αναπαριστούν σε ρεαλιστικό επίπεδο τους ασθενείς.

Σε αυτή τη μεταπτυχιακή διατριβή, αναπτύξαμε και μελετήσαμε 13 διαφορετικές ανατομικές μορφολογίες του αριστερού ωτίου, για συγκεκριμένους ασθενείς. Η μελέτη των αιμοδυναμικών παραμέτρων είναι σε θέση να ρίξει φως στην λειτουργικότητα του ωτίου. Πιο συγκεκριμένα εστιάσαμε στην επίδραση των διαφορετικών μορφολογιών στις ταχύτητες ροής του αίματος και κατ' επέκταση στην δημιουργία θρόμβου. Για συνοριακές συνθήκες και παραμετροποίηση των προσομοιώσεων χρησιμοποιήθηκαν κλινικά δεδομένα των ασθενών. Πιο συγκεκριμένα δεδομένα διοισοφάγειου υπερηχογραφήματος ψηφιοποιήθηκαν έτσι ώστε να εξαχθούν τα προφίλ ταχύτητας. Εφαρμόστηκαν πέντε διαφορετικά προφίλ ταχύτητας, τα οποία αναπαριστούν μια κανονική κατάσταση και 4 παθολογικές. Τα αποτελέσματα των προσομοιώσεων διέφεραν σημαντικά ανάλογα με τα γεωμετρικά χαρακτηριστικά του κόλπου αλλά και της μορφολογίας του ωτίου. Πραγματοποιήθηκαν υπολογισμοί ταχυτήτων,

διατμητικών επιφανειακών τάσεων, προκειμένου να συσχετιστούν με την δημιουργία θρόμβωσης. Ο μελλοντικός σκοπός αυτής της έρευνας είναι να προφέρει δυνητικά βοήθεια και ταχύτητα στη λήψη αποφάσεων των κλινικών.

Λέξεις κλειδιά: Αριστερός κόλπος, Αριστερό ωτίο, Μοντελοποίηση της ροής του αίματος, Διατμητικές τάσεις, Υπολογιστική ρευστομηχανική, Μορφολογίες αριστερού ωτίου, Δημιουργία θρόμβου.

Table of Contents

List of figures

List of tables

List of abbreviations

3D	Three-dimensional
AF, AFib	Atrial fibrillation
BPM	Beats per minute
CAD	Computer aid design
CAT	Computerized axial tomography
CFD	Computational fluid dynamics
CT	Computerized tomography
CVD	Cardiovascular disease
CVS	Cardiovascular system
DC	Dice coefficient
DICOM	Digital imaging and communications in medicine
ECG	Electrocardiogram
EEG	Electroencephalogram
LA	Left atrium
LAA	Left atrial appendage
LGE	Late gadolinium-enhanced
LIPV	Left inferior pulmonary vein
LSPV	Left superior pulmonary vein
LV	Left ventricle
LVD	Left ventricular disfunction
MRI	Magnetic resonance imaging
MV	Mitral valve
MVD	Mitral valve disfunction
PET	Positron emission tomography
PV	Pulmonary veins

RBC	Red blood cells
RF	Random forests
RIPV	Right inferior pulmonary vein
RMS	Root mean square
RSPV	Right superior pulmonary vein
RV	Right ventricle
S2S	Surface to surface
TEE	Transesophageal echocardiography
UI	User interface
WBC	White blood cells
WSS	Wall shear stress

List of symbols

C_i	A vector from the centroid of the cell to the centroid of the adjacent cell.
e_i	The vector from the centroid of the face to the centroid of the edge.
f_i	A vector from the centroid of the cell to the centroid of that face
θ_e	Equiangular face/cell.
a	Number of Time Steps
D_H	Hydraulic Diameter
F	Frequency
h	Height.
I	Turbulence Intensity
L_i	Inlet Length
L_o	Outlet Length
m	Mass
P	Pressure
Q	Flow rate
t	Local Time
T	Time Period
u	Component of Velocity
u	Velocity
U_r	Radial Component of Velocity
y^+	Non-Dimensional Wall Distance

Greek Symbols:

γ	Pure shear stress
Δt	Time-Step Size
θ	Angle in Degrees
μ	Blood's dynamic viscosity.
μ_t	Turbulent viscosity
π	Pi Constant
ρ	Density
τ	Shear stress
ω	Angular Frequency

Chapter 1. Introduction

Computational Fluid Dynamics (CFD) is a global tool used in a variety of engineering fields and it has become a primary method for design and analysis. CFD is a unique combination of mathematics and fluid mechanics that provide a bunch of analytical solutions and visualizations to achieve a better understanding of the problems with a user friendly interface (UI). Engineers have been using CFD for decades at industrial design, research and applications, specially to study and demonstrate complex flow dynamics such as aerodynamics, meteorological phenomena, environmental engineering, fluid flows, biomedical engineering, heating, ventilation and air conditioning of buildings, vehicles etc. Significant interest of the computers usage has catched the eyes of the researchers and the industry too, for solving numerus problems at the healthcare domain. The latest years there is an increasing interest in applying CFD methods at the biomedical field to study complex mechanisms in the human body such as blood flow and at general lots of "transport phenomena".

The mathematical modelling in a branch of mechanics has raised the demand and the usage of computer sources to solve such problems specially at the health care domain. Complex computer representations "In Silico models" of biological tissues are being analyzed using CFD approaches. The coupling between CFD and medical imaging can provide us a useful tool to construct subject-specific models for simulations. CFD modeling can enhance the diagnostic assessment, design predictive models and devices. The huge advantage of this method is that is an noninvasive technique which can be used to compute unmeasurable (at clinical practice) hemodynamic parameters and clinical factors noninvasive [1]. 3D patient specific simulations and numerical simulations at their general form, have the advantage that they are not invasive

as the in-vivo experiments. Also, their flexibility provides a variety of tests and clinical trials to be implemented.

The advantage of numerical simulations is that they are less invasive than the in-vivo studies and potentially tend to be more accurate and flexible than the in vitro experiments. A major advantage of this fast-growing field is the capability of testing experimental hypotheses before the implementation in real clinical practice.

Computational models of the Cardiovascular System (CVS) are a combination of medical knowledge with electrophysiology (The impulses of the nerves one of the most important functionalities in the human body) and fluid dynamics (Blood mechanics). Combination of mathematics and physics such as elasticity theory (The movement of the muscles, the arteries) are used in practice for solving numeric problems. Most of the times these models are simplified versions of reality, where some effects are been neglected or dimensions are been reduced. Nowadays, the accuracy of a cardiovascular model depends on its reliability except from the approach and the solver etc. As much the simulations and the 3D models are realistic (e.g the walls are moving and the leaflets are closing/opening), the results would be proportional to that. In Figure 1.1 is depicted a realistic 3D cardiac model, including all the chambers.

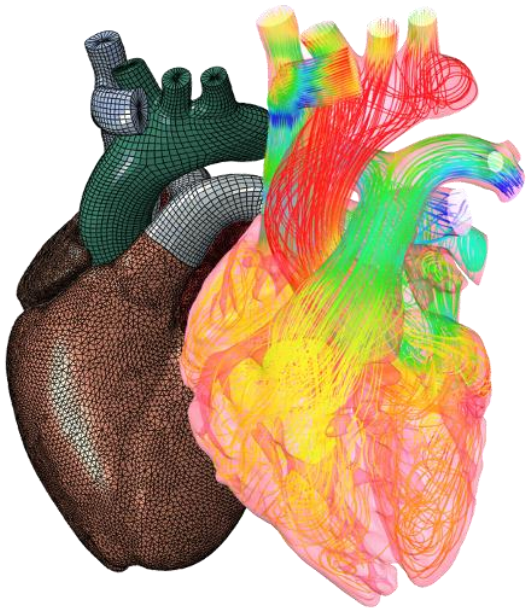

Figure 1.1. Representation of a CFD four chamber heart 3D model simulation [2].

Mathematical and numerical modelling of the Cardiovascular System has attracted remarkable interest from the research community due to its high potential impact on physiology, risk stratification, heart functionality and patient's outcomes

1.1 Clinical problem

It has been established that the Left Atrial Appendage (LAA) structure is a cavity where an extensive majority of thrombus are formed. Its high anatomical roughness consists it a cavity with critical impact factor at flow. Studies have proposed that the morphology of the LAA have gradient value for thrombus formation [3]. The percentage of strokes related to thrombus detachment increases from 1.5% at 50-59 years old to 23.5% at 80-89 years old [4]. Furthermore, studies try to investigate the role and the functionality of the LAA cavity as there are surgical practices that cut off and obliterate the LAA, and the atrium's functionality remains the same. Still the complete understanding of LAA's role and its morphological shape is unfathomable. However, there is still limited data on numerical hemodynamics in the LA and LAA as previous studies have shown. Here, at this thesis we are going to investigate the hemodynamics at LA and LAA.

1.2 Motivation

''Biomechanics in the study of the structure and function of biological systems by means of the methods of mechanics'' *Hatze et al.* [5] described. "The heart is the strongest muscle of the body" so this thesis was a challenge to me first to fully understand how the heart works and afterwards to investigate the functionality of the LA and the LAA to examine their pathophysiological role using CFD. Moreover, from my point of view and as lot of studies have shown, the combination of engineering with medical and clinical knowledge is a promising field which stand to make our everyday living easier and better.

Cardiovascular disease (CVD) is the leading cause of death in modern society, especially in the western world, accounting atherosclerosis as most of the cases. At 2018 nearly there were 836,546 deaths in the US. About 92.1 million American adults suffer from a cardiovascular related disease. The total cost of cardiovascular diseases and strokes is estimated to be more than $329.7 billion which includes both health expenditures and lost productivity. The CVDs will continuously and increasingly burden human beings and 23.6 million people are expected to die by 2030 [4]. Most deaths from CVDs would occur as the result of heart attack, coronary artery disease or stroke. Coronary heart disease and stroke have a higher rate than any other disease.

The Left Atrium (LA) and Left Atrial Appendage (LAA) are interlinked cardiac structures constituting the most significant source of cardioembolic events, predominantly in patients with Atrial Fibrillation (AFib) but also mitral valve disease and left ventricular dysfunction [6]. CFD cardiovascular modeling can help through noninvasive techniques to predict patient status, to provide decision support systems and of course to reduce the cost [1].

1.3 Aims and objectives

The aim of this thesis is the understanding of cardiac blood flow and functionality, by means of the mechanical development and assessment of various approaches for patient-specific hemodynamics. In this study, employing CFD to examine the local hemodynamics at LA, we are investigating the impact of the anatomic morphologies of LAA on the blood flow. A further purpose of this work is to be used of medical experts at clinical practice so they can exploit the outcomes to enhance their decision making about clinical procedures. This thesis arises from the fundamental matters that the mathematical description and computer simulations of the cardiovascular system can shed light on this field and that they can be used to help medical experts.

At the next chapters, a detailed description of the thesis outline and the main objectives, are presented. We first start from general information for cardiovascular system and CFD. We use CFD to investigate the LA and the LAA and describe the local hemodynamics of these two chambers. To implement this, we developed an in-house code for the 3D reconstruction and a steady, powerful commercial CFD solver. This thesis is structed as follow. In the second Chapter the Cardiovascular System is described and introduced. The third Chapter does a brief description of the current state of the art and what studies of LAA have shown. The fourth Chapter describes the image processing and the 3D reconstruction methodology, as afterwards the grid generation of the 3D models is deployed. The fifth and sixth Chapters are presenting the numerical formulations and the methodology for the blood flow simulations and their implementation. The seventh and eighth Chapters are demonstrating results and findings, as an overall discussion and thoughts for a further work plan.

So far very few studies have been done focusing on computational modeling of LA and LAA and its aspects. Most of the computational studies referring to CVS, focus on ventricular modeling where the 3D models are more detailed and refined than the atrial models. Even if the LA represents the main reservoir cavity of the intraventricular flow during diastole, its geometry is still oversimplified at the most studies, usually is demonstrated as a rigid tube without LAA. The LA is the opposite of a prior passive transport chamber to the LV. Its role and its importance for ventricular filling is significant [7].

A brief theoretical background has been introduced above, so now we can notice that we are dealing with a non potty problem. The main aim of this work is to obtain and achieve a profitable simulation of blood flow in the left atrium and examine the impact of the appendage's morphology. In order to do that our model and its aspects would be analyzed in next chapters.

Chapter 2. The heart

The principal functionality of the cardiovascular system is the distribution of blood to all the tissues of the body to ensure adequate transport of all the nutrients the body needs. This system is responsible for the delivery of oxygen and nutrients to the cells and the withdrawal of carbon dioxide and other cell wastes, through the circulatory of the blood. Its function overall is to operate tasks and transfer ingredients and nutrients to the noble organs and the periphery essential for the life. The understanding of the pathophysiology of the heart's functions and diseases presuppose in depth the knowledge of mechanical and electrical alterations. The cardiovascular circulation is a complex dynamic system that is comprised of atriums, ventricles and different kind of vessels. The human heart is a four chambered muscular organ that contracts and expands periodically. The circulatory system in most adult humans circulates approximately 5L of blood around the body every minute while during exercise the blood supply can increase up to 25 L. Both the right and left side of the heart have the same structure, where on top lie the atrias and at their base they interconnect with the ventricles. The aim of this chapter is to introduce the principal functionalities of the cardiovascular system and to briefly explain its complexity. The main purpose of the upper part is to receive blood and the lower part eject it to the rest of the body [8].

2.1 Structure

2.1.1 Location and shape

The heart is placed in the middle mediastinum of the thoracic cavity surrounded by the lungs and protected by the chest bones. The normal human heart has a mean mass of 250-350 grams and a kind of a cone shape with its base positioned upwards and its peak downwards. The normal referenced dimensions are 12 cm in length, 8 cm in wide, 6 cm in thickness, although the mean dimensions are disputed because the shape varies between individuals (e.g it is very common in athletes to have a larger heart due to training and the effects of exercise to the heart muscles). The upper part outgrowth large blood vessels such as the aorta, the venae cavae and the pulmonary trunk. The left heart is stronger and larger, since it pumps the blood to all the body.

2.1.2 Chambers

Right atrium: This structure is mainly constituted by the Musculi Pectinati. The blood reaches this chamber from the superior and the inferior Venae Cavae (from the Latin word for **"hollow veins"**, singular **"vena cava"** are two large veins which return the deoxygenated blood from the body to the heart) and the coronary sinus as it is pushed through the unidirectional tricuspid valve to the right ventricle.

Right ventricle: Is the chamber of the heart that has the function to send the deoxygenated blood through the pulmonary trunk and the right and left pulmonary arteries to the lungs. Internally the right ventricle presents the Trabeculae Carneae or meaty ridges which are rounded or irregular muscular columns which project from the inner surface of the ventricles.

Left atrium: The left atrium receives the oxygenated blood from the pulmonary veins and the lungs. Afterwards, it pumps it to the left ventricle towards the mitral valve, which is responsible to prevent the backflow, and maintain a constant open/close rhythm. The main functionality of the left ventricle is to sustain the diastolic filling of the right ventricle both regularizing the inflow and increasing the late diastolic pressure gradient with what is called "atrial kick". The blood flow conditions inside the LA have significant impact on abnormal conditions such as atrial fibrillation (AF) [9] and stroke.

Left ventricle: The left ventricle is responsible for the blood supply for the great majority of the circulation. Being filled of oxygenated blood by the left atrium, this heart chamber can eject a volume of blood of around 70 ml at every cycle towards the aortic valve.

All the chamber we analyzed above are depicted in Figure 2.1 where a detailed anatomy of the heart is denoted. Each cardiac chamber is demonstrated with it's role regarding the blood flow circulation.

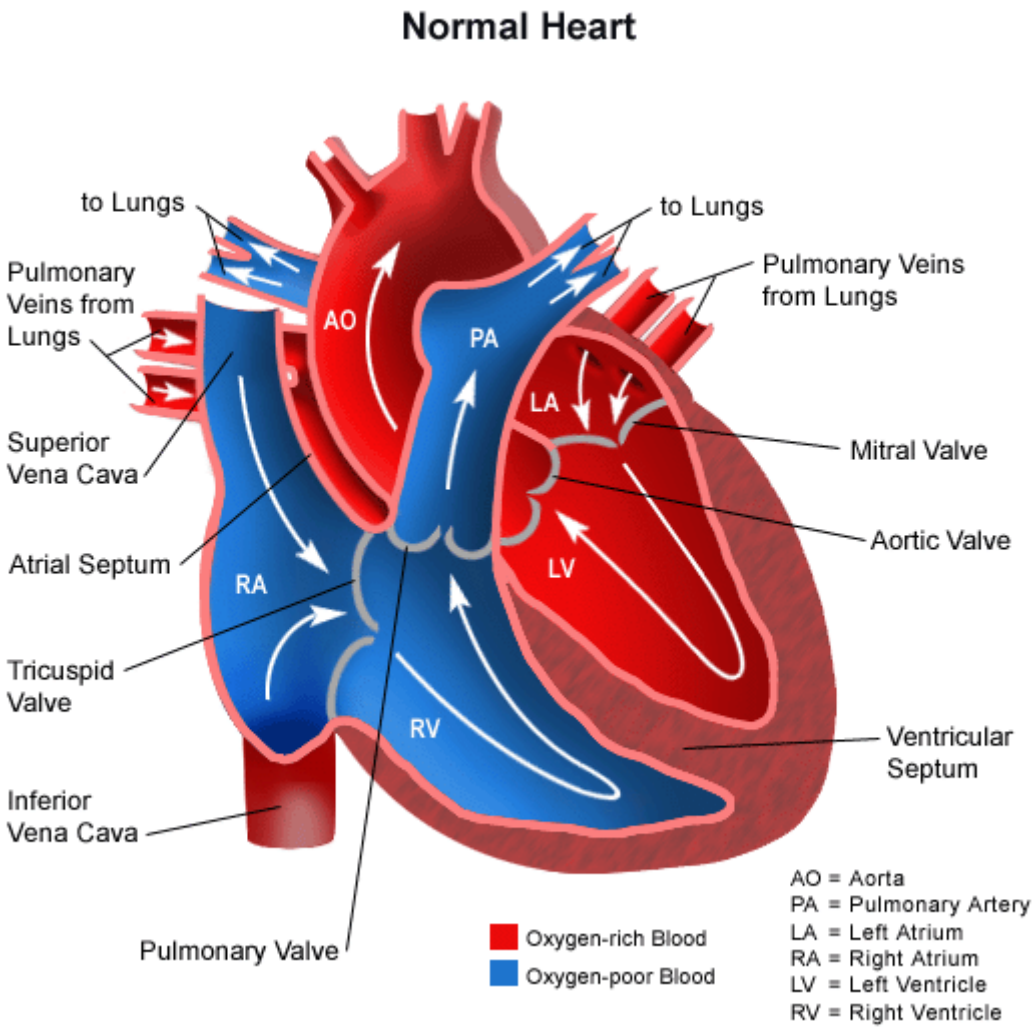

Figure 2.1. Sectional detailed anatomy of the heart [10].

2.1.3 Cardiac valves

The direction of the blood between the champers of the heart is controlled by the systolic and diastolic movements of the heart as well as by the intracardiac valves. The heart has four unidirectional (preventing backflow of the blood) valves: the tricuspid, the mitral, the aortic and the pulmonary valve. The valves consist of a fibrous ring of cardiac skeleton with a variable number of leaflets, mainly consisting of collagen reinforced endothelium. Since there is not any kind of nerve or muscle control, valve movement is fully governed by pressure gradients, inertia and viscous and turbulent forces. Each chamber of the heart is separated from the others. The valves (Figure 2.2) between the atrium and ventricle are called atrioventricular. Between the right ventricle and the right atrium lies the tricuspid valve which has 3 leaflets. between the left atrium and the left ventricle lies the mitral valve (MV), also referred as bicuspid valve due to its two leaflets which are attached with chordae tendinae to papillary muscles arising from the ventricular wall. The Mitral valve is responsible for ejecting the blood from the left atrium to the left ventricle. Two lunate shaped valves are placed at the exit of each ventricle.

The pulmonary valve which is placed at the base of the pulmonary artery and it has 3 leaflets, and the aortic valve at the base of the aorta which also has 3 leaflets.

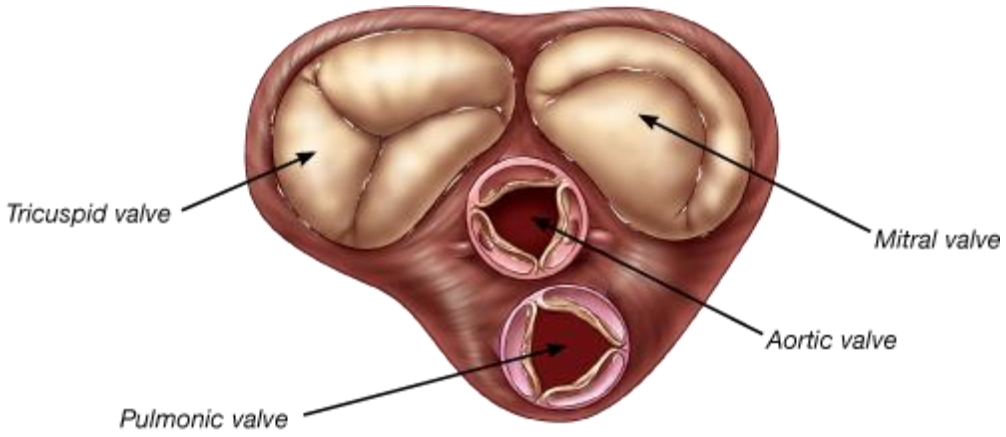

Figure 2.2. The four cardiac valves that separate the chambers (tricuspid valve, mitral valve, aortic valve and pulmonic valve).

2.1.4 Heart wall tissues

The heart wall consists of 3 layers, the inner layer or endocardium, the middle or myocardium and the outer layer or pericardium. The central fibrous region of the heart aka fibrous skeleton is used as a base for the valves and as the myocardial cells' origins and insertions region. The endocardium is made of a lining of simple squamous epithelium which covers both the heart and the valves. It is continued with the endothelium of the veins and arteries of the heart ending up to the myocardium with a thin layer. The myocardium is the thickest of all the layers and it consists of striated muscle tissue surrounded by collagen. This cardiac muscle pattern is complicated as it is consisted of swirl muscle cells with a spiral shape around the heart. This swirling structure helps the heart to dilate efficiently and receiving enough blood for the demands of the body.

The heart is covered by an external membrane called pericardium which has two layers. Between the parietal and visceral layers of the pericardium is a very thin, fluid-filled serous space, or cavity, which facilitates the movements of the heart. The above description is depicted in Figure 2.3

The cardiac muscle is consisted of two major type of cells primarily by cardiac muscle cells which can contract very easily, and they make the 99% of the volume in the atria and ventricle A specialized type of muscle cells are the Purkinje fibers originating from the sinoatrial node. Purkinje fibers are responsible for the synchronized contraction of the ventricles and they are essential for maintaining a consistent contraction rhythm.

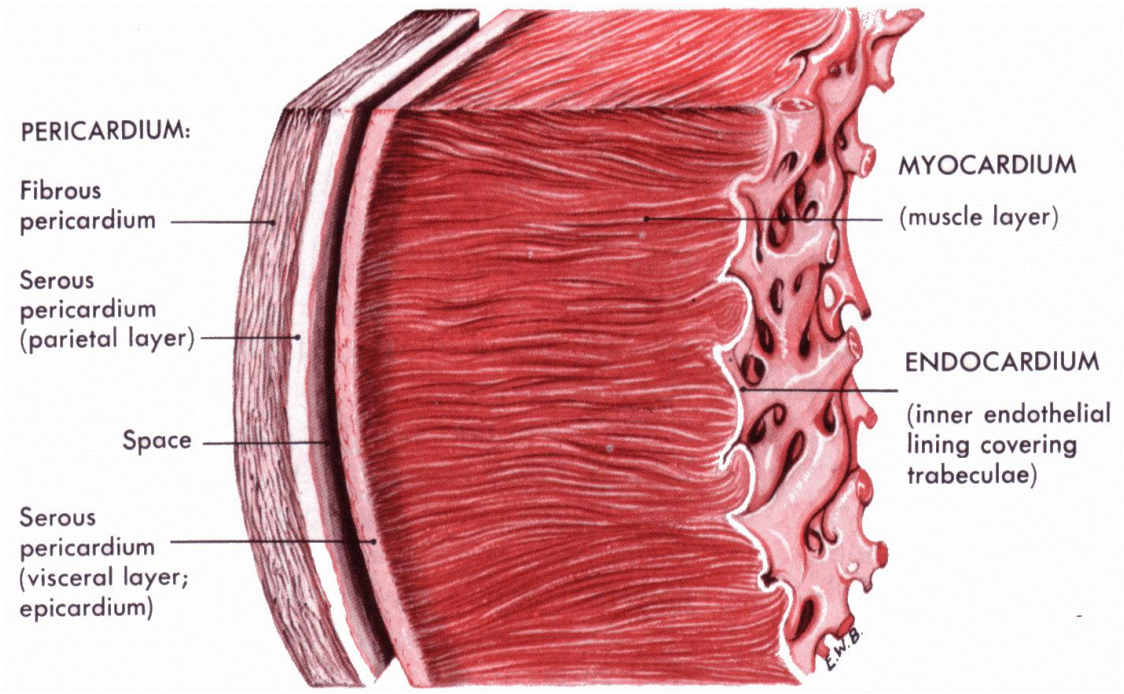

Figure 2.3. The cardiac tissue structures [11].

2.2 The circulatory system

The heart is one of the principal organs of the CVDs. Its functionality mimics a pump trying to eject a proper amount of blood to irrigate all kinds of tissues. The heart is divided by the interatrial and interventricular septa into two main parts, the right and the left heart, which in turn they are divided into atrium and ventricle. The flux between atria and ventricles is guaranteed by four valves, two atrioventricular and two semilunar. Below we are analyzing the role and the functionality of each heart chamber. Further analysis of the left heart will be available as we focus at the left atrium on next chapters.

The responsibility for the blood transport to tissues goes to the arterial system. Another important functionality of the arterial system is to maintain the arterial pressure to normal ranges. This range is relatively high because the distal end of the arterial system, has lots of bifurcations leading to diminish vessel's diameters and forms a large peripheral resistance. The diameter and thereby the resistance can be affected by the smooth muscle cells from the wall. Also, unlike the heart condition of the individual, the viscus forces are significant factor which affect characteristic parameters, responsible for blood flow, such as velocities of blood and length scale.

Everything around us demand energy (mechanical work) to produce a movement, which stands for the movement force x displacement. Thus, the demanding work to force a kind of displacement, depends on the weight of the object and the force which is mandatory. Respectively the heart needs to consume energy to generate blood flow. The heart functionality

and its cycle depend on the overall condition of the body. It has been found that a mean rate of 55-90 beats per minute (BPM) is characteristic of a healthy heart, but in case of intense activity that rate can reach 200 BPM [12]. The mechanical energy produced by the heart per heartbeat is:

$$W = QP + \frac{1}{2}mu^2, \tag{1.1}$$

where Q is flow rate, m is the mass ejected, P is the blood pressure, u is the blood velocity. The part of the kinetic energy is quite negligible (2% of the left and 5% about the right heart), a condition which may become more respective under physical exercise. The flow rate Q under normal conditions is $5x10^3$ cm^3 min^{-1}, assuming we have 60-90 BPM → 55-83 cm^3 of blood ejected at each heartbeat.

2.2.1 Blood

Rigorously speaking, blood is not a fluid, but it's composed of blood cells and plasma. Blood cells include, red (RBCs or erythrocytes) and white blood cells (WBCs or leukocytes) and platelets. The plasma is an aqueous polymeric and ionic solution which is composed of 93% water and 3% particles such as electrolytes, organic molecules, and numerous proteins (fibrinogen, albumin). Plasma's main functionality is to transport these substances and elements throughout the circulatory system. Erythrocytes have a biconcave disc structure with a mean diameter of 6-8 μm and a maximum thickness of 1.9 μm. A typical average volume of them is 90 m^3. Their number per cubic millimeter of blood is approximately $5\text{-}6x10^6$ and they represent 40-45% of the total human blood of the normal volume. The density of the blood is ρ= 1060 Kg/m^3 and its dynamic viscosity is μ= 0.0035 Pa·s.

2.2.2 The cardiac cycle

2.2.2.1 Conduction system of the heart

The cardiac conduction system, depicted in Figure 2.4, is a network of myocardial cells specialized in initiation and quick transmission of the electrical impulses responsible for the coordinated contractions of each cardiac cycle. The two atrias contract simultaneously as do the two ventricles, but the contraction precedes the ventricular. The conductive system of the heart is responsible for the automated rhythmic cardiac cycle. It consists of:

1. The sinoatrial node at the upper wall of the right atrium
2. The atrioventricular node at the septum
3. The bundle of His with its two branches and the Purkinje fibers from the atrioventricular node to the septum

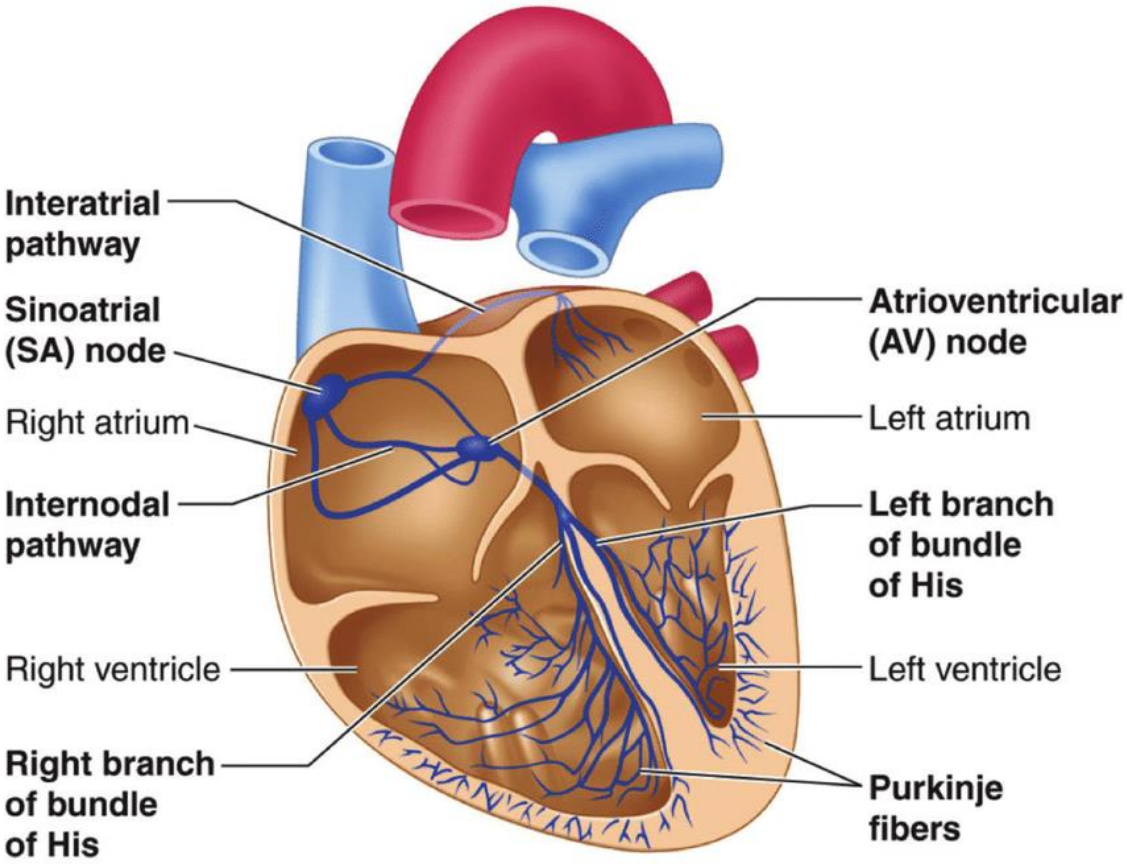

Figure 2.4. The conduction system of the heart [13].

The sinoatrial node is the natural peacemaker of the heart. The sinoatrial node produces an incentive which is immediately conducted to the muscle fibers of the atrias, cause their contraction.

This incentive goes to the atrioventricular node and it is distributed to the septum, to the papillary muscles and the ventricular walls. The papillary muscles contract first pulling the tendon cords and sinuses of the atrioventricular valves that join and close the orifices.

The cardiac cycle could be divided at two major phases: Contraction and Relaxation (Systole and Diastole). The cardiac cycle comprises into 4 basic phases, (1) filling, (2) isovolumetric contraction, (3) expulsion, (4) isovolumetric relaxation. The 2, 3 phases are known as systole, while 4, 1 diastole. The rhythm of the heart is generated by the sinoatrial node, an impulse-generating tissue located in the right atrium of the heart, at least in healthy conditions. Bellow, Figure 2.5 depicts all the stages and phases of the cardiac cycle.

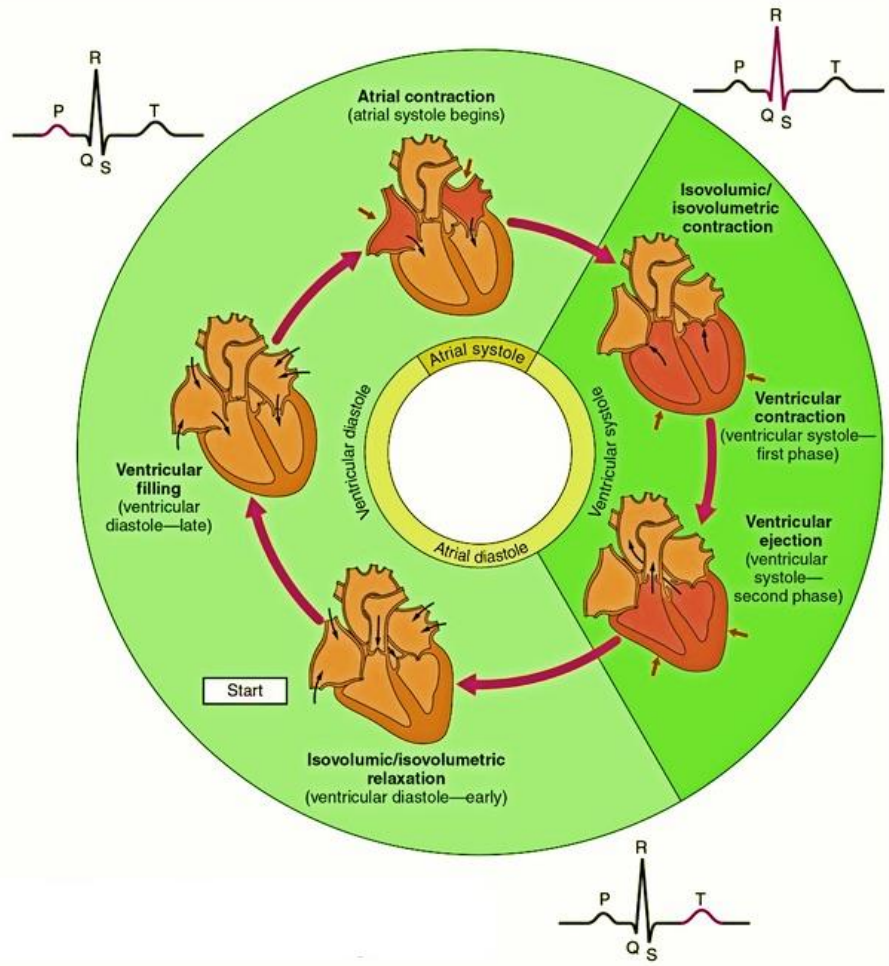

Figure 2.5. All the phases of the cardiac cycle are depicted above. The red colored chambers denotes their functionality at the specific timepoint [14].

1. **Atrial contraction**

   At this phase the atrioventricular valves are open as the minuscules are closed. The electrical discharge of the atria (recorded as P wave in the electrocardiogram) causes mechanical contraction of the atrial myocardium. Atrial contraction [15] increases the pressure in the cavity of the right and left atrium, resulting in blood flow through the open atrioventricular valves. The raised pressure in the atrial contraction is recorded as **a** wave (from a=atrial systole) and the filling of the ventricular cavities as a result of the atrial systole is referred as "atrial kick". At the end of the atrial contraction there is a decrease in pressure in the atria which is recorded as **x** wave, resulting in the reset of the atrioventricular valves to a closed position, producing the first cardiac sound, aka S1. The volume of blood in the ventricles at the end of the atrial contraction is called **end-diastolic volume** and it is the largest throughout of the cardiac cycle. Accordingly, the pressure in the ventricles at the end of the atrial contraction is called

end-diastolic pressure. Blood flow to the ventricles during atrial contraction generates small vibrations in the abdominal myocardium, which cause the fourth heart tone (denoted as S4, S=sound). The intensity of S4 increases when the abdominal walls are not elastic as in hypertrophy. The above description of the atrial pressure is depicted in Figure 2.6.

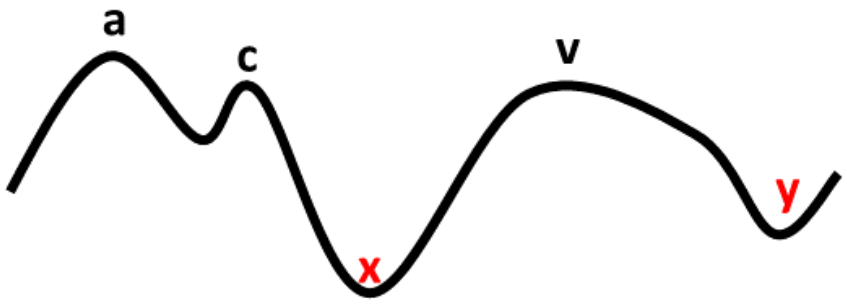

Figure 2.6. The waveform presenting the wave peaks of the atrial pressure.

During exercise where the heart rate is increased, the contribution or the atrial contraction to the diastolic volume is approximately 40%. Consequently, loss of atrial contraction (such as Atrial Fibrillation) causes a decrease in pulse volume, mainly during intense physical activity.

2. **Isovolumic contraction (rapid ejection and reduced)**

Ventricular repletion causes the ventricular myocardial cells to contract, resulting in a rapid increase in pressure in the cavity. Increased pressure in the ventricles relative to the sinuses, causes the atrial valves to close which produces the first heart sound (S1). Normally, mitral valve closure precedes this tricuspid by about 40 msec, but this interval is so short that this tearing of the first heart tone is not readily apparent upon hearing. Atrioventricular valves closure disrupts the blood flow from the atrium to the ventricles, resulting in a small transient increase of pressure recorded as wave **c** (from c=closure). After the closure of atrioventricular valves, the continuous shortening of the ventricular myocardial cells, causes an increase in pressure in the cavity without altering the volume, as all valves of the heart are closed. The closure of the semilunar valves produces the second heart sound, aka S2. Because of this property the first phase of the coincidence is called ischemic in which the total volume does not change, although the shape of the ventricle becomes more spherical. The first pressure derivative (dp/dt) expresses the velocity of pressure rise in the ventricle and is determined by the slope of its curve over time and it is depicted in Figure 2.7.

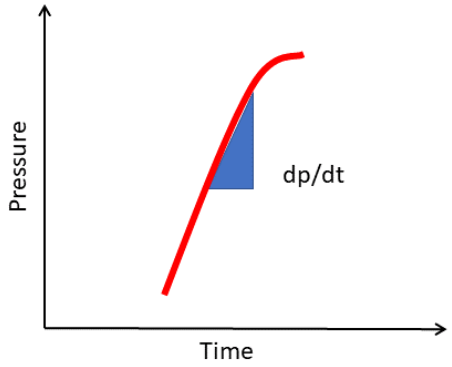

Figure 2.7. First pressure derivative that expresses the velocity (dp/dt).

3. **Ventricular ejection**

   At the extrusion of blood from the ventricles the atrioventricular vales remain closed while blood flow from the concave veins to the right atrium and respectively from the pulmonary veins to the left atrium. The pressure drops at atriums due to increase of their dimensions is mitigated as the progressive increase of blood volume due to blood flow. The pressure drops at atriums which prevails at the end is recorded as wave **x**. At the end of isovolumic contraction, a continuous increase in pressure in the right ventricle at a value greater than that in the pulmonary artery and in the left ventricle at a value greater than that in the ascending aorta, causes the open of the atrioventricular valves.

4. **Isovolumic relaxation (rapid filling and reduced)**

   About 200 msec after the start of depolarization the repolarization starts, and it is recorded as wave **t**. The included rupture of the myocardial cells results in a decrease in pressure in the cavity. When the pressure in the ventricles is reduced to lower than those in the large vessels, the pressure gradient is reversed resulting in sudden closure of the valves. During the time between the closure of the lumbar valves and the opening of the atrioventricular valves the volume remains constant, as all four heart valves are closed. The volume of blood in each ventricle after closure of the lumbar valves is called the end-systolic volume and is the smallest throughout the cardiac cycle. The closure of the lumbar valves at the end of the extrusion is recorded as the second heart tone (S2). The first derivative of pressure at the isovolumic relaxation expresses the reduction rate of the pressure at the ventricle by the slope of its curve over time. The reduce of the pressure after the time point -dp/dt, presented in Figure 2.8, is exponential and its properties are expressed by the parameter of isovolumic relaxation $\boldsymbol{\tau}$.

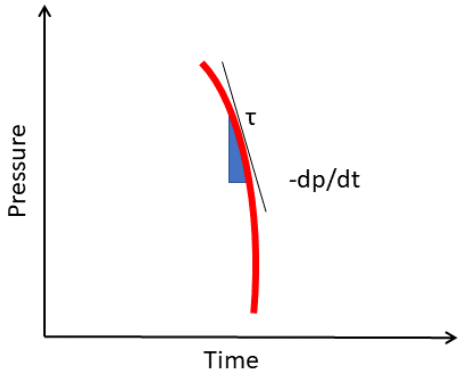

Figure 2.8.Pressure decrease and isovolumic relaxation τ (-dp/dt).

5. **Ventricular filling**

Ventricular diastolic filling occurs during the period between the opening and the closure of the atrioventricular valves. During this phase, the pressure in the pulmonary artery and aorta is reduced, due to the continuous flow in circulation. ventricular filling is distinguished by velocity deceleration.

All the above are depicted systematically in a standard technical diagram that is used in cardiac physiology named "Wiggers diagram" in Figure 2.9.

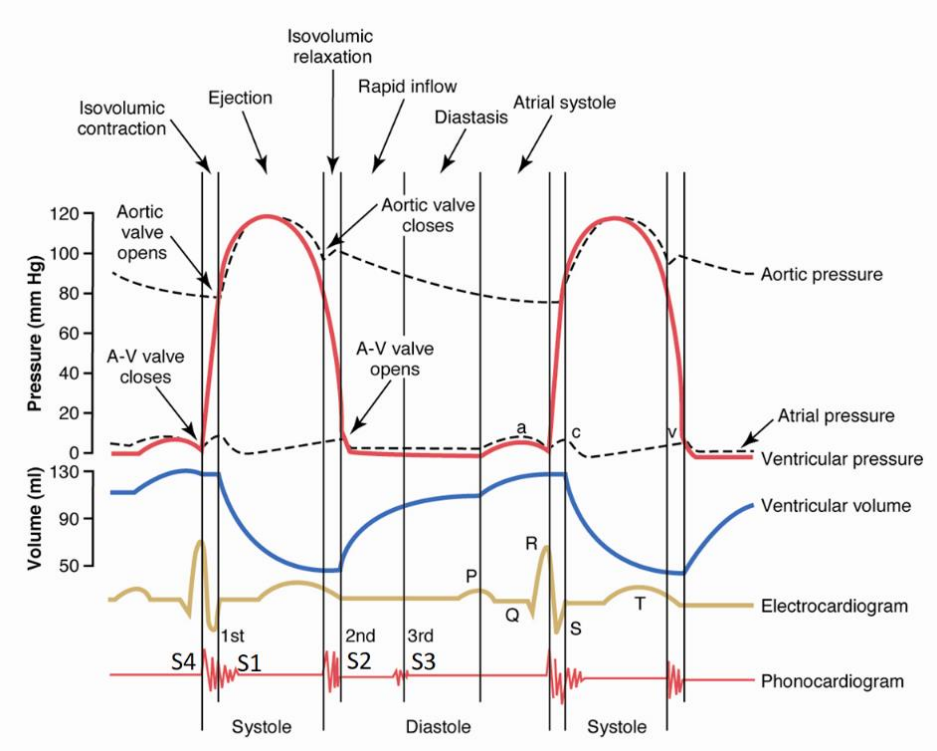

Figure 2.9. The Wiggers diagram [16].

2.3 Left atrium anatomy

The Left Atrium (LA) (Figure 2.10, Figure *2.11*) is a cavity with an oval morphology and a smooth inner surface. The LA is a highly complex anatomic structure given multiple inlets at

the insertion of the Pulmonary Veins (PV), single outlet at the Mitral Valve (MV) orifice and the presence of the left atrium appendage (LAA), a blind-ended structure on the anterior-lateral wall of the LA whose anatomic form is highly variable. The inner wall of the atrium is continuous with the wall of the right atrium and it's called interatrial septum. This wall is slightly oval at the area of the right atrium where fossa ovalis lie. A thin membrane covers the fossa ovalis and it called foramen ovalis and it can be presented with a slight slice at the top [17].

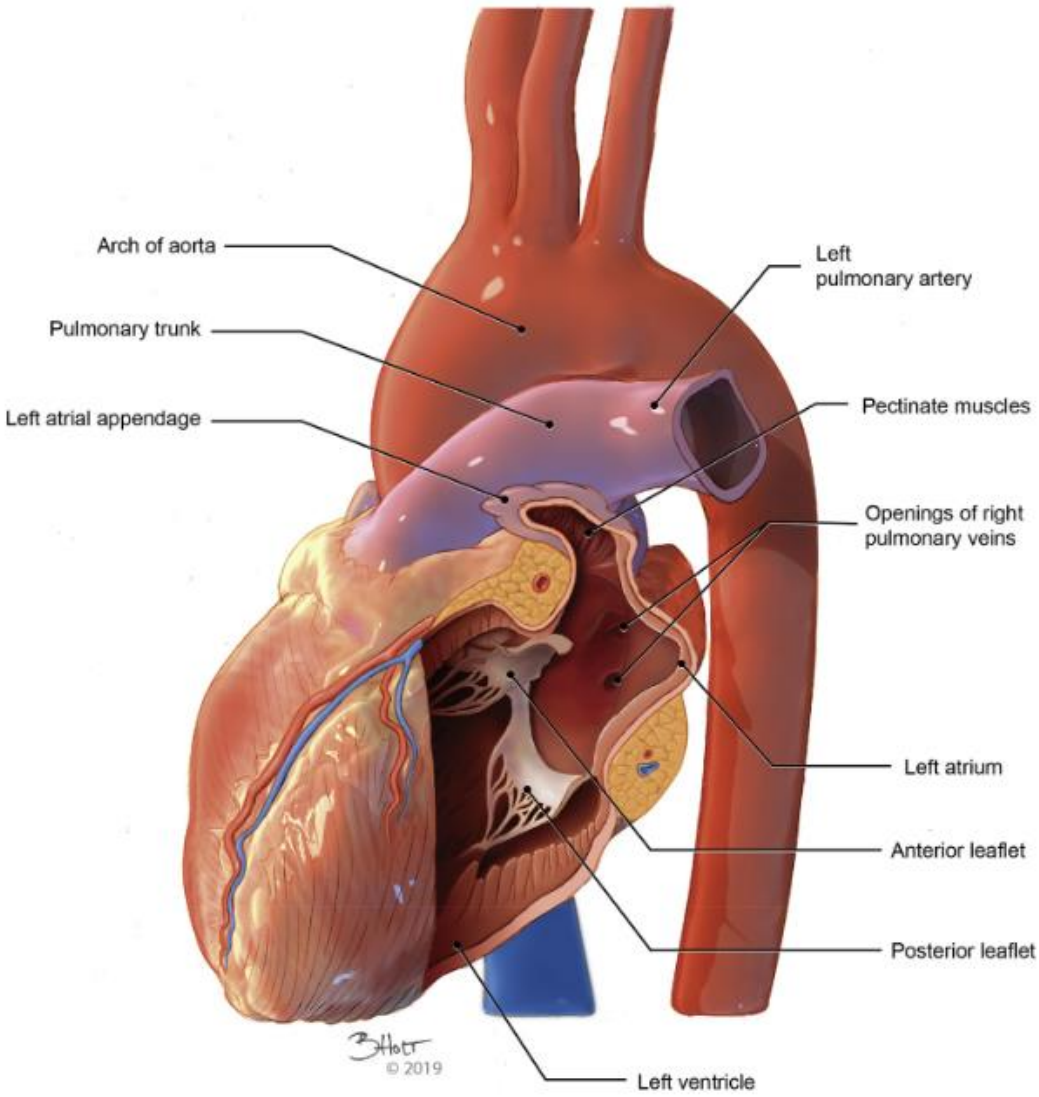

Figure 2.10. A detailed anatomy of the left atrium, depicted with an axial cut [18].

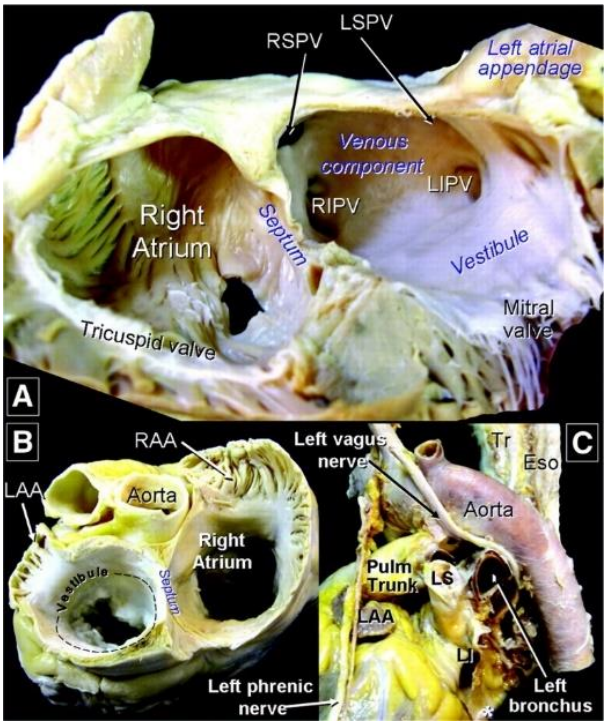

Figure 2.11. Realistic detailed left atrial anatomy, denoted with all the cavities and anatomical areas (A, B, C) [19].

The significance of the LA and LAA in several clinical conditions, such as Atrial Fibrillation (AF), valvular disease is critical. Three-dimensional (3D) reconstruction of the LA and surrounding structures with combination of CFD modeling, it may provide further insight into the pathophysiologic process. Moreover, by implementing this approach we can extract primal information about the functionality of the heart. The left atrium (LA) and left atrial appendage (LAA) are interlinked cardiac structures constituting the most significant source of cardioembolic events, predominantly in patients with atrial fibrillation but also mitral valve disease and left ventricular dysfunction [17].

2.4 Left atrial appendage (LAA)

The LAA (Figure 2.12) is a blind-ended structure on the anterior-lateral wall of the LA whose anatomic shape form is highly variable. In the past LAA has been an insignificant part of the cardiac structure. At latest years it is being recognized as a structure with important pathological associations. Thrombus has a high prediction to form within the LAA in patients with AF.

Qamruddin et al. [20] referred that "The trabecular LAA is the remnant of the original embryonic left atrium that develops during the third week of gestation". The main smooth walled left atrial cavity develops later and is formed from the outgrowth of the pulmonary veins. It is a finger-like projection of the main LA body. The LAA has a long tubular, hooked morphology and has a narrow junction with the venous component of the atrium. On the other hand, the right atrial appendage is wide and triangular shaped, but at the end both side's

appendages are trabeculated with muscle bars largely running parallel to each other (pectinate muscles).

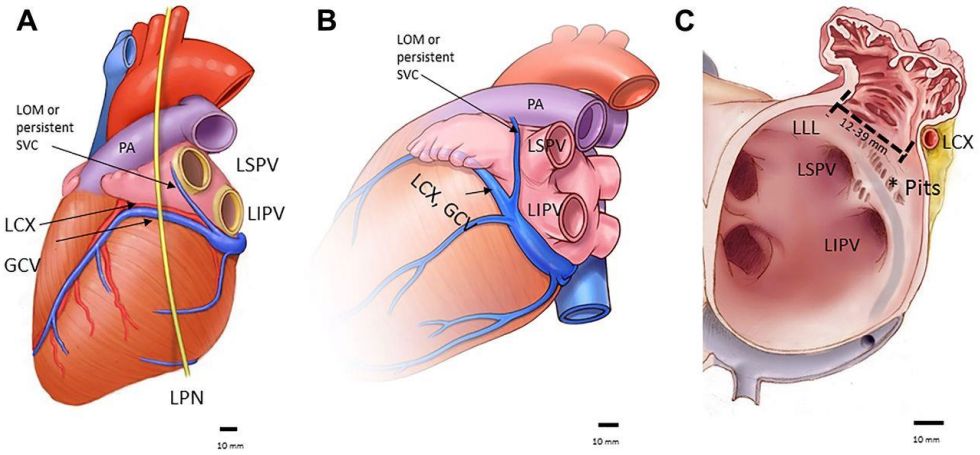

Figure 2.12. LAA ling area (A), LAA attached to the LA (B) and internal LAA anatomical morphology (C) [21].

Morphologies of the LAA presented in Figure 2.13 are classified into four major categories: the "Chicken wing" (48%), the "Cactus" (30%), the "Windsock" (19%), and the "Cauliflower" (3%). According to a recent study, the risk of stroke is 54% lower in patients with chicken wing morphology compared to other anatomic variants [3] and cactus has the higher risk for thrombogenesis.

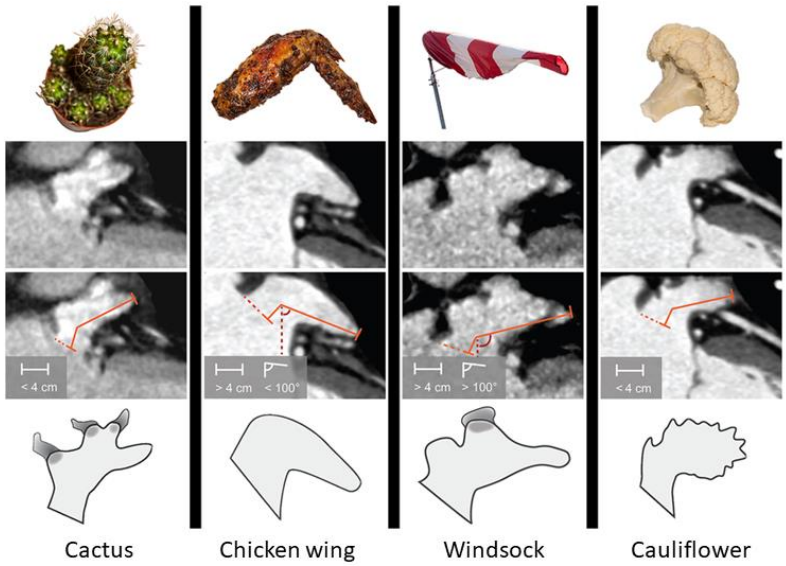

Figure 2.13. Morphological types of LAA (the "Chicken wing" (48%), the "Cactus" (30%), the "Windsock" (19%), and the "Cauliflower" (3%)) [22].

Until recently there have been no publications about the anatomy and the functionality of LAA. The first such detailed description of LAA was provided by *Ernst et al.* [23]. LAA volume varies from 0.7 ml to 19.2 ml. The size of the orifice of the LAA also varies considerably with a minimum diameter 5-27 mm and maximum from 10-40 mm. The length of the LAA ranges from 16 to 51 mm.

2.5 Physiology of LAA

The structure of the LAA shrinkers to a greater extent than the rest of the left atrium and has a distinct pattern of contraction. Blood flow inside the LAA can be studied with transoesophageal echocardiography, which provides good views of the appendage. The flow cycle begins with a first phase of forward flow (out of the appendage) which occurs after the transmitral flow in early diastole, followed by a short phase of backward flow (into the appendage). The starting point of the forward phase of blood flow, is at the early diastole. That creates a relation between LV relaxation and an early emptying of the appendage. This arrangement has strong dependency on the heart rate.

The appendage lies relatively immobile to the pericardium. As the left ventricle dilates during diastole it fills the intrapericardial space and it has been suggested that it may contribute to appendageal emptying by compressing the inferomedial wall of the LAA.

2.6 Atrial fibrillation (AF)

Atrial fibrillation (AF) is the most common heart rhythm disorder (tachyarrhythmia) and is becoming progressively more prevalent with population aging. Despite the progress of treatment and techniques to patients with cardiac disorders, AF remains one of the major causes of thromboembolic events. Some patients with AF can feel the abnormal heart beating (heart palpitations) while others have a shortage in exercise ability due to reduce in cardiac output. In 2010, the estimated worldwide number of men and women with AF were 20.9 million and 12.6 million respectively. One in four middle-aged adults in Europe and US will develop AF.

Hypertension, cardiac failure, valvular heart disease, hyperthyroidism and chronic obstructive pulmonary disease are some of the major causes of atrial fibrillation. AF is characterized by an irregular rapid (over 600 beats/min) and chaotic electrical depolarization of the atrias. This abnormal rhythm occurs because of the unpredictable condition of disordered impulses across the electrical bridge (Atrioventricular node AV), to the lower cardiac chambers (Ventricles). It is similar to atrial flutter, but AF has more serious implications such as stroke or thrombosis creation. During AF the upper chambers of the heart (left atrium and right atrium) beat irregularly with lose of beat rhythm, out of coordination with the two lower ventricle chambers. These arrhythmias result in ineffectual atrial contractions affecting cardiac output and vulnerability to blood clot (Thrombus) formation that can result in stroke events. Larger concern with AF is the potential to develop clots and moreover thrombus formation, specially at the LAA cavity. The loss of the atrial contribution to LV filling and stroke volume with atrial fibrillation often leads to symptomatic deterioration. A serious major complication of AF that studies have shown, is blood stasis in the atrium and specifically at the LAA chamber. Blood stasis can lead to thrombus formation which after can dislodge and embolize in cerebral

or other arteries, thereby causing ischemic injury or stroke. It has been found that LAA volume and luminal surface area are higher among patients with AF [24].

2.7 Pathogenesis of clot formation

Hemostasis is a major defensive mechanism of the human body against bleeding. Its purpose is to protect the body from bleeding and at the same time to maintain the liquid consistency of blood to prevent it from thrombosis. It is consisted of an aggregation of complex biochemical processes and mechanisms of interactions between "coagulation factors", blood cells (especially platelets) and vascular endothelium.

Clotting or thrombus formation is the process where blood changes composition from liquid to a gel form with much higher density and it potentially it results in hemostasis. The clotting system is consisted of two phases:

1. **Primary hemostasis**: Formation of a weak platelet plug.
2. **Secondary hemostasis**: Stabilizing the weak platelet plug into a clot by the fibrin network.

Thrombosis most of the times forms into blood vessels but at this study we refer to LAA instead of vessels. The association of atrial fibrillation and the risk of stroke through the thromboembolism has already been recognized.

According to Virchow's triad theory (Figure 2.14), there are three board factors for thrombosis:

1. Stasis of blood flow
2. Endothelial injury
3. Hypercoagulability

When an individual suffers from atrial fibrillation the Virchow's criteria are fulfilled. The abnormal condition leads to absence of contraction movement of the atrias, resulting to blood stagnation and thrombus formation.

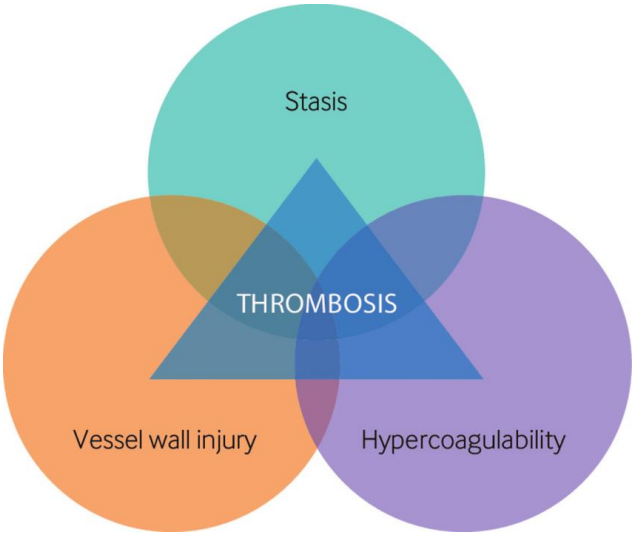

Figure 2.14. Modules of the Virchow's triad law [25].

2.8 Medical imaging

Medical imaging is the technique and the process to create virtual representations of the internal of tissues for medical intervention as well as visual representation of them. The purpose of the human need to reveal the internal structures hidden by the skin and the bones is to diagnose and treat any possible disease. The discipline of all that in the bigger picture is part of biological imaging in combination with radiology where technologies such as x-rays, radiography, magnetic resonance imaging, medical ultrasonography or ultrasound, endoscopy, elastography, tactile imaging, thermography and nuclear medicine functional imaging techniques as Positron Emission Tomography (PET).

There are some other techniques, not designed to produce images but to measure and record, such as electroencephalography (EEG) electrocardiography (ECG).

2.8.1 Medical imaging modalities

Nowadays, we can obtain sufficient information from imaging techniques for the cardiovascular system. Although, there is a variety of cardiac imaging methods available, their effective usage requires knowledge and expenses. We are going to overview some of the basic and best techniques.

Computerized Tomography (CT) (Figure 2.15), standing for Computer Tomography, also called Computerized Axial Tomography (CAT) imaging. It uses x-rays to project images of the body from different points of view. Acquires a 3D dataset that depicts the hole thoracic cavity, where we can obtain a clear view of the cardiovascular system. There are 2 different groups of CT devices: fan beam and cone beam.

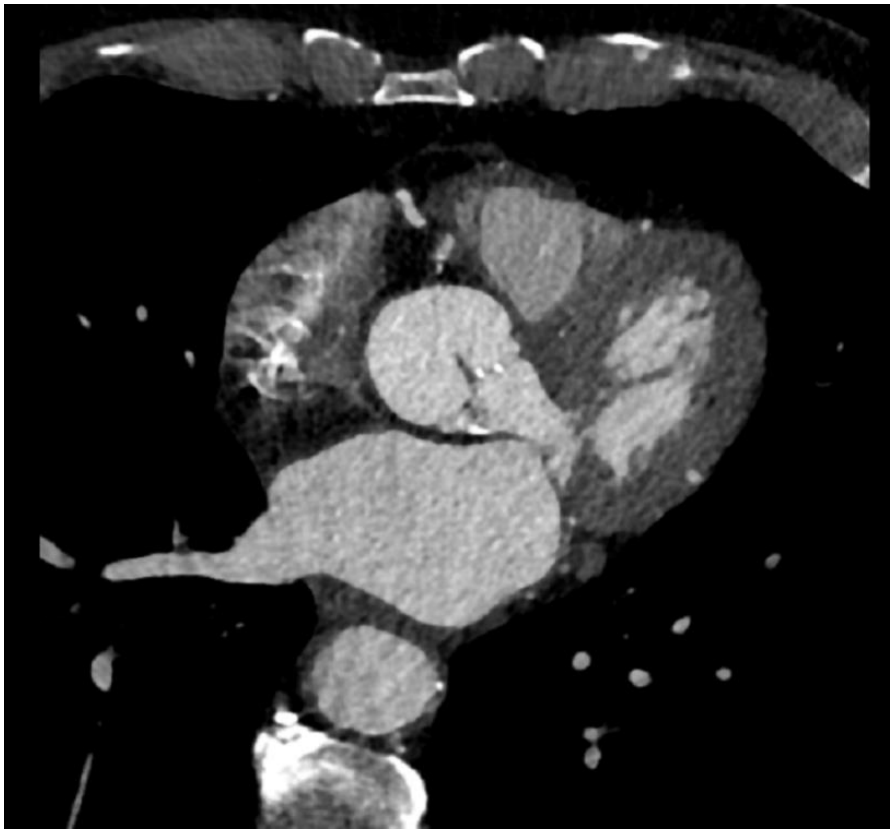

Figure 2.15. Typical CT scan depicting at the center of it the LA cavity with the right superior PV and the other chambers.

The cone-beam systems are used mostly by dental therapists. At fan beam a circular metallic frame rotate around the patient where the body is at a horizontal position upon a table. The table passes through slowly the center of the CT machine. The procedure causes no pain, but some tests need a contrast enhancement liquid to make some parts of body to be depicted better in the image. Some disadvantages of CT scans are:

- Expensive
- Not available in every
- Skips lesions far away from the sections
- Extrinsic objects like restoration and prosthetics create artifacts
- CT data are insufficient compared with other soft tissue imaging techniques

Specially for the LA chamber we can access the atrium and the pulmonary venous anatomy with the surrounding tissues. As a result, cardiac CT has become the investigation of choice before and after atrial fibrillation ablation. At the present thesis we use CT datasets to render the images of the LA and LAA views and extract the 3D geometry.

Magnetic Resonance Imaging (MRI) (Figure 2.16), is a unique imaging modality that can obtain 3D anatomy and blood characteristics, without using ionizing radiation. Its functionality

is based on achieving resonance signal from the hydrogen nucleus. It's actually imaging of water in the tissues. MRI method produces the highest contrast resolution as a medical imaging technique. Radio waves are directed to a specific location for examination in a magnetic field. The energy produced from hydrogen atoms in the cells stimulated by radio waves are converted to numbers and then by computer processing they are converted to images.

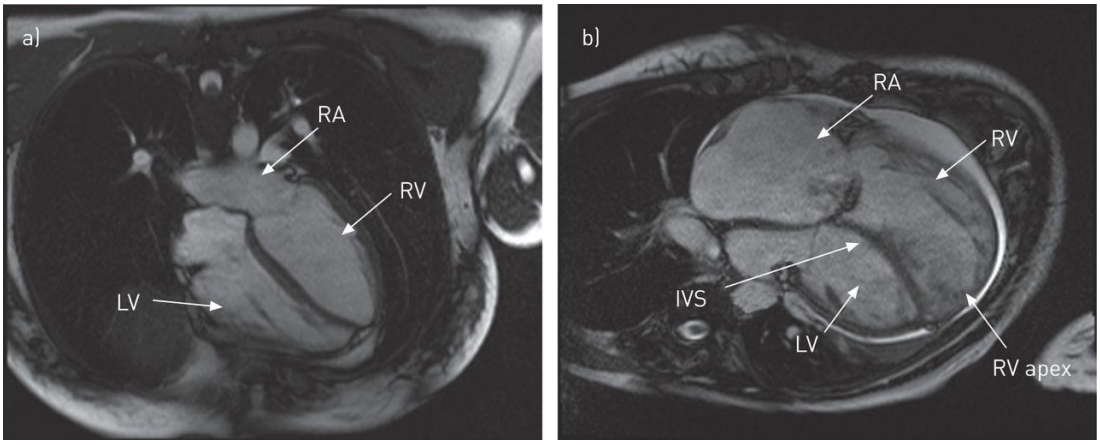

Figure 2.16. Typical MRI imaging depicting all the four chambers of the heart.

Ultrasound, imaging is one of the oldest techniques in clinical practice for more than a half century. It is portable, inexpensive and has quite good temporal resolution. The principles of ultrasound imaging are quite simple. A wave reflects partially at the interface among tissues with different impedance. The ultrasound and the reception of the reflected wave is generated from a piezoelectric transducer. The major aspect of ultrasound is to visualize tissues but also to provide feedback about blood and myocardial velocities. Velocity imaging was initially based on the Doppler effect and is often referred as Doppler imaging. However, this image modality has lower resolution compared to CT or MRI.

Transesophageal echocardiography (TEE) (Figure 2.17), uses high frequency sound waves (ultrasound) to make detailed pictures of heart at arteries. In comparison with a standard echocardiogram, the transducer that produces the sound waves for TEE is attached to a thin tube that passes through the mouth, down to throat and into the esophagus. The esophagus is very close to the structures of the upper heart, very clear images can be obtained. TEE can offer unique imaging resolution of the left atrium and left atrium appendage. Hence, TEE has been extensively used as a tool for embolism detection. "TEE is the most extensively used and accepted imaging modality to diagnose the existence of LAA thrombi" *Beigel et al.* [26] described. In this thesis TEE data is used to extract the velocity profiles from the pulmonary veins. This topic would be discussed more extensively in the next section.

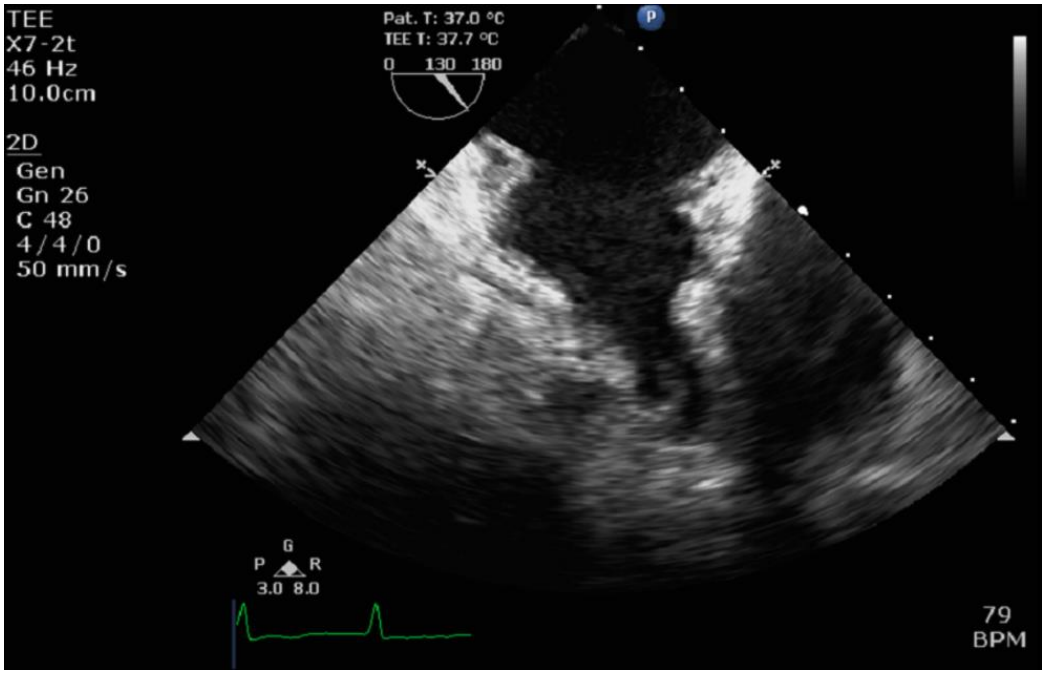

Figure 2.17. TEE imaging depicting the left atrial appendage.

The use of Transesophageal Echocardiography has made the clear imaging of the LAA possible, and measurements of its size, shape, flow patterns are proficient. Medical experts usually choose the modality which stands better for the patient and the exams that should be done depending on the seeking pathology. CT is faster procedure than MRI, plus if someone feels uncomfortable in small spaces MRI is not a good option. CT scan is used mostly to depict stiffer tissues (bones) than MRI (brain). Also, with MRI fluid motion and characteristics can be detected. Although no modality, whether is invasive or noninvasive in vivo or in vitro, for measuring physiological parameters is perfect. It depends as we referred above to the factors we are seeking for, on the area where the tissue lies and the disease we are investigating. Although, the need for high speed, density and small sizes of tissues has driven the development of 3D imaging. The future of medical imaging seems to be more flexible and faster with robotic devices [27].

The acquired images (usually 3D cohorts of 2D stacks) must be processed to be able for usage. The standard global protocol used for communication and storage of medical image data is the DICOM (Digital Communication in Medicine) format.

Chapter 3. State of the art

Some decades ago, cardiac computational models were very simple (1D, 2D) and they were used for computational simulations, implementing electrical activity or cardiovascular dynamics. Nowadays, 3D cardiac models have been introduced and they are becoming more and more complex as their applications are employed at different areas such as fluid dynamics, image segmentation, statistical modeling, patient risk stratification even surgical planning. Due to the evolution of computing resources 3D models have led us to more reliable and advanced computational simulations of cardiac electrophysiology or mechanics.

There are many studies in the literature which are concerning the hemodynamics of the cardiovascular system, but most of the times the geometries are separated chambers (e.g LV without the atrium or the MV as inlet, instead a rigid tube is used) or oversimplified models. The most studied part of the heart is the left ventricle (LV) as this chamber is the most susceptible to dysfunction. The LV is the strongest muscle of the heart as it is responsible for pushing through the blood to the rest body. Due to its role, LV is more prone to diseases and dysfunctionalities such as hypertrophic cardiomyopathy (HCM) and dilated cardiomyopathy (DCM). Although, the left atrium is less investigated as its functionality is still not clear to us, but always the adoption of this chamber was that it is just a pre-stage of the LV filling. The latest decades medical studies have turned their interest to investigate the role of left atrial appendage at clot formation.

3.1 Blood flow modeling

Several studies develop different approaches to reduce the risk of clot formation. Most of them involve physical separation of the LAA from LA as *Salzberg et al*. did at their study [28]. On the other hand, there are few studies focusing on developing LAA occlusion devices which are implemented at the orifice area of the LAA, trying to keep the path closed, so the blood flow doesn't pass through the appendage to diminish the risk of thrombus formation. Such techniques reduce the risk of thrombus formations as their role is to obstruct the flow of clots which already have formed at LAA through the atrium [18-19] or to obstruct the blood flow inside the appendage. Therefore, except from the devices to prevent thrombus, there are many anticoagulant therapies, such as warfarin [26]. These therapies have significant complications in 1-2% of patients. Although, a variety of specific procedures have been proposed to overcome these problems. In practice all the procedures are known, but they last a long time and they are complex, so most of the times the results are severe dangers.

As for blood flow modeling, there are few studies focusing on the left atrium. The first study was employed by *Di Martino et al.* [31] where they simulated the dynamics of the left atrium. They used porcine CT imaging data to construct a 3D atrial model and they investigated the electrophysiology of left atrium. Their results indicated heterogeneous stresses in the atrium, as the highest stress concentrations occurred in the posterior region close to the pulmonary veins. Afterwards, *Tomohiro Otani et al.* [32] did a great work developing a 3D LA model using CT images. They implemented a feasible methodology to perform personalized blood flow analysis, using the LA endocardial surface motion as boundary condition. *Vijay Vedula et al.* [33] studied the impact of the hemodynamics in the LA and its effects on ventricular flows. He used 4D CT scans exploiting them to implement also different cardiac cycle phases. *Michael Markl et al.* [34] used 4-D MRI data to characterize the flow dynamics in LA and LAA in patients with atrial fibrillation and *Alessandro Masci* [35] did the same using CT data and implementing a better methodology for the 3D reconstruction of the model. *Filippo Menghini* analyzed the hemodynamics in a LA numerical model focusing on possible transitions to turbulent flow. Although their models lack of details and the appendage shape and PV areas are oversimplified. *Ori Hazan et al.* [36] from one aspect did a pure engineering study but, on the other hand from clinical aspect had the worst model. His model is super simplified instead of the fact that he uses CT scans to reconstruct the appendage. The appendage morphologies were reconstructed, but they lack of reliability. *Satriano et al.* [37] did a mechano-electric finite element model of the LA to study the electrical and the mechanical activity and functionality of the LA. *Bosi et al.* [38] in their study examined the hemodynamics inside the LAA in different morphologies. They used also CT scans as image modality for patient data and as for input data normal and AF conditions were simulated. Their methodology and their approach

are sufficient and overall, it's a well written study. At the end, a worthy mentioned study was developed by *Hunter et al.* [39], where they examined the distributions of the LA WSS. They used an electromechanical model to correlate the electric atrial activity with WSS findings at specific areas. Also, they developed an anatomical segmented atrial map, divided in 21 areas.

3.2 Segmentation of the left atrium

The reconstruction of a 3D anatomical model of LA and LAA is a difficult problem as many studies have shown. Most of the studies implement semi-automatic or manual methods to reconstruct 3D models, as other try to develop a fully automatic process pipeline with low accuracy results though. The segmentation of the LA is hard to obtain high accuracy as this chamber consists of five more parts attached to it (four pulmonary veins and the appendage). Also, the mitral valve (MV) where the atrium relates to the left ventricle is a though area to be separated, as the regions and the intensities there are similar. For validation purposes, most of the studies used major metrics such as average Dice Coefficient (DC) and average surface to surface distance (S2S), as some others compare their results with manual segmentation findings.

Tao et al. [40] proposed a fully automatic process, using a dataset with late gadolinium-enhanced (LGE) MRI images. Their method consists of two steps where a global segmentation is applied using a multiatlas registration, as afterwards, a local refinement implemented using 3D level-sets. They compared their results with manual segmentation and the results showed a comparable performance with the manual process. Afterwards, *Chao Ma et al*. [41] proposed an approach with a combination of random forests (RFs) and active contour model, to develop a fully automatic segmentation process. They used the RFs to integrate effectively contextual and appearance information from different multisource images together for LA shape inferring. Afterwards they identified the tissue probability maps for the LA structure, they used a voxel-wise classification combined with a contour evolution scheme, in order to refine the structure labels. *Moreover, Valinoti et al.* [42] proposed a fully automatic approach to build a 3D patient-specific LA model including the PVs. They used MRI imaging data applying an edge based level set method to obtain the 3D model. Their results were compared with manual segmentation with S2S metrics. Although, their final reconstructed model lacks of smooth surface as it is consisted of a big stack of plates. Also, there are some other studies [43] were they focus to segment and reconstruct only the LAA excluding the rest of the LA body and the PVs, so they can focus their analysis only at this cavity.

3.3 Generic models

The first attempts to develop cardiac computational models resulted in simplistic geometrical shapes. Most of the times, the geometry included only LV, represented by confocal ellipsoids

which tried to approximate the shape. However, this approach is has been using for applications where shape and realism are not the purpose [44].

The next step was the anatomical models, aiming to represent as much as realism they could, but they still lacked of anatomical detail due to their poor quality of the data used to construct them and of course the knowledge. They mostly used data of animals trying to manual segment histoanatomical images.

The rise of the Computer Aid Design (CAD) provided the ability to construct cardiac 3D models without any data of anatomical information. Instead, they used some basic parameter values such as chamber volumes from clinical literature, to create a virtual 3D geometrical model.

Atrium models started to grow later than ventricular did for several reasons (LV disorders and health issues). The main one though, was the atriums higher complexity.

3.4 Medical image-based models

The development of medical images and medical technologies gave the capability to construct much more realistic 3D cardiac models. Medical image-based 3D models were born due to the advance of techniques as CT and MRI which provided a breakthrough to structural and functional information. Afterwards the computational modeling raised and the trend towards personalized medicine have just started, resulting in the definition of "patient specific models". Cardiac atlases started to develop producing a big dataset of population with generated 3D geometries [45].

3.5 Our approach

The main goal of this thesis is the investigation of the blood flow at the left atrium. Specifically, we focus to investigate the blood flow inside the appendage and correlate different morphologies with the velocity findings. Our approach combined the image processing with the blood flow modeling with patient-specific modeling to enhance our study. The generated 3D reconstructed anatomical models provided high accuracy with an acceptable level of reliability. Through the executed blood flow simulations reliable estimations concerning the blood flow and the appendage morphologies. Different anatomical regions with a variety of the resulting calculations are detected. A few statistical results used to demonstrate potential differences. The author strongly believes that the current study with the developed approach, can provide applicable knowledge to a new field with impact on the society of Cardiology. To our best of knowledge there is no other study with so many patients using patient-specific data.

Chapter 4. Methodology for segmentation and 3D reconstruction

4.1 Image processing

Image processing is a technique that implements mathematical operations to process an image. A typical simple workflow to process medical images is:

DICOM images dataset → pre-processing → main process → export segmented object

In fact, the input image with the output is the same image depicting the same objects/structures with different means. A typical image frame is at the 2D space as its dimensions are x and y arguments that they correspond to a specific location of pixels in the image. Every value of x, y pairs represent the intensity of a pixel. In this thesis we implemented a segmentation process to segment the LA and the LAA to construct a 3D atrial model. In order to do that, we used 3D image CT scan sets to obtain a 3D volume. Instead of the typical 2D CT frame, the z dimension representing the number of frames was used. The z dimension represents the length of the image set which actually is the total number of the images = z.

4.1.1 Dataset

The dataset consists of cardiac Computed Tomography (CT) chest scans from 13 patients (male, female, age) acquired from SIEMENS CT VA1 DUMMYCT, at the Medical Center of Vanderbilt University. CT scans provide high quality geometrical data as each set consists of around 300 slices at 512x512 pixel. The slice thickness is 0.75mm and the pixel spacing is 0.4mm for each volume set. A contrast enhancement fluid method was used to obtain images with better intensity specifically at the LA and LAA area. We selected for the segmentation procedure to use the best quality series so our results would be as much accurate as possible.

Also, the affiliated medical experts provided us data for validation such as geometrical measurements of LAA. These data were used to reconstruct the segmented images, using the developed methodology.

4.2 Segmentation of left atrium

In this study we tried to develop a semi-automatic segmentation of the LA. In brief the process pipeline (Figure 4.1) follows the next steps. A contrast enhancement method was used according to [42]. Adapting the threshold is the first step after the contrast enhancement to improve the image quality and diminish the unwanted objects. Then a region growing method is applied to fill and select properly the LA area, to provide an initial contour. The obtained initial contour is fused with a quite different processed image frame to enhance the output. Afterwards, the fused image is given as input at the Gradient Vector Flow (GVF) snakes to export the segmented object. At the end, to reconstruct the 3D geometry, we extract the boundaries of the segmented objects as a *x, y, z* point cloud to interpolate them and construct the 3D anatomical model [43].

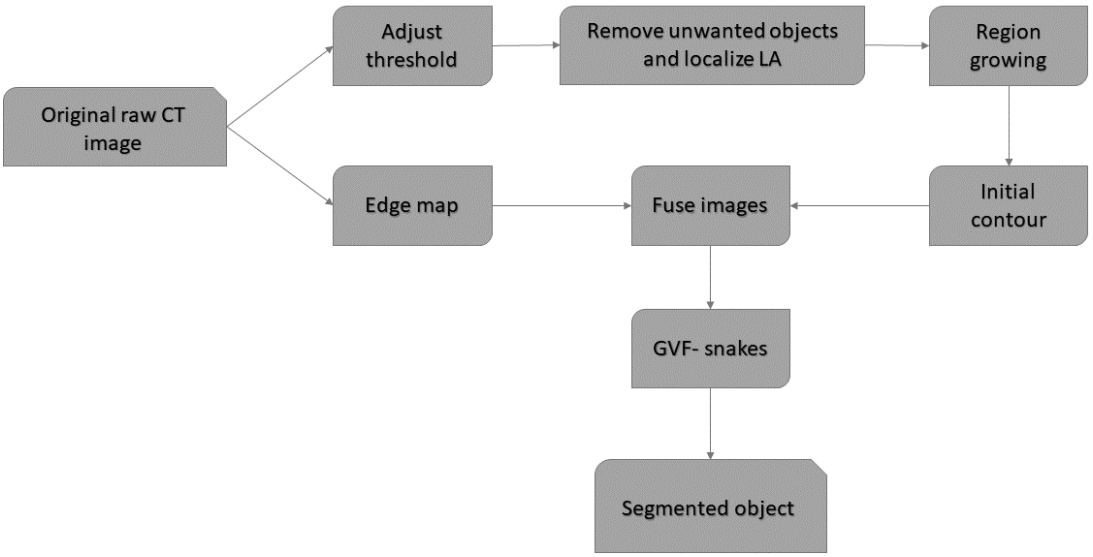

Figure 4.1. Segmentation workflow pipeline.

Particular attention was paid to the left atrial appendage, to achieve as much accuracy as it can be obtained by our approach.

4.2.1 Pre-processing steps

First, we want to resize the image as in the most cases the LA is located in the center of the CT image so, from 512x512 we reshape them at 255x255 as we can observe in Figure 4.2. This step is essential as the major issue here is to remove unwanted tissues such as bones, fat and lungs. The first shortcut of unwanted tissues is done. After that the next step is to convert the image to binary. This conversion allows us to remove (for second time) objects that are smaller

than the defined threshold. The binarization of the image, transforms the pixel's matrix at 0 and 1 values (black and white).

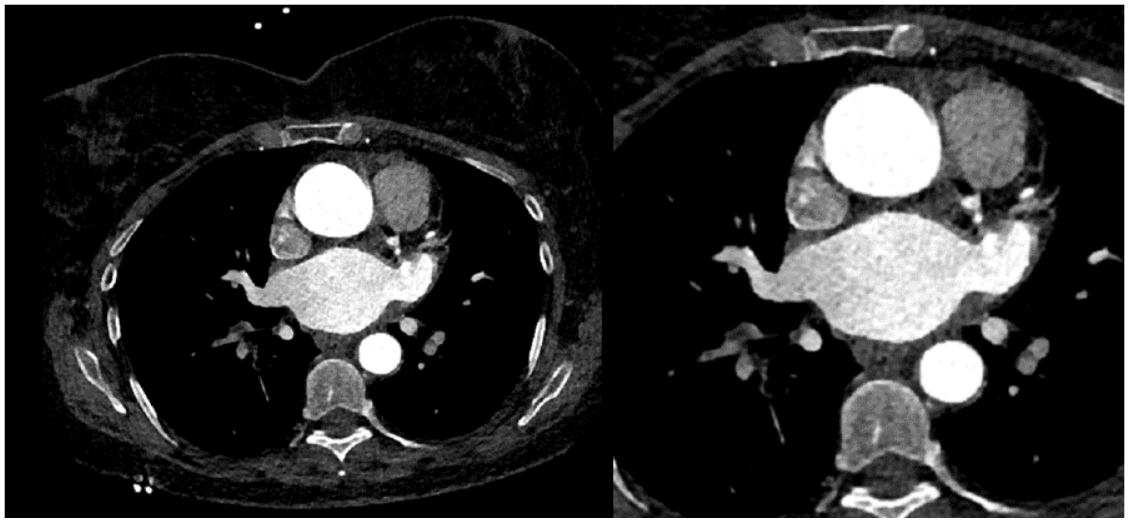

Figure 4.2. CT scan with contrast liquid resized from 512x512 pixels to 255x255, to center the LA.

4.2.2 Edge detection

Edge detection refers to mathematical methods that their scope is to identify objects on an image, that have different features or discontinuities. It is a fundamental image processing tool that can provide feature detection and extraction for a digital image.

$$H_{ij} = \frac{1}{2\pi\sigma^2} exp\left(\frac{(i-(k+1))^2+(j-(k+1))^2}{2\sigma^2}\right), \quad (4.1)$$

4.2.3 Intensity transformation

Intensity transformation can be expressed by the following equation:

$$g(x,y) = T[f(x,y)], \quad (4.2)$$

where $f(x,y)$ is the original image and $g(x,y)$ is the result of transformation T. This transformation is applied on every pixel in the image.

4.2.4 Removal of background unwanted tissues

After we enhanced the image, we should subdivide it in meaningful regions. Most of the times medical images are affected by noise or small tissues that may interfere the quality of the results even if the overall quality of the image is good. For this reason, usually these areas are neglected with adjusting the threshold limit and diminishing the area boarders.

Figure 4.3 is depicting the detected boarders of the LA (centered) and the surrounding tissues.

Figure 4.3. Removal of the unwanted tissues on the background and the segmentation mask.

4.2.5 Contours

Since the different tissue areas correspond to different grey intensities on medical images, a simple approach to extract meaningful areas is the creation of corresponding surfaces. This technique is known as contouring and it can be implemented both in 2D and 3D images. Next, we are going to give an overview of the most used algorithm "Marching cubes". *Lorensen et al.* [46] were the first to propose the marching cubes algorithm trying to construct a polygonal surface located on an interface of a scalar field sampled on a regular grid. A specified contouring level can label grid vertices, voxels on the image. A preliminary set of voxel-wide cubes is defined by eight neighboring voxels, the algorithm can identify the intersected cubes intersected by the isosurfaces of interest. The fundamental concept of marching cubes algorithm is that every cube can be partitioned by a set of triangles whose vertices lie on cube edges. The specific position of the triangle vertices is successively computed by linear interpolation of voxel scalar values on the cube vertices. Figure 4.4 depicts the results from the region growing we implemented.

4.2.6 Parametric deformable models

The deformable models are consisted of surfaces and curves that are be able to be deformed when there is a presence of an external and internal forces. Deformable models can be classified into two major categories:

- The classic energy minimizing model
- Shape constrained surface models

Active contours and Snakes are some of the simplest deformable models.

4.2.6.1 Snakes

Active contours are also known as snakes, is a common employed solution at a 2D image segmentation. Snakes are parameterized curves which are evolving based on image features. They can be described by a Lagrangian frame as:

$$\begin{matrix} U \\ s \end{matrix} \times \begin{matrix} \mathbb{R}^+ \\ t \end{matrix} \to \mathbb{R}^2, \tag{4.3}$$

where $U \subset \mathbb{R}$ e.g [0, 1] and $s \in U$ is the curve parameterization. The development equation for snakes can be derived from the minimization of the energy function as:

$$E_{snake}(C) = E_{smooth}(C) + E_{image}(C), \tag{4.4}$$

where

$$E_{smooth}(C) = \int_0^1 [w_1 |C_s|^2 + [w_2 |C_{ss}|^2]\, ds, \tag{4.5}$$

Is the internal deformation energy and:

$$E_{image}(C) = \int_0^1 w_3\, P(\boldsymbol{C})\, ds, \tag{4.6}$$

is the driving energy. In order to minimize the functional E(**C**), the active contour **C**(s) must satisfy the Euler-Lagrange equation as:

$$-\frac{w_1 \partial \boldsymbol{C}_s}{\partial s} + w_2 \frac{\partial^2}{\partial s^2} + w_3 \nabla P(\boldsymbol{C}) = 0, \tag{4.7}$$

As a substitute of using an energy gradient algorithm to configure what minimizes E_{snake} it is possible to adopt a development for making the snake evolve in time toward a configuration satisfying the Euler-Lagrange equation resulting in the evolution equation:

$$\frac{\partial C}{\partial t} = w_1 \boldsymbol{C}_{ss} - w_2 \boldsymbol{C}_{ssss} - w_3 \nabla P(\boldsymbol{C}), \tag{4.8}$$

4.2.6.2 Level sets

Most of the deformable models cannot deal with topological changes. For that reason, *Osher et al.* [47] introduced the level set techniques as an alternative approach to parametric deformable models. This approach allows us to overcome the limitations on topology and large deformations. Level sets indicate how evolving curves or surfaces are modeled. The level set of a real function φ of n variables is a set of:

$$\{(x_1, \dots\dots, x_n) | \varphi(x_1, \dots\dots, x_n) = c\}, \tag{4.9}$$

where c is constant. The approach of the level set, takes the primal surface and adds an extra dimension of time t. The new function is a hypersurface which is allowed to move upon the gradient field. At any time, the first level set of the hypersurface defines the growing surface. A preliminary closed surface C, can implicitly represent the zero-level set of a higher dimensional function $\varphi\ (x, y, z)$ as:

$$C = \{(x, y, z) \mid \varphi\ (x, y, z) = 0\}. \tag{4.10}$$

The user most of the times defines the initial surface as $\varphi(x(0), y(0), 0) = 0$. Afterwards, the higher dimensional function $\varphi\ (x, y, z)$ can be generated by a representation of it as a signed distance function of the surface:

$$\varphi\ (x, y, z) = \pm d(x, y, z), \tag{4.11}$$

where $d(x, y, z)$ is the Euclidean distance from φ to the surface C. The surface points are $\varphi\ (x, y, z) = 0$, where the outside points are assigned with (-) and the points inside with (+). After the determination of the hypersurface C the equations of its expansion can be formed.

4.2.6.3 Region growing

A 3D region growing technique was used with a given input seed point. The seed point was given with a x, y pixel values inside the script for the automatic purposes. Starting from the seed point, neighborhood voxels that satisfy the intensity criteria are starting to connect to it. The preprocessed image is used as an initialization step to develop the contours. Any unwanted regions and tissues were removed using a subtraction method as we mentioned before. However, because of the left atrium's position, a lot of interfaces take place. First, the interaction between LA and LV trough MV must be defined. These regions have exactly the same intensities, so we assume that this boarder is defined manually.

$$intmin < optimal\ threshold < max\ value\ threshold$$

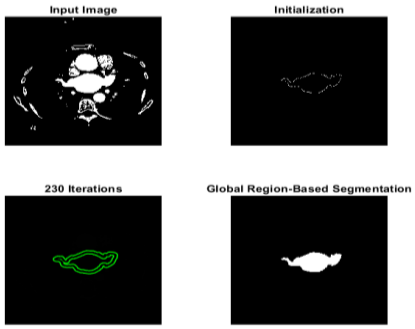

Figure 4.4. Contours growing with the automatic approach, having as feed input the x, y values of the ROI.

The basic equation for the region growing method is:

$$\cup_{i=1}^{n} R_i = R, \tag{4.11}$$

where R_i is a connected region, *i= 1, 2, 3 …n.*

4.2.6.4 Gradient Vector Flow (GVF)

Here we are going to describe the GFV-snake approach. Active contours were introduced by Kass et al. [48]. The method tries to minimize the energy function consisting of an external force (E_{ext}) and an internal force (E_{int}) equation 4.12:

$$E = \int_0^1 E_{int}\ \big(X(s)\big) + E_{ext}(X(s)), \tag{4.12}$$

where s represents along the contour $s \in [0, 1]$ and X denotes the active contour. The initial energy is given by:

$$E_{int} = \frac{1}{2}(\alpha|X'(s)|^2 + \beta|X''(s)|^2, \quad (4.13)$$

where α and β are the weighting parameters to control the snake's tension and rigidity. The external energy function E_{ext} represents the negative gradient magnitudes of the image. A new deformable model named Gradient Vector Flow snake was proposed by [49] to overcome the limitations of the traditional snakes. This model uses the GVF as external force by implementing a vector diffusion equation to diffuse the gradient edge map from the image. The first step is to calculate the edge map of the image [50]. Figure 4.5 demonstrates our approach that we used to enhance the final contour, combining a background mask with a foreground edge map.

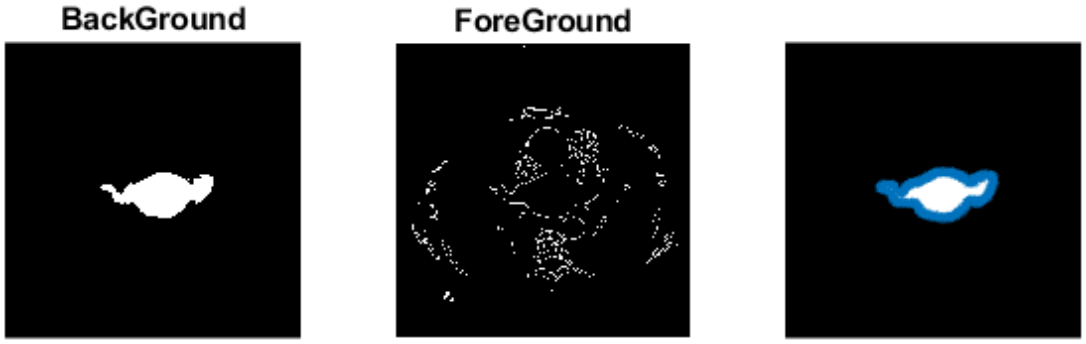

Figure 4.5. GFV method to enhance the output contour where the point cloud is going to be calculated.

After all the above steps, the generated contour is going to be used for the extraction of a polyline representative for each slice of the dataset. The iterative automatic process calculated and extracted all the polylines from the borders of the segmented masks. These points are connected, with a manual process, with triangles to generate the 3D geometry.

The approach that we described above was implemented by a developed in-house Matlab code (Mathworks) for that purposes.

4.3 Reconstruction

Imaging modalities and techniques (Chapter 2) have helped clinicians to diagnose and plan better strategies to treat diseases. The main task of the clinicians and medical experts is to analyze the acquired images and result to a diagnose or a treatment plan. The construction of 3D anatomical models can be described in several stages. Medical image segmentation is a branch of computer science that deals with the extraction of relevant and interesting features in images. The biomedical field uses these techniques to provide 3D patient specific anatomical models. CFD-based techniques are used to construct complex computer representations (In

Silico Models) in health and disease. First of all, there are two major categories of 3D models: 1) Patient specific 3D models, where the geometry is constructed from patient data, so the results after the analysis would be for that patient and 2) Idealized 3D models where the construction is based on mathematical formulas and topology visualizations to obtain a generalized ideal geometry, which practically its perfect. Latest fully automated techniques are used a lot, in order to save time and money for patients and medical experts. Segmentation of LA and LAA can be difficult as its anatomy is highly complex. At this thesis all the 3D model geometries are constructed from patient specific data. For this purpose, in this thesis a semi-automatic in-house code was developed and described below.

The segmentation of the atrium and specially with appendage included is more challenging than other structures in the heart. The shapes of the LA vary among different variations and its blood pool is consisted with other structures such as the appendage, the pulmonary veins, the surrounding pulmonary artery and the aorta. The difficult part here is that all the above-mentioned structures have quite same intensity which consists hard the segmentation of the LA area. Furthermore, LA's outlet mitral valve makes the boundaries between LA and LV almost invisible at most of the cases, setting this issue as one of the major problems of atrium's segmentation. As a result, segmentation of LA has attracted much more interest and progress, as LV or vessels have.

4.3.1 Geometry description

The LA consists of left atrium (LA) main body, the left atrial appendage (LAA), the mitral valve (MV) and the pulmonary veins (PVs). Blood inflows through the PVs and outflows through the mitral valve. The LAA is a highly complex anatomic structure situated in the lateral aspect of the LA. The PVs are four separate vessels with an average diameter 10mm. Their names stem from their position (RIPV, LIPV) as is indicated in [51], upper and lower PV left and right respectively. The LA is interconnected with the left ventricle (LV) by the MV, where which blood flows through, from the LA to the LV. Figure 4.6 presents an example of the reconstructed LA and LAA geometry.

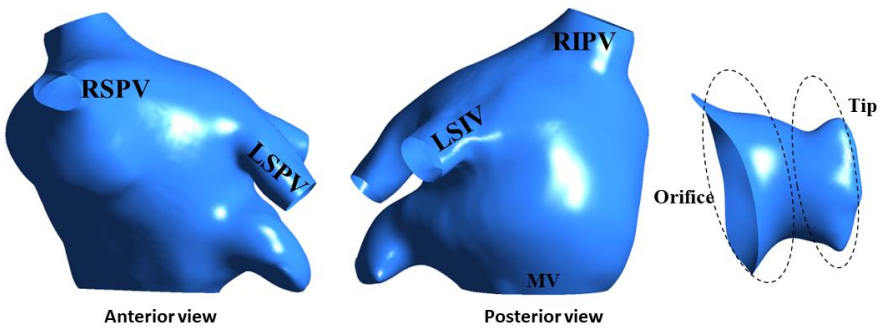

Figure 4.6. Reconstructed LA and LAA (orifice and tip areas) geometry with right and left superior (RSPV, LSPV), right and left inferior (RIPV, LIPV).

Table 1 are presented some extracted features for the generated atrial geometries and its appendages. In Figure 4.7 the reconstructed LAA geometries and their morphology are depicted for all the 13 patients.

Table 1. Left atrial appendage patient's anatomical morphologies.

Patient ID	Appendage morphology	LAA diameter (cm)	LAA length (cm)	LA volume (ml)
1	Cactus	1.63	2.92	164.5
2	Chicken Wing	2.18	2.23	144.9
3	Windsock	1.93	2.84	124.3
4	Cauliflower	2.52	2.28	217.17
5	Chicken Wing	1.72	2.97	116.86
6	Cactus	0.074	2.47	276.49
7	Windsock	2.49	2.54	178.9
8	Cauliflower	2.11	1.73	112.29
9	Cactus	2.85	2.82	116.77
10	Cauliflower	0.78	1.98	171.12
11	Chicken Wing	1.81	3.29	142.5
12	Chicken Wing	2.20	2.54	68.4
13	Windsock	1.97	2.66	99.8

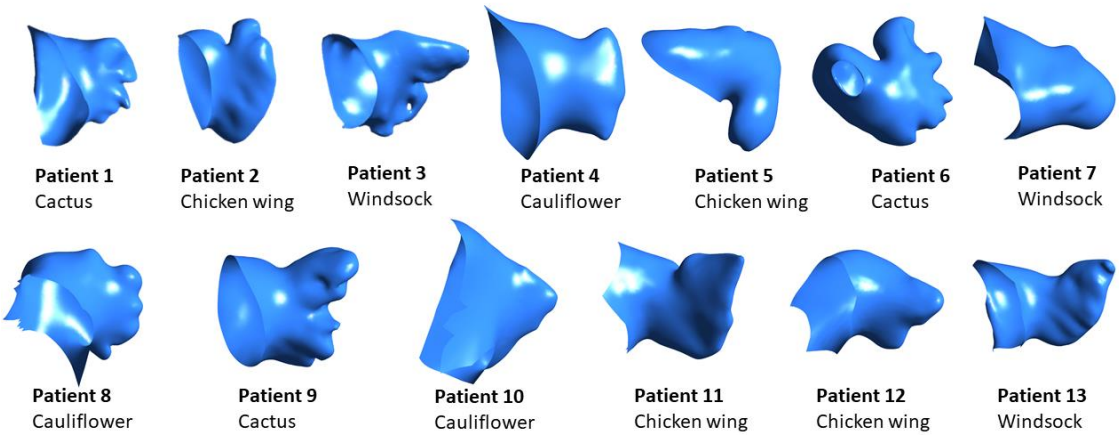

Figure 4.7. LAA morphologies.

4.4 Validation

To access the reliability of an algorithm and its effectiveness in medical research domain, the validation step is necessary. After the implementation of the segmentation, the reconstructed geometries were assessed by a medical expert. Also, the performance was executed comparing the algorithm's results with CT scan measurements provided by the medical experts. For

patient's 2 reconstructed LA and LAA, the LAA's tip length is provided 4.20 and we calculated it as 3.94 and their PV diameter provided as 2.84 and we calculated it as 2.95. All the above can be depicted in Figure 4.8, However, it is still difficult to obtain a ground truth area for each contour as most likely small differences will appear.

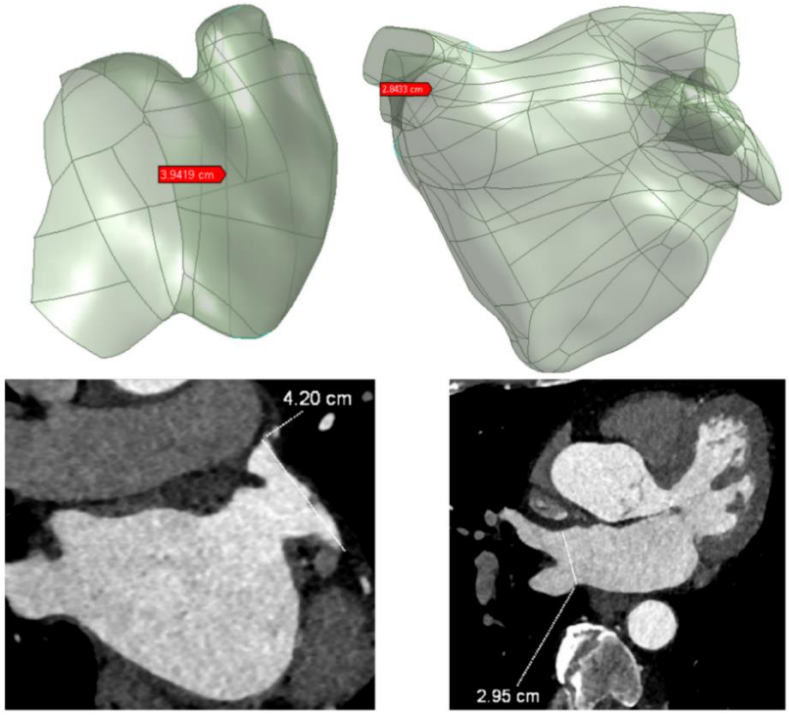

Figure 4.8. Extracted measurement of the reconstructed LA geometries.

Even if the same clinical expert does the same contour after a considerable amount of time, he will do it different and the above will be spotted.

4.5 Mesh generation

In order to set up a computational model for CFD meshing is must do preliminary step. Mesh or grid generation is a pivotal aspect of CFD. A fine grid is required in order to achieve a better convergence and to reduce as much as possible the numerical errors. The discretization of the domain, along with the choice of the kind and shape of elements used, play a key role in the computation of accurate solutions. Once the shaped surface boundary is constructed, the next step is to build the volumetric mesh. The discretization of the domain to small elements whose vertices called nodes, are the points where the solution, vectors and values of variety parameters. This mesh most of the times is consisted of unstructured tetrahedra due to their flexibility in filling volumes of complex shapes. In this thesis, all the 13 patients were discretized with tetrahedral elements as depicted in Figure 4.9.

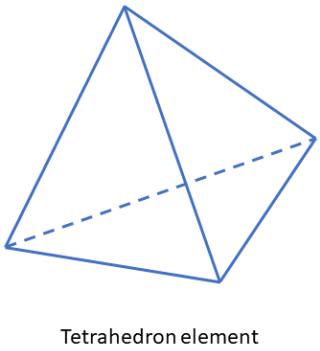

Figure 4.9. Tetrahedron element that used for the mesh generation.

A parametric bivariate function is been built as a collection of polygons which are typically triangles generated by Lagrangian shape functions or patches generated by high-degree polynomials such as NURBS (Non-Uniform Rational Basis Spline). Because of the no-slip condition (we are going to talk about it to the next chapter) the creation of layers with thin elements to the walls is needed to properly model the highly gradients at these regions. These layers are even more important when WSS must be computed, since the shear stress is a function of the velocity field as we can see at the next Chapter. More specifically we are going to use the inflation method as is depicted in Figure 4.10 to add extra thin layers to the walls, where we should specify the thickness, the grow factor and the number of layers.

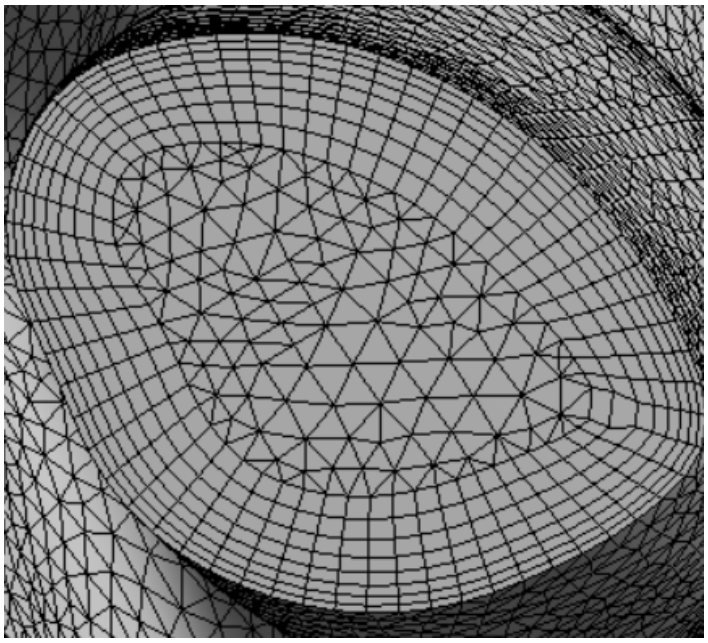

Figure 4.10: Pulmonary vein inflation technique to enhance the mesh quality.

4.5.1 Structured versus unstructured meshes

Numerical approximations such as FDM used mostly by structured meshes. This type of meshes follow a regular repeatable pattern of their nodes. Each interior node is always

connected to the same number of neighbor nodes. On the other hand, unstructured meshes don't follow a continuous pattern and their neighbors to a node changes from node to node. An example of such meshes is depicted in Figure 4.11. The data structures required to represent unstructured meshes are more involved as we need to store additional information to identify the neighbors or each node in the mesh. FEM and FVM are the most common used techniques in this type of meshes [52].

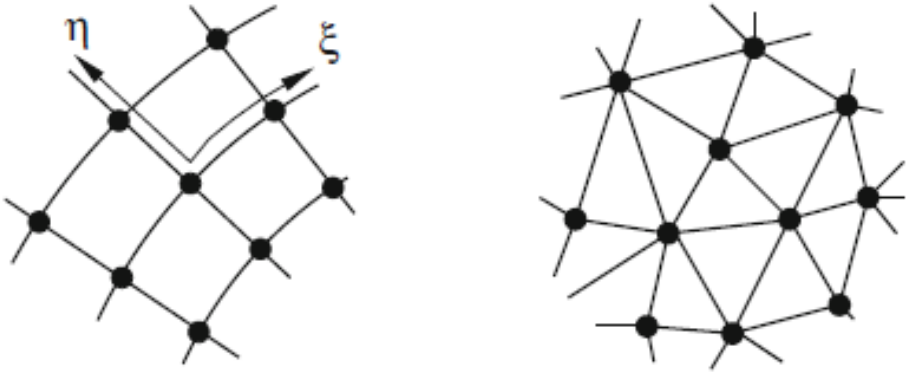

Figure 4.11: Structured and unstructured mesh.

Figure 4.12 depicts an example of patient's 2 meshed geometry is presented. We have generated an unstructured mesh with tetrahedral elements and inflation method at the atrial wall.

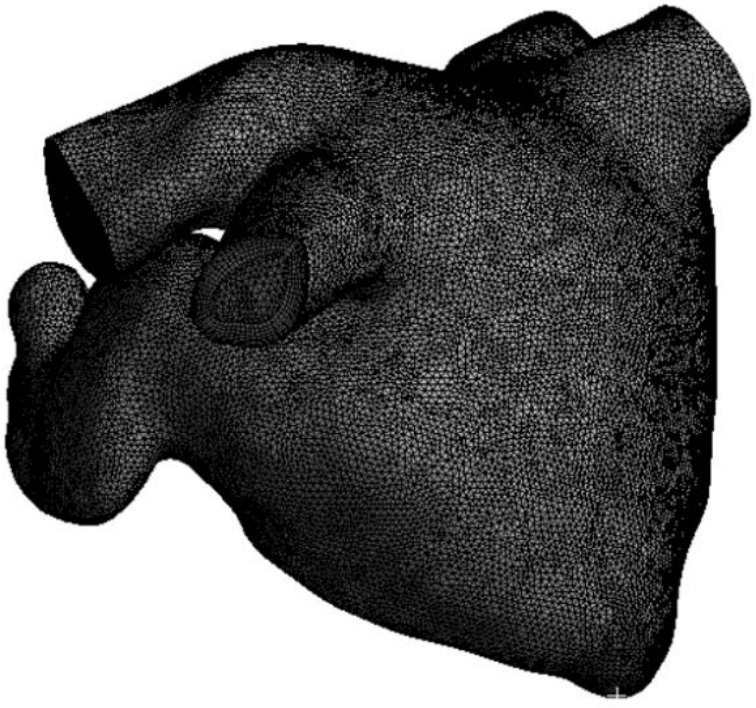

Figure 4.12: Left atrium's unstructured generated mesh.

4.5.2 Mesh quality assessment

The 13 reconstructed models were discretized into tetrahedral elements. The WSS values were used to check where the mesh converges. Also, an error analysis has been conducted. Orthogonal quality (OQ) (Figure 4.13) and skewness metrics were chosen to check the element quality.

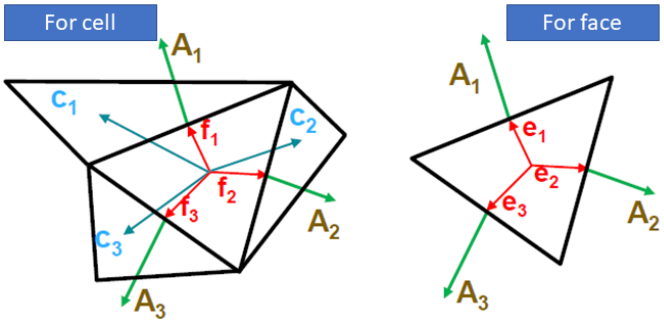

Figure 4.13. Orthogonal quality.

The OQ is derived from the solver which provides the discretization for each cell, for one cell it is the minimum of:

$$\frac{A_i}{|\vec{A_i}|}\frac{f_i}{|\vec{f_i}|} \qquad \frac{A_i}{|\vec{A_i}|}\frac{C_i}{|\vec{C_i}|} \; for\ every\ face\ i. \tag{4.13}$$

Every face is computed as the minimum of: $\frac{A_i}{|\vec{A_i}|}\frac{e_i}{|\vec{e_i}|}$ computed of each edge i. A_i is the face normal vector and f_i is a vector from the centroid of the cell to the centroid of that face, C_i is a vector from the centroid of the cell to the centroid of the adjacent cell, where e_i is the vector from the centroid of the face to the centroid of the edge. The range of the orthogonal quality is 0-1, where values equal and neat to 0 mean bad quality and 1 mean good. Figure 4.14 we are presenting an example of patient's 2 OQ metrics results.

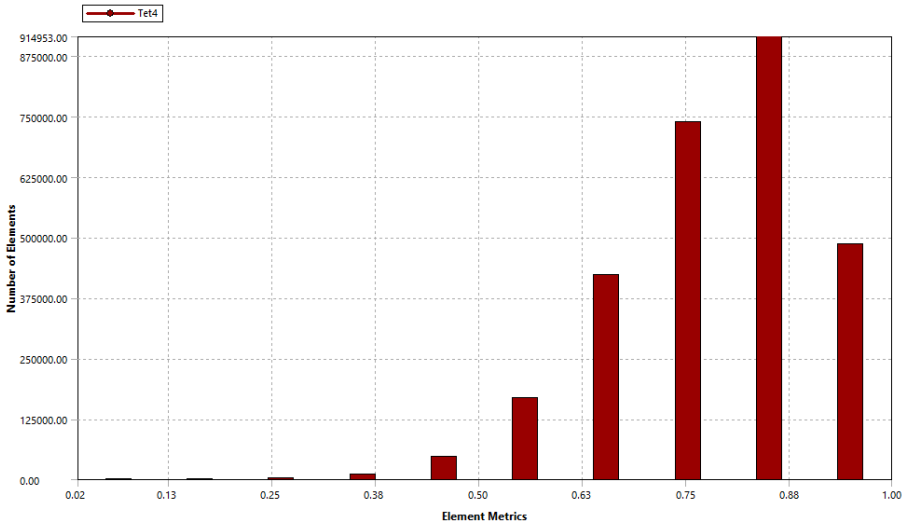

Figure 4.14. Orthogonal quality metrics from patient's 2 generated mesh.

On the other hand, the skewness (Figure 4.15) metric has the opposite range where 0 means good and 1 bad. There are two methods to determine the skewness as we can observe them in Figure 4.15.

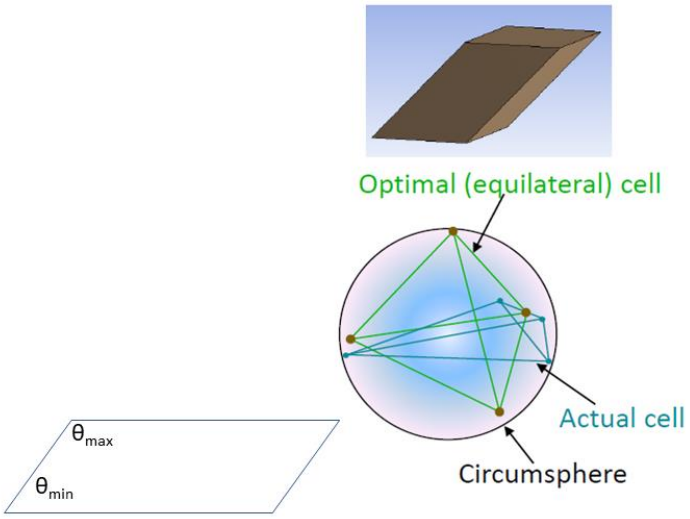

Figure 4.15. Skewness quality.

Equilateral volume deviation which applies only for triangles and tetrahedron elements:

$$skewness = \frac{optimal\ cell\ size - cell\ size}{optimal\ cell\ size} \tag{4.14}$$

The normalized angle deviation:

$$max\left[\frac{\theta_{max}-\theta_e}{180-\theta_e}, \frac{\theta_e-\theta_{min}}{\theta_e}\right], \tag{4.15}$$

where θ_e is the equiangular face/cell. Figure 4.16Figure *4.14* we are presenting an example of patient's 2 OQ metrics results.

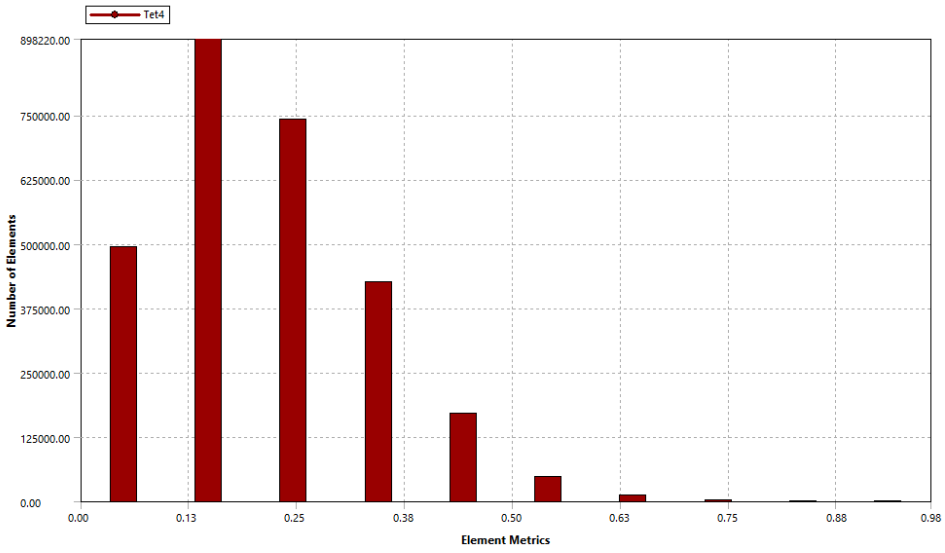

Figure 4.16. Skewness metrics from patient's 2 generated mesh.

Chapter 5. Numerical formulation

The major general approach of CFD involves as much the discretization of the equations as the 3D geometry (to adopt a fine grid). As we mentioned above discretization is performed most of the times using mesh techniques to divide the geometrical volume of the model into smaller parts. This kind of mathematical models are kind of complicated so they cannot be solved analytically in general. For this reason, a lot of numerical techniques are resorted to obtain approximated solutions. The mathematics of CFD solvers are described from the major Navier-Stokes equations which are formed by the momentum and mass transfer equations. These partial differential equations have no known general analytical solutions, but they can be solved and discretized numerically. By this way the equations of motion are expressed as discrete algebraic form at each node of the grid, so that the computer can solve a system of equations rather than continuous equations at lots of points that form a volume. The discretization methods follow special rules and they are not peremptory, depending on what technique is employed (e.g finite-element, finite-volume). The techniques we chosen, were implemented that way so numerical instabilities and errors are avoided or minimized. These instabilities can lead the results that deviate from actual solution. To avoid that, a wise and experienced choice of techniques and number of elements is needed. A basic consideration when designing a model of blood flow is blood-tissue interactions. Blood in most cardiovascular segments is contained inside tissues (e.g arterial or cardiac walls).

5.1 Numerical solution of partial differential equations

Most models used in numerical simulations are based on Partial Differential Equations (PDEs) for an unknown u (scalar or a vector) expressed with the general form:

$$\frac{\partial u}{\partial t} + L(u) = f,\ in\ \Omega,\ 0 < t < T, \tag{5.1}$$

where L indicates a differential operator in space of variable x. The equation will build up by proper initial and boundary conditions. If the problem is steady time derivative is not present. The time T indicates the final time of our simulation, as the numerical approximation deals with a bounded time interval problem. One of the most common techniques to solve numerically PDEs, is the subdivision of the computational domain Ω to a grid (mesh) as we mentioned before. The solution u is replaced by an approximation u_h at each node of the grid. The h index indicates the grid spacing. If the problems are time-dependent, time approximation is necessary.

The most common and accurate technique to solve numerically a PDE, is to divide the computational domain Ω into a grid. An u_h approximation replace the solution u. The pedix h is the grid spacing.

At time-depended problems the approximation of time should be included by typically and iterative method that from the knowledge of the approximation u_h^n at a time t^n for $n = 0,1, \dots n$ builds the approximation u_h^{n+1} at time $t^{n+1} = t^n + \Delta t$, being $\Delta t > 0$ a chosen timestep.

The discretization step must be considered first. The most common methods are Finite Difference Method (FDM), Finite Volume (FVM) and Finite Elements (FEM). We are going to use the FVM method here at this thesis.

5.2 Theory for solver

The component that provide us the solution is called solver. The basic steps to solve a CFD problem are:

1. Integration of the partial differential equations over all the control volumes in the region of interest.
2. A system of algebraic equations is formed from these integral equations by generating a set of approximations.
3. Iterative solution is applied to solve the algebraic equations.

The iterative approach is a must be, because of the non-linearity of the equations and as the exact solution is approached the solver is said to converge. Many factors are crucial to obtain an exact solution such as size and shape of control volumes. Many physical processes are being modeled using empirical relationships.

Visualization (or Post-processing) of the solution is a very important feature to present results interactively. Some important features of post-processing are (Figure 5.1):

1. Visualization of the 3D geometry.
2. Vector plots that provide us magnitudes and directions of the flow.
3. Visualization of scalar variables through the 3D domain.
4. Numerical calculations.
5. Animations.
6. Charts with graphical plots of variables.

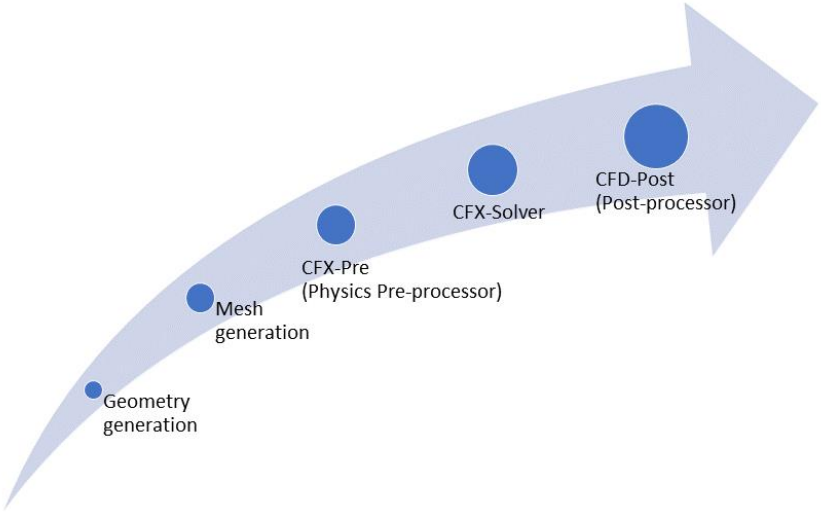

Figure 5.1: Pipeline of the CFD solver for the blood flow modeling.

5.3 Solver setup

All the steps executed here are supposed to provide us a stable converged solution. Some of the most important for reference are domain definition, the boundary conditions, model selection to solve the flow, the material properties, timesteps (we implement transient simulations), the max number of internal iterations for convergence control and the Root Mean Square (RMS) for residual level [53]. At this Chapter we analyze the RMS and the rest of the parameters are presented at the next Chapter.

A critical parameter to measure the local imbalances of each control volume is the residuals. Is the most accurate measure of convergence as it indicates whether or not the equations are solved accurately. The residual is used to automatically stop the CFX solver when the specified target is reached. In transient simulations has quite the same role but instead of stopping the solution, it terminates the coefficient iterations. If the number of iterations per timestep is large such as 20, then when the residual reaches the specified value, the iterations will stop before they reach their maximum number. The required convergence level depends on the model and the user's specified requirements. The guidelines below must be followed to obtain convergence:

- To obtain enough qualitative understanding of the flow the RMS values must be greater than $1e^{-4}$.
- $1e^{-4}$ is a slack number for convergence, but it may be sufficient for many engineer applications.
- $1e^{-5}$ means good convergence and most of the times sufficient for most engineering applications.
- $1e^{-6}$ or lower mean very tight convergence and most of the times is used for geometrical sensitive.

We specified the RMS number to be $10e^{-4}$.

Another important factor is the Courant Number, where we can't interfere directly but indirectly. That means we can't specify Courant Number value, but we can force other parameters such as mesh quality, which interact immediately with it. Courant Number is a value which indicates the amount of flow and its transition from a computational grid cell at a specific time step. For the explicit Eulerian method, the Courant Number should not be greater than 1. If it is greater than 1 that indicates that the flow passes more than one grid elements at each timestep and as a result the time integrator has no chance to obtain accurate solution. Also, the value we can provide us feedback about the transition from element to element if is smooth or not. The Courant Number is in one dimension expressed as:

$$C \equiv \frac{u\Delta t}{\Delta x} \tag{5.2}$$

Where u is the velocity of the fluid, Δt is the time step value and Δx is the internal spacing of two grid elements from their center point.

5.4 Governing equations

Blood can be modeled by mean of Navier-Stokes for incompressible Newtonian fluids [52]. To obtain the numerical solution by CFD a "few" governed equations of mathematical models are solved. These mathematical models are the governing equations of fluid flow which are based on the conservation laws of physics. There are three major equations in order to solve the velocities in 3D and the pressure at the fluid problem.

Conservation of mass

The conservation of mass for a fluid is based on the mass balance:

$$\frac{\partial}{\partial t}(\rho \delta x \delta y z) = \frac{\partial \rho}{\partial t}\rho \delta x \delta y z, \tag{5.3}$$

The mass flow rate is a result of density, area and velocity component to the face.

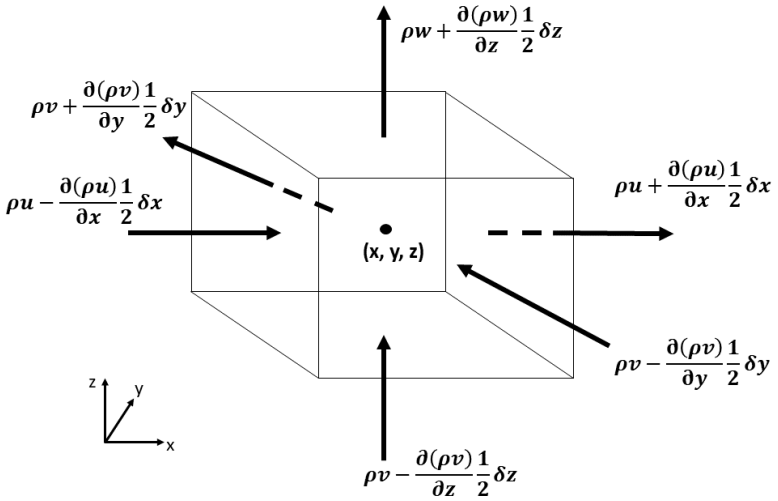

Figure 5.2: Conservation of mass.

$$\left(\rho u - \frac{\partial(\rho u)}{\partial x}\frac{1}{2}\delta x\right)\delta y\delta z - \left(\rho u + \frac{\partial(\rho u)}{\partial x}\frac{1}{2}\delta x\right)\delta y\delta z + \left(\rho v - \frac{\partial(\rho v)}{\partial y}\frac{1}{2}\delta y\right)\delta x\delta z - \left(\rho v + \frac{\partial(\rho v)}{\partial y}\frac{1}{2}\delta y\right)\delta x\delta z + \left(\rho w - \frac{\partial(\rho w)}{\partial z}\frac{1}{2}\delta z\right)\delta x\delta y - \left(\rho w + \frac{\partial(\rho w)}{\partial z}\frac{1}{2}\delta z\right)\delta x\delta y, \quad (5.4)$$

According to Figure 5.2, the net rate of mass flow into element is written. This equation indicates that the flow that is heading into the element, produce an increase of mass in the element. The sings are positive while it enters the element while they are negative when it leaves the element. The equation (5.4) can be transformed to:

$$\frac{\partial}{\partial t} + \frac{\partial(\rho u)}{\partial x} + \frac{\partial(\rho v)}{\partial y} + \frac{\partial(\rho v)}{\partial z} = 0, \quad (5.5)$$

$$\frac{\partial \rho}{\partial t}\nabla.(\rho.\vec{u}) = 0, \quad (5.6)$$

This equation is defined as unsteady 3D mass conservation or continuity equation at a point in a compressible fluid. If the flow is assumed to be steady state, then we have:

$$\frac{\partial}{\partial t} = 0, \quad (5.7)$$

When the fluid is incompressible the density is set to be constant and the mass balance:

$$\frac{\partial u}{\partial x} + \frac{\partial v}{\partial y} + \frac{\partial w}{\partial z} = 0, \quad (5.8)$$

We are going to use the equation (5.8) to define our fluid as incompressible and we obtain the initial conditions for the transient simulations from the steady results.

The momentum equation is based on the Newton's second law: "Rate of increase of momentum of fluid particle = Sum of forces on fluid particle". Firstly, we consider the x-components of

the forces due to pressure and the stresses components (τ_{xx}, τ_{xy}, τ_{xz}). The magnitude of a force from a surface stress is the result of the product of the stress and area.

As we can observe in Figure 5.3 the direction of the x coordinate is given in positive sign, as the negative signs are given from the opposite of x direction. The force components acting on the left and right faces are given as:

$$\left[\left(p-\frac{\partial p}{\partial x}\frac{1}{2}\delta x\right)-\left(\tau_{xx}-\frac{\partial \tau_{xx}}{\partial x}\frac{1}{2}\delta x\right)\right]\delta y\delta z+\left[-\left(p+\frac{\partial p}{\partial x}\frac{1}{2}\delta x\right)+\left(\tau_{xx}-\frac{\partial \tau_{xx}}{\partial x}\frac{1}{2}\delta x\right)\right]\delta y\delta z=\left(-\frac{\partial p}{\partial x}+\frac{\partial \tau_{xx}}{\partial x}\right)\delta x\delta y\delta z, \quad (5.9)$$

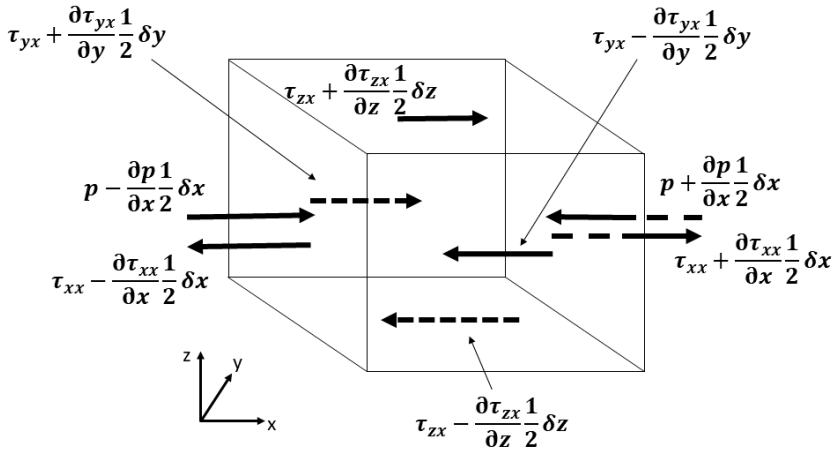

Figure 5.3: Conservation of momentum.

The force components in the x direction acting on front and back face are written as:

$$-\left(\tau_{yx}-\frac{\partial \tau_{yx}}{\partial y}\frac{1}{2}\delta y\right)\delta x\delta z+\left(\tau_{yx}+\frac{\partial \tau_{yx}}{\partial y}\frac{1}{2}\delta y\right)\delta x\delta y=\frac{\partial \tau_{yx}}{\partial x}\delta x\delta y\delta z, \quad (5.10)$$

The force components in the x direction acting on the faces at top and bottom are:

$$-\left(\tau_{zx}-\frac{\partial \tau_{zx}}{\partial z}\frac{1}{2}\delta z\right)\delta x\delta y+\left(\tau_{zx}+\frac{\partial \tau_{zx}}{\partial z}\frac{1}{2}\delta z\right)\delta x\delta y=\frac{\partial \tau_{zx}}{\partial x}\delta x\delta y\delta z, \quad (5.11)$$

$$\tau_{zx}-\frac{\partial \tau_{zx}}{\partial z}\frac{1}{2}\delta z, \quad (5.12)$$

$$\tau_{yx}+\frac{\partial \tau_{yx}}{\partial y}\frac{1}{2}\delta y, \quad (5.13)$$

$$\tau_{yx}-\frac{\partial \tau_{yx}}{\partial y}\frac{1}{2}\delta y, \quad (5.14)$$

$$\tau_{xx}-\frac{\partial \tau_{xx}}{\partial x}\frac{1}{2}\delta x, \quad (5.15)$$

Although, the total force at each unit volume of the fluid due to the surface stresses is the sum of the force components which are expressed in equations 5.12, 5.13, 5.14, 5.15:

$$\frac{\partial(-p+\tau_{xx})}{\partial x}+\frac{\partial \tau_{yx}}{\partial y}+\frac{\partial \tau_{zx}}{\partial z}, \tag{5.16}$$

The momentum conservation equation in x, y, z directions can be expressed as follows:

$$\rho\frac{Du}{Dt}=\frac{\partial(-p+\tau_{xx})}{\partial x}+\frac{\partial \tau_{yx}}{\partial y}+\frac{\partial \tau_{zx}}{\partial z}+S_{Mx}, \tag{5.17}$$

$$\rho\frac{Dv}{Dt}=\frac{\partial \tau_{xy}}{\partial x}+\frac{\partial(-p+\tau_{yy})}{\partial y}+\frac{\partial \tau_{zy}}{\partial z}+S_{My}, \tag{5.18}$$

$$\rho\frac{Dw}{Dt}=\frac{\partial \tau_{xz}}{\partial x}+\frac{\partial \tau_{yz}}{\partial y}+\frac{\partial(-p+\tau_{zz})}{\partial z}+S_{Mz}, \tag{5.19}$$

The S_M indicates the contribution to the body force per unit volume in the fluid. The stress tensor τ is related to the strain rate by:

$$\tau=\mu\left(\nabla\boldsymbol{U}+(\nabla\boldsymbol{U})^T-\frac{2}{3}\delta\nabla\cdot\boldsymbol{U}\right), \tag{5.20}$$

The momentum equation for viscus fluids, is formed as in Euler's equation where the power of inertia per unit mass. So, the Euler's equation suffices to add viscous force, so we have:

$$\rho\frac{D\vec{V}}{Dt}=-\vec{\nabla}P+\rho\vec{g}+\mu\nabla^2\vec{V}, \tag{5.21}$$

5.5 Finite Volume Method

There are a lot of methods whose usage is to obtain the approximated solution where the most common are Finite Difference Method (FDM), Finite Volume Method (FVM) and Finite Elements Method (FEM). Here we are going to use the FVM method as it combines a high geometrical flexibility (it can operate on arbitrarily complex geometries) with computational efficiency [52].

At this method (FVM) an integral formulation of the equation is been used. It can be employed whenever the operator L is written in the so-called divergence or conservation form that is:

$$L(u)=div\,\boldsymbol{F}(u), \tag{5.22}$$

where **F** is the flux vector depending on u and spatial derivatives of u. With a few manipulations at Navier-Stokes equations (see eq. 3) may be written in conservation form, where the momentum equation is formed as:

$$\boldsymbol{F}(u,P)=u\otimes u+P\boldsymbol{I}-\mu\boldsymbol{D}(u), \tag{5.23}$$

while for the continuity equation **F**(u) = u. Also, the above equation can be expressed at conservation form by exploiting the continuity equation $\boldsymbol{u} \cdot \nabla c = div(c\boldsymbol{u})$. In general, all differential problems that model a conservation law of physics can be cast in conservation form l_{ij}.

For what concerns the FVM, once the differential operator is written in conservation form, take place the integration of the equation on control volumes upon the grid. The unknown parameters now are the approximation of u at each control volume. If we apply the divergence method, we have:

$$\int_{c_i} div\, \boldsymbol{F}(u)dx = \int_{\partial c_i} \boldsymbol{F}(u) \cdot \boldsymbol{n} d\gamma \approx \sum_j \boldsymbol{F}_{lij}\,(u_h) \cdot n_{ij}, \qquad (5.24)$$

where $\boldsymbol{F}_{lij}$is an approximation called numerical flux of the flux vector on the side l_{ij} of the control volume C_i. The numerical flux depends on the numerical solution u_h. By applying it to all control volumes of the grid we can transform equation (5.24) into a system of linear or non-linear equations. Therefore, the advantage of this method is that, instead of looking at the hole flow filed we limit our attention to small control volumes at a finite region. By that we achieve to obtain fluid flow equations in integral form. These integral forms of the governing equations can be manipulated to indirectly obtain partial differential equations. The equations obtained from the FVM, in either integral or partial differential form, are called the conservation of the governing equations. The equations obtained from the FVM moving with the fluid, in either integral or partial differential form, are called non-conservation form of the governing equations [54].

Chapter 6. Blood flow modeling simulations

The components of blood have been analyzed in the 2nd chapter so here we are going to refer to more technical aspects of blood. The first attempts to study the mechanics of blood flow were made by Young and Poiseuille in the 17th century. In order to develop a constitutive equation for blood there have been many attempts, but there is still lack of a theoretical reliable model of blood which would cover all regimes of physiological flow. Plasma by its self is a Newtonian fluid with dynamic viscosity of $1.2x10^{-3}$ Kg/m·s at 37°C [55]. However, due to the high cellular content of blood the whole blood behaves like non-Newtonian fluid. Although, the hole cardiovascular system is a network of vessels and chambers. Considering the dimensions, we are referring to and specially the diameter of the vessels ranging from 4-8μm, the deformations and the stresses of the blood are high. In terms of mechanics large arteries and veins are differentiated from other vessels by their size, as inertial effects are predominant over viscous effects. These characterizations are based basically on Reynolds number which we are going to study. The blood then can be characterized as highly non-Newtonian fluid [56]. At the CFD field and more specifically at the blood flow modeling aspects, assumptions are made because of the difficultness to simulate the fully realistic behavior of blood. In large arteries such as aorta and in the heart chambers the non-Newtonian effects are weak due to large dimensions. Then the blood is considered as a homogeneous fluid with Newtonian properties. The constant coefficients of blood (as we mentioned at Chapter 2) which we are going to use for our approach are the density $\rho=1060$ Kg/m^3 and the dynamic viscosity as $\mu=3.5\times10^{-3}$ Pa·s [56]. Another major assumption is that the blood is considered as an incompressible fluid. This assumption stems from the fact that the density is unaffected by the pressure. At this thesis we consider blood as a homogeneous, incompressible, viscus Newtonian fluid with constant density. For the purposes of the current study, the commercial

solver CFX, Release 15.7, Help System, ANSYS, Inc. was employed to model the blood flow in left atrium.

6.1 CFD approaches

We could say that the numerical simulations of blood flow can be classified into two major groups. The first one is a one-way approach which does not consider the interaction of fluid and structure. This approach simplifies the modeling as we don't need parameters for material properties of the wall for its deformation and we don't need a numerical formulation for the coupled system. On the other hand, the second approach is the modeling of the Fluid-Structure Interaction (FSI) between fluid and its surrounding solid structure. In this approach the first consideration is that the surrounding structure is responsible for the flow due to muscle contraction. Fluid exerts forces to the surrounding wall, which then in turn will deform and effect the fluid flow. Hence, the FSI simulations encounter a coupled problem where both structural and fluid solvers must interpolate each other to obtain data.

6.2 Newtonian and non-Newtonian fluids

All the fluids can de discretized to many subcategories which can be depicted in Figure 6.1. Even if they are all called fluids there can be major differences among their behavior under stress. All the fluids which obey to Newton's law where the dynamic viscosity is constant, they are called Newtonian fluids. If the dynamic viscosity is constant the shear stress has linear dependency on the velocity. This is applicable to the most common fluids. The other category of fluids stands for non-constant dynamic viscosity and their relationship between shear stress and velocity is gradient. These fluids are called non-Newtonian and there are several subcategories of them.

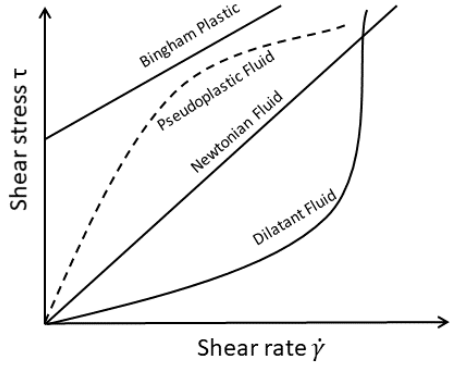

Figure 6.1: Newtonian and non-Newtonian fluids [57].

Above we explained the definition of Newtonian and non-Newtonian fluids, but the question that arise here now is if the blood flow is whether or not. At fluid mechanics Newtonian fluids are considered the simplest models that regard viscosity [58]. Natural fluids can't be represented perfectly and most of the times many common liquids and gases (water, air) are

assumed to be Newtonian for practical reasons and calculations. The blood's viscosity coefficient examined and found to be five times greater than water's, for a relatively large diameter [59].

6.3 Laminar flow and turbulent flows

The flow condition can be categorized at two major categories, laminar flows and turbulent flows. Laminar flows are characterized by highly ordered fluid motion by smooth layers of fluid. Laminar model defines a flow where all the particles of the fluid are moving as a straight line. We can also note it as, all the particles of the fluid are moving in the same rate. The word laminar comes from the movement of adjacent fluid particles together in "laminates" [58]. Fluids with high viscosity such as oil, at low velocities are typically laminar. Turbulent flow is highly disordered fluid motion that typically occurs at high velocities and it is characterized by velocity fluctuations. This type of flow is characterized of irregular movement of particles something like a state of "chaos". When a critical velocity is overextended the fluid becomes turbulent. The alternating flow between laminar and turbulent is called transitional.

We assumed flow is transitional, i.e. the flow is at an intermediate condition between laminar and turbulent. We calculated an average Reynolds number at the pulmonary veins (inlet) is Re=940.37 (average velocity $\boldsymbol{u}$ =0.27 m/s, diameter **d**=0.0115 m) and an average Reynolds at mitral valve (outlet) is Re=5542.28 (average velocity $\boldsymbol{u}$ =0.61 m/s, diameter **d**=0.03 m). Based on this Reynolds number we assumed the flow conditions to be transitional. For that purposes we used a turbulent model "the k-epsilon (k-ε)" to solve the motion of the blood flow into the left atrium. The k-epsilon model is a protrusive turbulence model and it has been proven to be stable and robust numerically. It uses a scalable wall functions to enable solutions near fine wall grids. The k denotes the kinetic energy that is defined at the model, and it expresses the variance of fluctuations in the velocities and ε is the turbulence eddy. When the k-ε model is used it introduces two new variables to the basic system and the continuity equation is expressed as:

$$\frac{\partial \rho}{\partial t} + \frac{\partial}{\partial x_j}\left(\rho U_j\right) = 0. \tag{6.1}$$

Afterwards the momentum equation is

$$\frac{\partial \rho U_i}{\partial t} + \frac{\partial}{\partial x_j}\left(\rho U_i \mathrm{U_j}\right) = -\frac{\partial \mathrm{p'}}{\partial \mathrm{x_i}} + \frac{\partial}{\partial \mathrm{x_j}}\left[\mu_{\mathrm{eff}}\left(\frac{\partial \mathrm{U_i}}{\partial \mathrm{x_j}} + \frac{\partial \mathrm{U_j}}{\partial \mathrm{x_i}}\right)\right] + \mathrm{S_M}, \tag{6.2}$$

Where $\mathrm{S_M}$ denotes the sum of the forces, the μ_{eff} denotes the effective viscosity for turbulence and $\mathrm{p'}$ expresses the modified pressure.

6.4 Wall shear stress (WSS)

As Wall Shear Stress (WSS) for Newtonian fluid is defined as the tangential forces from friction on the wall caused by the moving fluid and is given from the equation:

$$\tau_w = \mu \frac{\partial u}{\partial y}|_{y=0}, \tag{6.3}$$

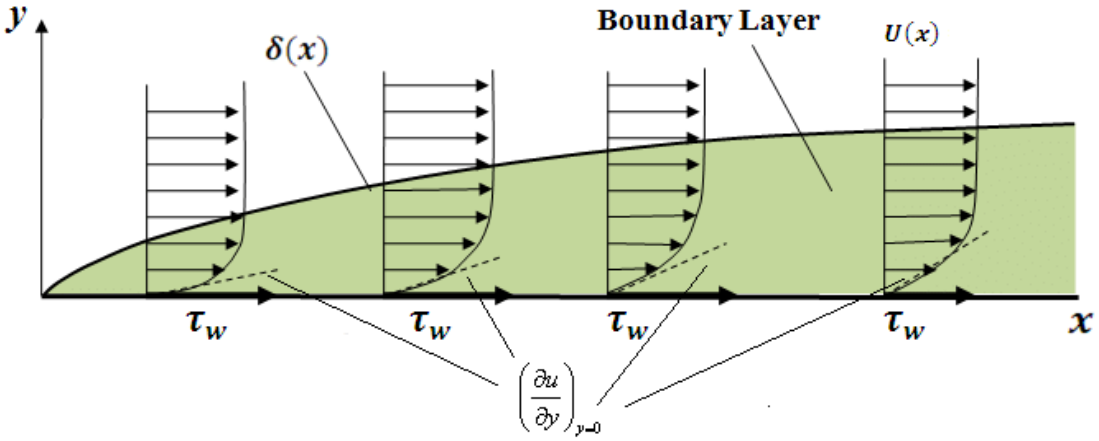

Figure 6.2: Wall shear stress [58].

where μ is the dynamic viscosity of fluid, u is the fluid velocity along the boundary, h height above boundary. A moving fluid will incur a shear stress at that boundary. As we will mention below the no-slip condition impose that the speed of the fluid at the ending layer of the boundary is zero but at specific height is equal with the fluid's speed. That region between these two points is called "The boundary layer". In a typical vessel when the endothelial cells exposed to shear stress alterations due to blood flow's periodic nature and the magnitudes of the Wall Shear Stress (WSS). In case of a steady laminar flow the WSS (are at normal ranges) enhance the release of factors from the endothelial cells that suspend smooth muscle proliferation, coagulation, migration and general the endothelial cell survival. On the other hand, WSS values outside of the normal range can potentially lead to vascular pathologies.

Turbulent flow which results at higher WSS values (arising at stenotic regions, high curvatures and complex geometries) may damage the endothelial cells. These damaged cells afterwards may be the major factor for plague formations and thereafter generate thrombosis. The human body by itself, try to cape with increases of WSS, attempting to maintain the normal function by local tissue remodeling such as thickening of the intimal layer, diameter adaption.

6.4.1 WSS impact on blood flow

Cardiac chambers as blood vessels too, are under constant mechanical loading, due to blood pressure. The blood flowing exerts a pulsatile force on the surrounding wall, and its radial force is defined as the blood pressure which can lead to geometrical changes (e.g diameter).

Moreover, the tangential force defined as wall shear stress (WSS) produces a frictional force that can immediately effect the endothelial functionality [60]. There are several studies in the literature that associate WSS with a variety of pathological diseases like ischemic stroke, atherosclerosis [44–46]. The measurement of the WSS could potentially provide deeper insights of the cardiovascular pathophysiology and provide clinicians with useful tools for clinical assessments. Although, unfortunately the WSS measurement is not a straightforward process.

Primal blood velocity data can be provided through Doppler ultrasound measurements, which are going to be used by mathematical models to calculate WSS or wall shear rate (WSR). The common model used in clinical practice is the Hagen-Poiseuille [47, 48], but it has several limits due to its idealistic assumption of parabolic velocity profile. The Womersley model [66] is one of the most accurate and used models, however, is limited to straight rigid tubes and laminar flows. In reality though, the vessels and the cardiac chambers are formed by complex, irregular geometries with complex flows.

6.4.2 Methodology for the LAA

In this study we focused to investigate the velocities and the WSS at the LAA. For that purposes we developed an approach to extract values alongside the LAA cavity. Our interest is to examine the velocities and WSS distributions at the LAA surface and not the gradients. Starting from the orifice, 3 random 3D x, y, z points are selected as baseline to generate a surface enclosed by the LAA cavity Figure 6.3Figure *6.4*. Afterwards, we generated a line at the borders of that surface to examine the velocities and the WSS values upon this line. A fix displacement step is used x=0.005m to generate the rest of the cross-sections, until the LAA tip area is reached. The total number (see Table 2) of the generated cross-sections depends on the length of the LAA surface. Finally, all the velocities and WSS results, regarding the LAA, are plotted upon these lines and they are demonstrated. For all the above purposes an in-house Matlab code (Mathworks) was developed during the research of this thesis.

Table 2. Numbers of total cross-sections.

Patient ID	Total number of cross-sections
1	19
2	31
3	20
4	23
5	15
6	24
7	10

8	15
9	19
10	15
11	33
12	32
13	27

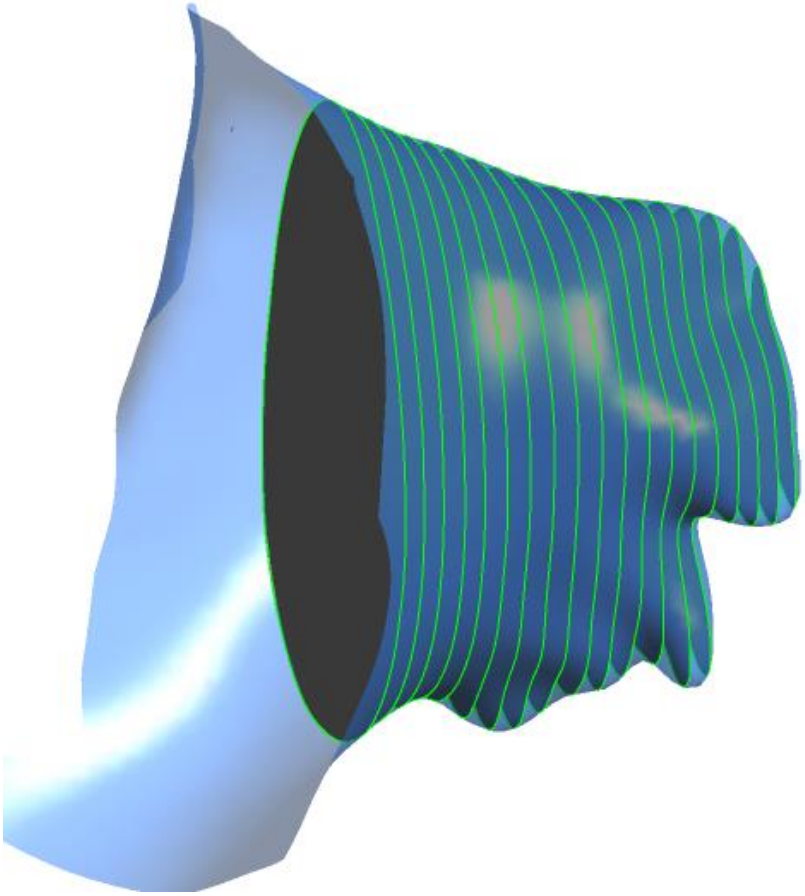

Figure 6.3. LAA generated polylines alongside its surface

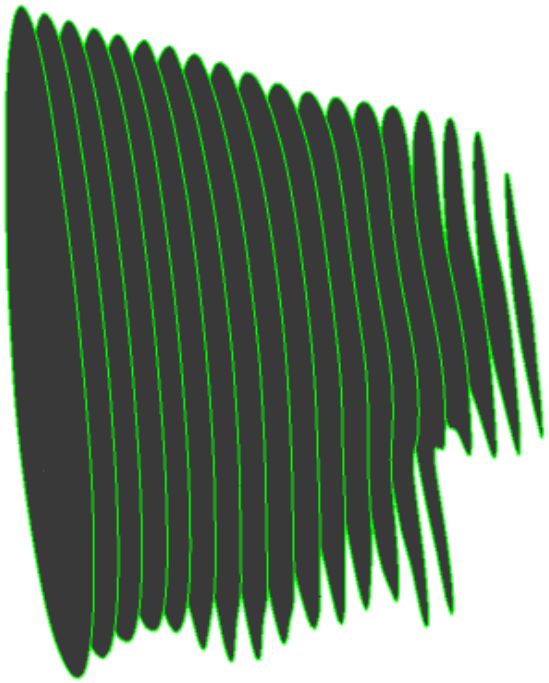

Figure 6.4. Surfaces for polylines generated inside the LAA cavity.

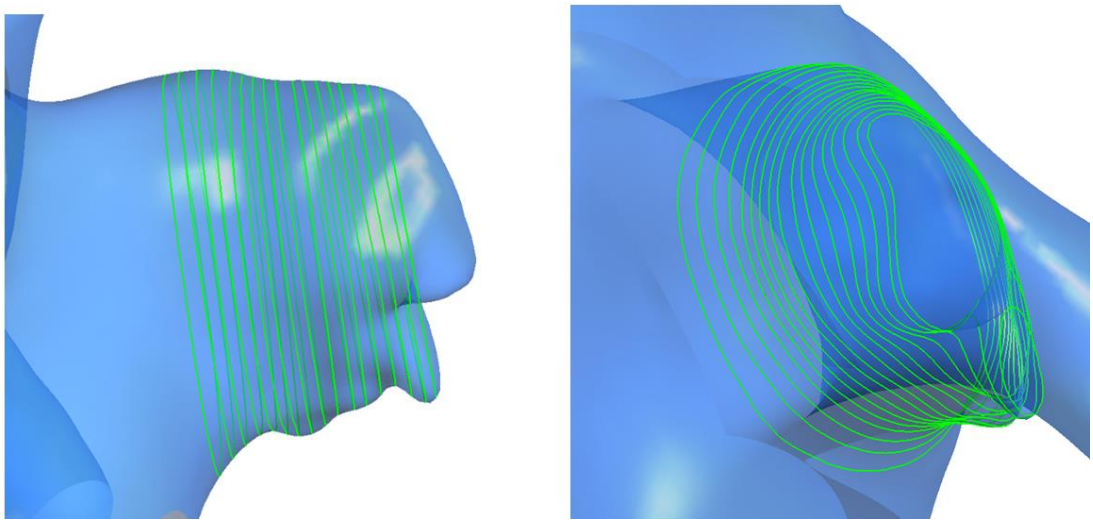

Figure 6.5. Generated cross-sections alongside the surface of the appendage.

6.5 Methodology for blood flow modeling

The major field studying the fluids is called rheology, so we can refer at the behavior of fluid as rheologic behavior and specially for blood hemorheology (haemorheology from the Greek word ‘αἷμα and rheology from Greek ῥέω rhéō, "flow"). The rheologic behavior of the fluids depends on the in-between relationship of stress tensor and the strain rate tensor. There are two major models that can be used to describe the rheology: Newton’s and Carreau’s. The Newton’s law expresses a linear relationship between stress and strain which is noted as:

$$\tau_{ij} = 2\mu d_{ij}, \tag{6.4}$$

where μ is the blood dynamic viscosity, ρ is the blood pressure and d_{ij} is the strain tensor calculated as:

$$d_{ij} = \frac{1}{2}(\nabla v + \nabla v^T), \tag{6.5}$$

The Carreau's law afterwards, is noted as:

$$\tau_{ij} = 2\mu(\dot{\gamma})d_{ij}, \tag{6.6}$$

where γ represents the shear expressed as:

$$\dot{\gamma} = \sqrt{2d_{ij}d_{ij}}, \tag{6.7}$$

We model blood as incompressible, homogenous with constant density Newtonian fluid. The thermal and gravity effects are neglected. Under this assumption the CFD problem expressed by the conservation of mass and momentum as we mentioned at Chapter 5. The walls of the atrium are modeled as rigid walls. Under these two assumptions the fluid dynamics problem is expressed by the conservation of mass and momentum (Chapter 5).

Finite Volume (FV) method is used, to discretize the Navier-Stokes equations. Modelling the blood flow is carried out using the Navier-Stokes and the continuity equations as we mentioned above.

6.5.1 Boundary conditions

Emphasis was placed at the 3D geometry to acquire as much accuracy is possible. Hence, to define appropriately the fluid dynamic problem we must specify the boundary conditions. Our model has been parameterized with clinical data extracted from real patients. Velocity and pressure values are used to extract and examine velocities, WSS and pressures at the LA. First, steady state simulations were executed to obtain initial conditions and use them afterwards as inputs for the transient simulations. Velocity TEE values used to reproduce inflow conditions. The first velocity value used at the steady simulations as input at t_0 was 0.03 m/s, a value close to the starting point of the transient velocity profile. We defined velocities at the inlets (Figure 6.6) and a constant pressure value as outlet equal to 5 mmHg. The transient simulations afterwards take place over 3 completed cardiac cycles with each of them to be around 0.8 s (total time around 3.6 s). Its cycle was divided to specific timesteps based on the patient's BPM. To achieve a sufficient computational cost each cycle would have around 30 sub-timesteps and 90 totals, obtained by the following calculations:

$$\frac{\text{Minute}}{\text{BPM}} = a, \tag{6.8}$$

$$\frac{a}{30} = \text{timestep}. \tag{6.9}$$

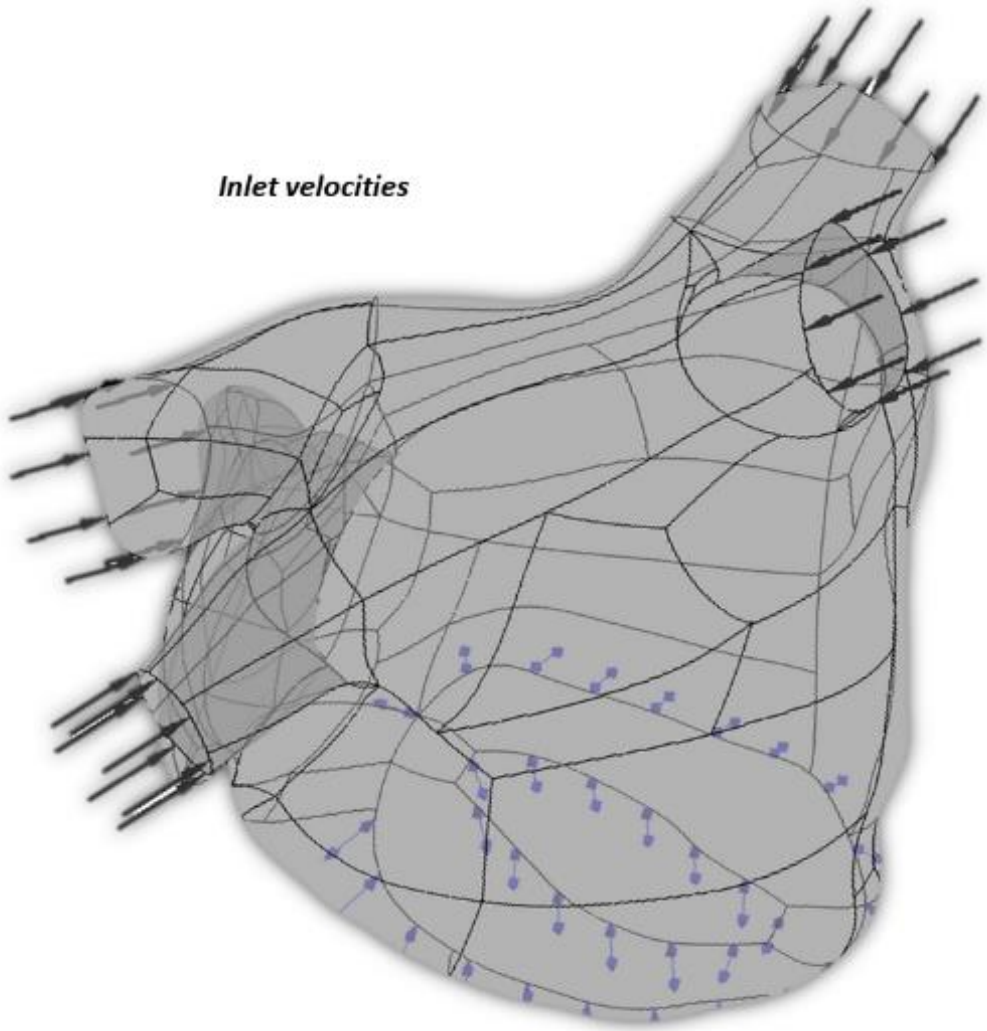

Figure 6.6. Inlets at the four pulmonary veins of the left atrium.

6.5.2 TEE digitization and velocity profiles

In order to obtain blood velocity data, we used TEE images. The TEE demonstrates waveforms at specific areas. For our purposes it was the best approach to extract real clinical data from patients. In order to obtain a velocity profile with respect of time, we digitized the TEE waveform and we extracted specific timepoints. At each cycle the three atrial waveforms were included (S, D, A) and at the end, the results are demonstrated upon these peak values. We used a Matlab code developed by [67], to digitize the TEE graphs and obtain specific points of a completed cardiac cycle on the waveform. Afterwards, we used this wave-profile to obtain velocity values with the respect of the time. Figure 6.7 we can observe a typical TEE image, where there are denoted the three waves, as the starting point of our velocity profile.

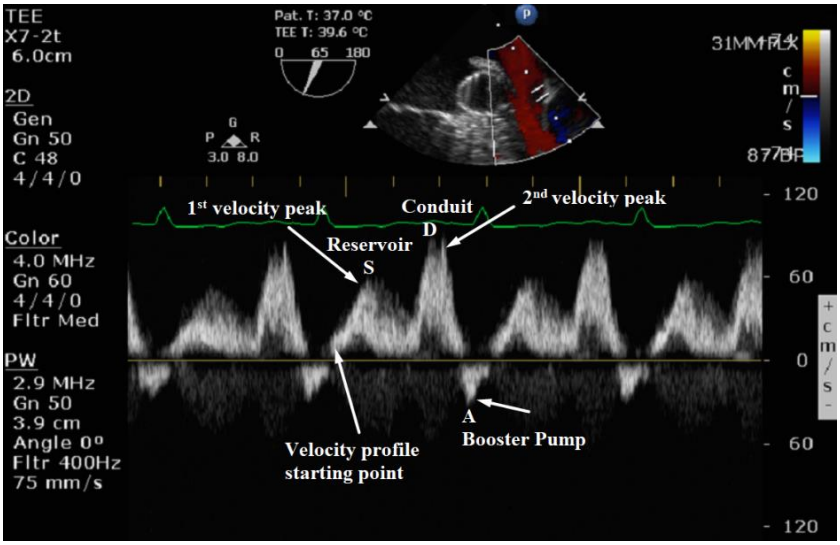

Figure 6.7: Pulmonary veins waves and peak velocities.

The extracted velocity profiles used as inlets boundary conditions at the pulmonary veins. From the time that our simulations are transient, we considered the usage of a full profile, instead of one specific value, to simulate a more realistic condition. In Figure 6.8 are presented all the five velocity profiles that we used. The normal TEE waveform represents the normal velocity profile known as sinus rhythm and the others represent the abnormal conditions. As the clinical studies have examined [61, 62], a normal blood flow condition is denoted at the waveform with its first wave to be bigger than the second. When the S wave is bigger than the D wave, we are having a normal blood flow condition. On the other hand, an abnormal condition is denoted at the waveform when the second wave is bigger than the first one (S<D). Our digitized velocity profiles follow the above theory. The normal profile has S>D and all the others have D<S.

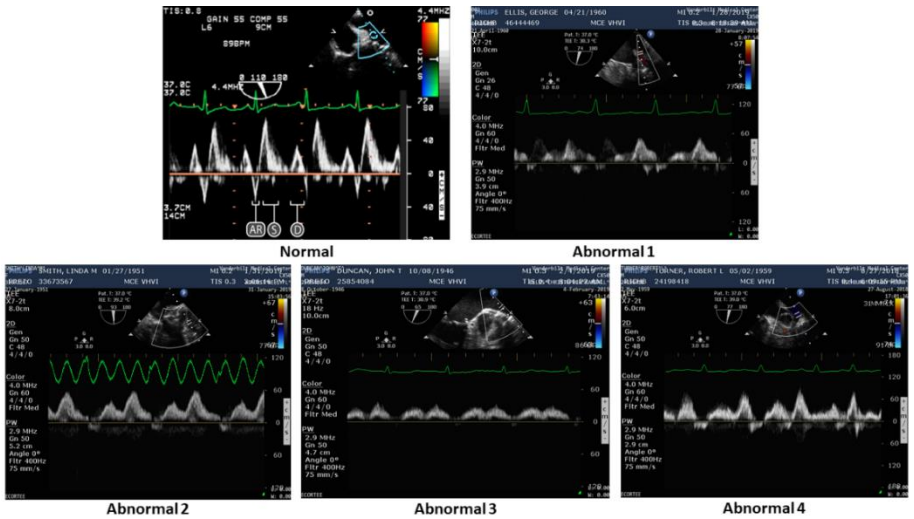

Figure 6.8. TEE velocity profiles used to obtain data.

Figure 6.9 depicts plotted together all the velocity profiles we used at the blood flow simulations. The normal velocity profile revealed the highest value at the S peak wave and the

Abnormal 4 profile revealed the highest velocity value at the D peak wave. The classification of the velocity profiles starting from the higher to the lower is: Abnormal 4 > Abnormal 1 > Normal > Abnormal 2 >Abnormal 3 based on the mean values calculated from the velocity profiles (Abnormal 4 = 0.25 m/s, abnormal 1 = 0.2 m/s, normal = 0.18 m/s, abnormal 2 = 0.13 m/s, abnormal 3 = 0.1).

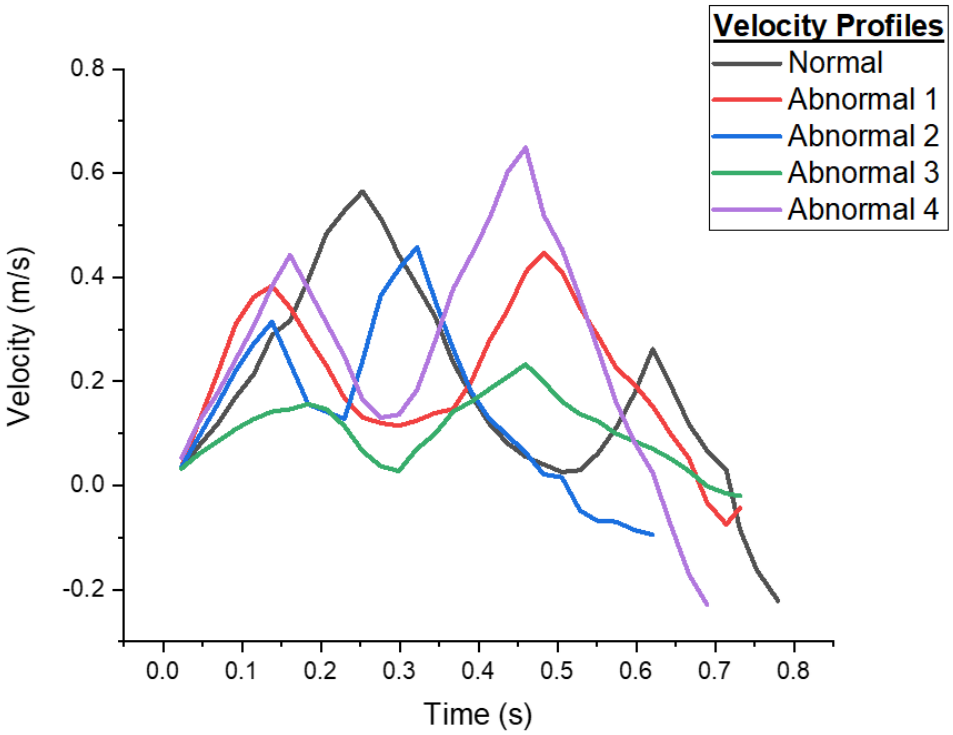

Figure 6.9. Digitized TEE and regenerated waveforms to obtain velocity profiles.

We transformed the pulmonary veins phases (waves), so S, D, Ar waves transformed to Conduit, Reservoir and Booster Pump will represent the atria's flow phases at the cardiac cycle.

6.5.3 No-slip condition

Blood flow is influenced by the pressure of solid boundaries. No fluid can flow within a solid boundary, so that velocity normal to the surface is zero. Viscous forces consist the fluid to "stick" upon the wall, so the tangential fluid's velocities are equal to the velocities of the wall, that is called no-slip condition. Because of that, the atrial walls assumed to be rigid, and a no-slip condition was imposed at the LA and LAA surfaces. The boundary velocity is a tangential component $\mathbf{U}_T$ and the boundary condition is called no-slip condition at fluid dynamics and normally invokes to every interface for fluid-structure:

$$u_T = \mathbf{U}_T, \tag{6.10}$$

If a solid surface is not moving, then $\mathbf{U}_T$=0 because the surface is not moving, and the no-slip condition becomes $\mathbf{u}_T$. The no-penetration condition stems here as non-bulk fluid cannot

penetrate an impermeable boundary. Hence, the normal component of fluid velocity $\mathbf{u_N}$ must match the boundary velocity $\mathbf{U_N}$ as:

$$u_N = \mathbf{U_N}, \tag{6.11}$$

The above boundary condition is called no-penetration condition and its applicable to any solid in contact with a fluid [70].

6.5.4 Reynolds number

After a lot of experiments in the 1880s, Osborne Reynolds discovered that the flow regime depends mainly on the ratio of inertial and viscous forces in the liquid. This ratio is known as Reynolds Number (Re) [58].

$$\mathrm{Re} = \frac{\text{Inertial Forces}}{\text{Viscous Forces}} = \frac{\rho U D}{\mu}, \tag{6.12}$$

The Reynolds number is a dimensionless quantity that depends on the diameter D of the geometry, the mean blood velocity U, the density ρ and the viscosity μ of the blood. Particularly, in the aorta the Re≈4000 and 400 in coronary arteries. Thus, the range of blood's Re number is relevant varying from 50-4000. Although the pulsatile nature of blood flow does not allow development of full transition to turbulence. It is debatable whether the condition of the flow. In Table 3 we demonstrate some typical values of Reynolds number at main chambers and vessels.

Table 3: Reynolds number.

Nature	**Re number**
Bacteria	10^{-6}
Human	10^{6}
Blue wale	10^{8}
Automobile airplane	10^{7}
Aorta	2500
Typical vessel	100

At large Re numbers the inertial forces which are proportional to the fluid density and the square of the fluid velocity, are large relative to the viscous forces and thus the viscous forces cannot prevent the random and rapid fluctuations of the fluid. At small or moderate Re however, the viscous forces are large enough to suppress these fluctuations and to keep the fluid in line. Thus, the flow in the first case is characterized as turbulent and laminar in the second. The critical point at which the flow becomes turbulent is called the critical Reynolds number, Re_{cr}. These values vary among different geometries and flow conditions. All the above certainly describe the values of Re but this is not the case in practice. It turns out that the transition from

laminar to turbulent flow also depends on the degree of disturbance of the flow by surface roughness, pipe vibrations and fluctuations in the flow [58]. It has been established under the most practical conditions that the flow is:

- **Re** ≤ 2300 **Laminar flow**
- $2300 \leq$ **Re** ≤ 4000 **Transitional flow**
- **Re** ≥ 4000 **Turbulent flow**

First, cardio modeling is totally different from vascular modeling because of different dimensions. The diameter for example between a vessel and a large artery as the aorta, is totally different as we can observe in Table 3. It is controversial among studies the type of the flow at cardiovascular modeling. At most of the studies where vessels or arteries are simulated because of their diameter and their velocities the flow is considered as laminar. At some special cases where the geometry has curvatures and bifurcations a turbulence flow is occurred. From the above mentioned, we considered that the flow is at transitional condition. Specially at LA, where even the angle of PVs has critical role for the direction and the speed of flow. This consists that every different angle would provide different amount of flow rate inside the appendage. Furthermore, this indicates the significance of the morphology and the shape of the whole LA and specially the LAA.

Hence the above, modeling the large chambers of the cardiovascular system is a new field, as the 80% of the previous studies have focused to model mostly arteries.

6.6 Post processing

Once the CFD procedures and computations have been carried out, we can exploit the solution modules for direct visualization by means of vectors, contours etc. Apart from straight-forwards visualizations, post processing techniques are needed for effective demonstrations. At the next section we are going to demonstrate the results from our blood flow simulations.

6.7 Blood flow modeling assumptions

The major assumption of this thesis is that the walls are rigid with no movement. That lies far away from a realistic beating heart since the heart beating is produced from moving walls (muscles), but the results indicated that our approach can provide results with good accuracy to examine the hemodynamics in the LA and LAA. Also, the wall thickness is constant everywhere, but originally the posterior wall is quite thicker than the anterior [71]. Another assumption is that the MV doesn't move (open/close) as the normal valve does. We consider it as always open, but we specified it as an opening outlet which allows forward and backward flow, as the physiology of the atrium has a specific phase called "atrial reverse flow".

Chapter 7. Results

At the present thesis, 13 patients were studied. All the results are produced during the systolic and diastolic (S, D) phase of the left atrium. Here we are going to demonstrate the results for the atrium and the left atrial appendage. We focused our post processing to investigate mainly the velocities and the WSS. The produced results would be compared among all the patients at different timepoints. Specifically, regarding the WSS values at the LA, we have separated the cavity at two major views, the posterior and the anterior. Regarding the LAA we are demonstrating the anatomical morphology of each patient and we tried to analyze its impact on blood velocities and WSS. In Figure 7.2 the percentages of the anatomical morphologies of the appendages from 13 patients are depicted. As we can observe and as the literature confirms [6, 16, 67], the most common morphology among the studied cohort was the chicken wing. Obviously, the patient's cohort is small to extract strong statistics about the morphologies.

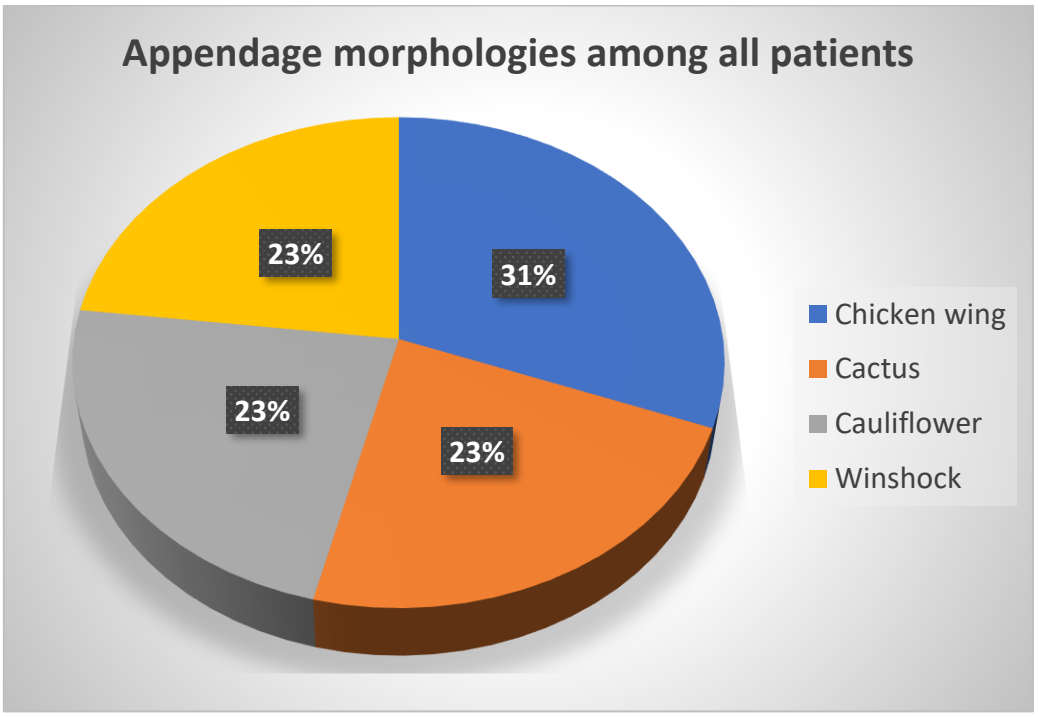

Figure 7.1. Statistics of LAA morphology among 13 patients.

7.1 Velocity

One major critical factor that is affected by the geometrical morphology is the blood's velocity. Our study focused strongly to examine the impact of different velocity profiles, as also the resulting velocities from these profiles. We used five different velocity profiles, one that represents a normal blood flow condition and four that signify abnormal conditions.

7.1.1 LA

Concerning the LA cavity, we are demonstrating the velocities using streamline visualizations which start from the inlets and they finish at the mitral valve. This kind of visualization express the path and the direction that the blood flow moves on. In order to examine the impact of the different velocity profiles, all the velocity values at the LA cavity are demonstrated with raw extracted velocity data from the blood flow simulations. We can observe at the right side of the anterior view that there are in some cases a few curved streamlines. These streamlines denote the flow that has passed inside the appendage cavity. Instead, in some cases the curved lines at the LAA area are absent, indicating that the velocity values are low and can push a normal blood volume inside the appendage, or that there is insufficient blood flow inside the appendage cavity. When the next cardiac cycle starts, some particles have been motionless inside the appendage and try to leave the cavity. When this situation is generated simultaneously it leads to blood stagnation. Furthermore, we can observe that at the main atrial cavity of all the patients, the flow and the velocities are normal, instead of the PVs area where the highest velocity values are shown up.

Figure 7.2 depicts the streamlines of the velocities, where a colormap on them indicates the values at the specific area, are presented. The main atrial cavity revealed the lowest velocities (especially patient 1), as the highest velocities are mainly at the area of the pulmonary veins and the mitral valve. Abnormal 4 velocity profile indicated the most turbulent streamlines mostly at the roof area between the pulmonary veins and near at the prolongation of the LAA cavity. The normal velocity profile indicated generally normal flows through the whole atrial cavity and at patients 3, 4 a velocity increase at the pulmonary veins. The Abnormal 2 velocity profile at patients 1, 4 and the Abnormal 3 velocity profile at patients 2, 4 indicated absent streamlines at the LAA cavity, indicating that there is limited inflow at the appendage. The results for the abnormal 3 velocity profile indicated the lowest velocities for all the five patients and that is confirmed due to its original low velocity data.

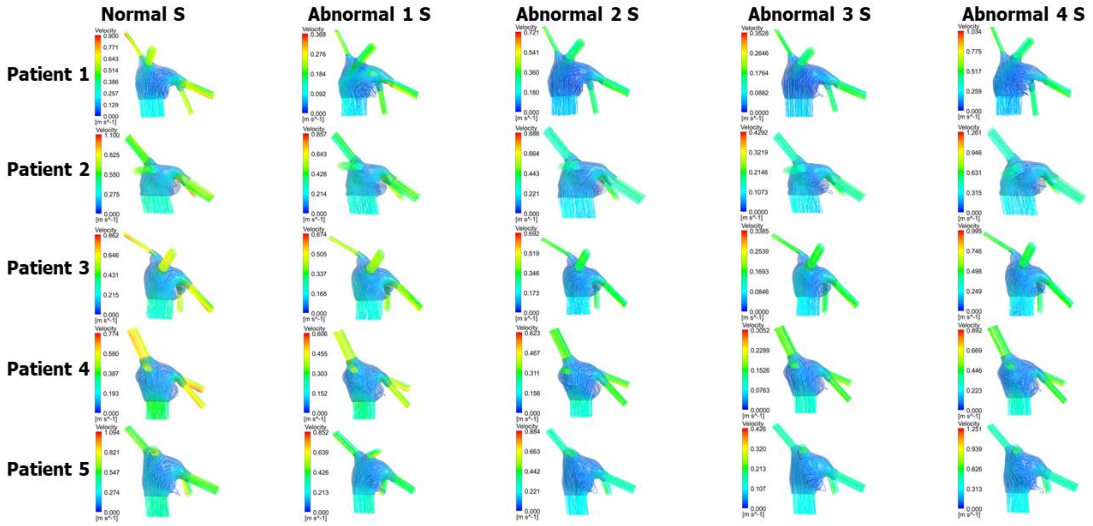

Figure 7.2. LA velocity streamlines visualization for patients 1-5.

Figure 7.3 demonstrates the streamlines for patients 6-10. The flow inside the appendage is completely absent at patient 6 and we are going to examine it at a section below. The normal velocity profile indicated the highest values at the pulmonary veins to all the patients. Afterwards, the flow inside the atrial cavity is becoming normal. Patient 10 indicated the most turbulent flow at all the velocity profiles, due to its strange shrinked shape of the atrial cavity.

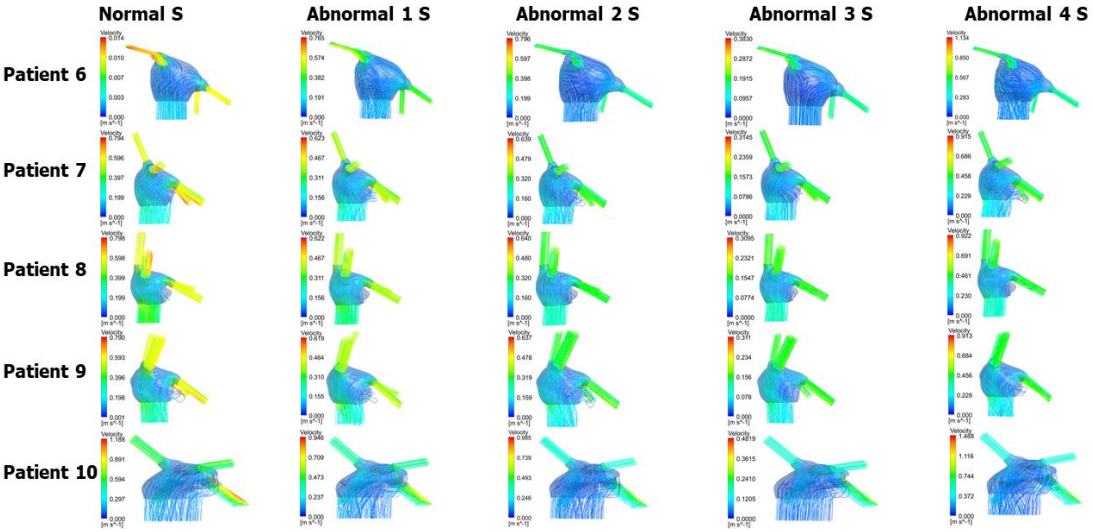

Figure 7.3. LA velocity streamlines visualization for patients 6-10.

Next, in Figure 7.4 the last 3 patients are demonstrated. These 3 patients revealed the highest velocities as it can be observed from the colored streamlines. Patient 13 indicated the highest velocity values at mitral valve area. Moreover, the curved streamlines that inflow at the appendage are absent at patient 6, 13 and especially at the abnormal 2, 3 and 4 velocity profiles are completely elusive. Although, we don't observe very high velocities at the pulmonary veins, something that was depicted on the previous patients.

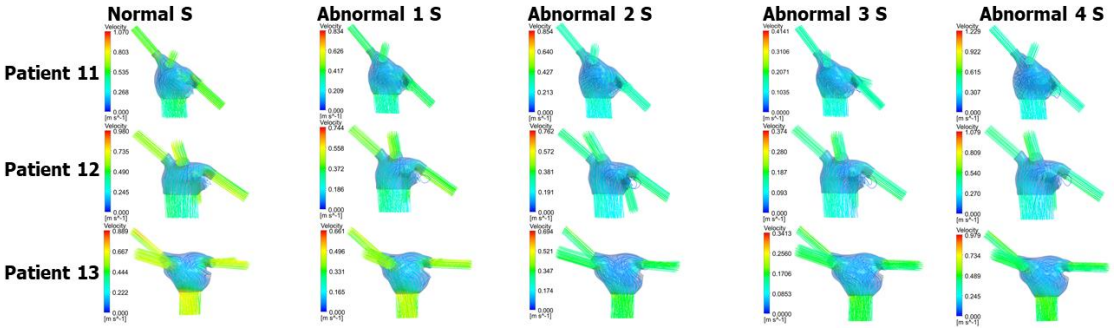

Figure 7.4. LA velocity streamlines visualization for patients 10-13.

Above we demonstrated and examined the atrial cavities of 13 patients. The results from blood flow simulations for five different velocity profiles are visualized with the usage of the streamlines. The velocities at the main atrial cavity demonstrated normal blood flows and that's because of the large length of the LA, where the flow resistance is normal. Although, some small turbulent areas were appeared mostly at the LA roof and near the appendage cavity, there were the diameter and the length of the cavity narrows and the flow resistance becomes higher. Moreover, the pulmonary veins indicated the highest velocity values, due to their narrow radius (an average diameter is $\boldsymbol{d}=0.0115\ m$). Even though to get more detailed results about the impact factors of the blood flow, the blood must be simulated with particles because is not a simple fluid and examine each critical clinical and geometrical factor that effects it. Besides, at this study our approach can provide primal data with decent outcomes about the blood flow inside the LA.

All the demonstrated velocity streamline results, regarding the D phase can be found at the part A of the Appendix.

7.1.2 LAA

Regarding the appendage as we mentioned at Chapter 6, the results were calculated upon the cross-sections alongside the LAA surface. Figure 7.5 demonstrates the mean values from all the resulting velocities at the appendage of all the patients, separately for each phase wave (S, D). All the values have been calculated upon the generated cross-sections on the LAA surface and they are depicted in box plots.

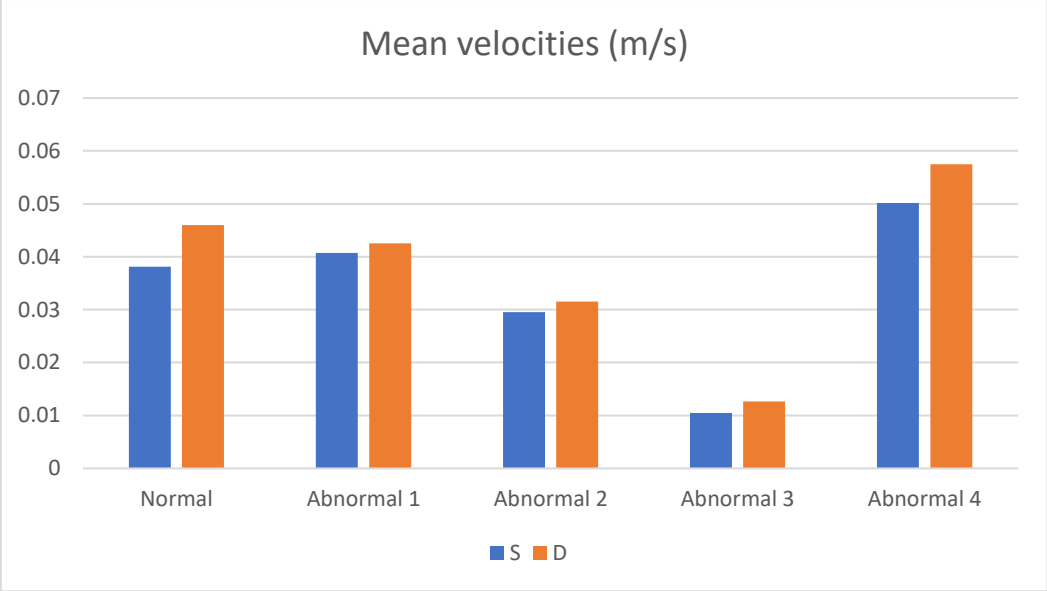

Figure 7.5. Mean LAA velocities extracted from the generated cross-sections.

In

Figure *7.6* we can observe a classification we performed, based on the velocities and the morphologies. The chicken wing morphology indicated the highest velocities, the cauliflower afterwards and at the end the windsock and the cactus the lowest. Moreover, that's a primal observation about the morphologies and their impact on the blood flow.

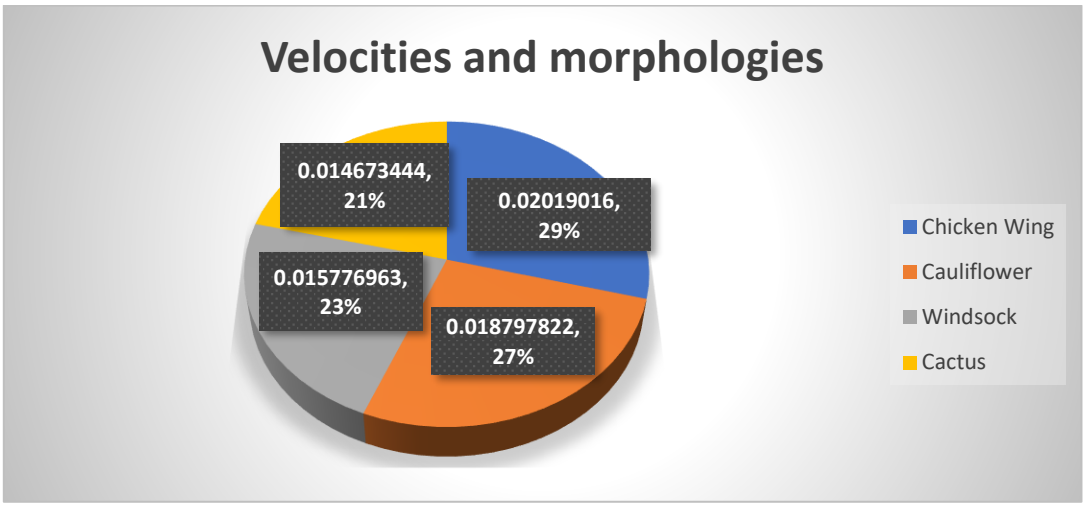

Figure 7.6. LAA morphologies classification based on velocity findings.

The results indicated a reducing velocity through the LAA, starting from the orifice to the tip, as it is visualized at the graphs in Figure 7.7. As the generated cross-sections moving through the tip area of the LAA, the velocity tends to have a descending progression. As we can observe the Abnormal 3 velocity profile has the lowest values, something that we verified at our results. In Figure 7.7 the green line represents the Abnormal 3 profile indicated the lowest velocities at the patient's LAA velocity results. On the other hand, the Abnormal 4 profile which has the

highest velocities wasn't always demonstrated the highest values at the LAA. Patient 11 with the chicken wing morphology indicated the highest velocity values. Alternatively, the patient 4 with the cauliflower morphology had the lowest velocities comparing with the rest patients. Moreover, the patients 2, 3, 4, 5, 8, 9, 12 maintained quite normal velocities until the middle area of the LAA, and afterwards they had a dropdown. On the other hand, patients 1, 6, 7, 10, 11, 13 had an immediate velocity drop down after the first 3-5 cross-sections, meaning at the end of the orifice and far along. That situation promotes these morphologies of the appendages more prone to blood stagnation.

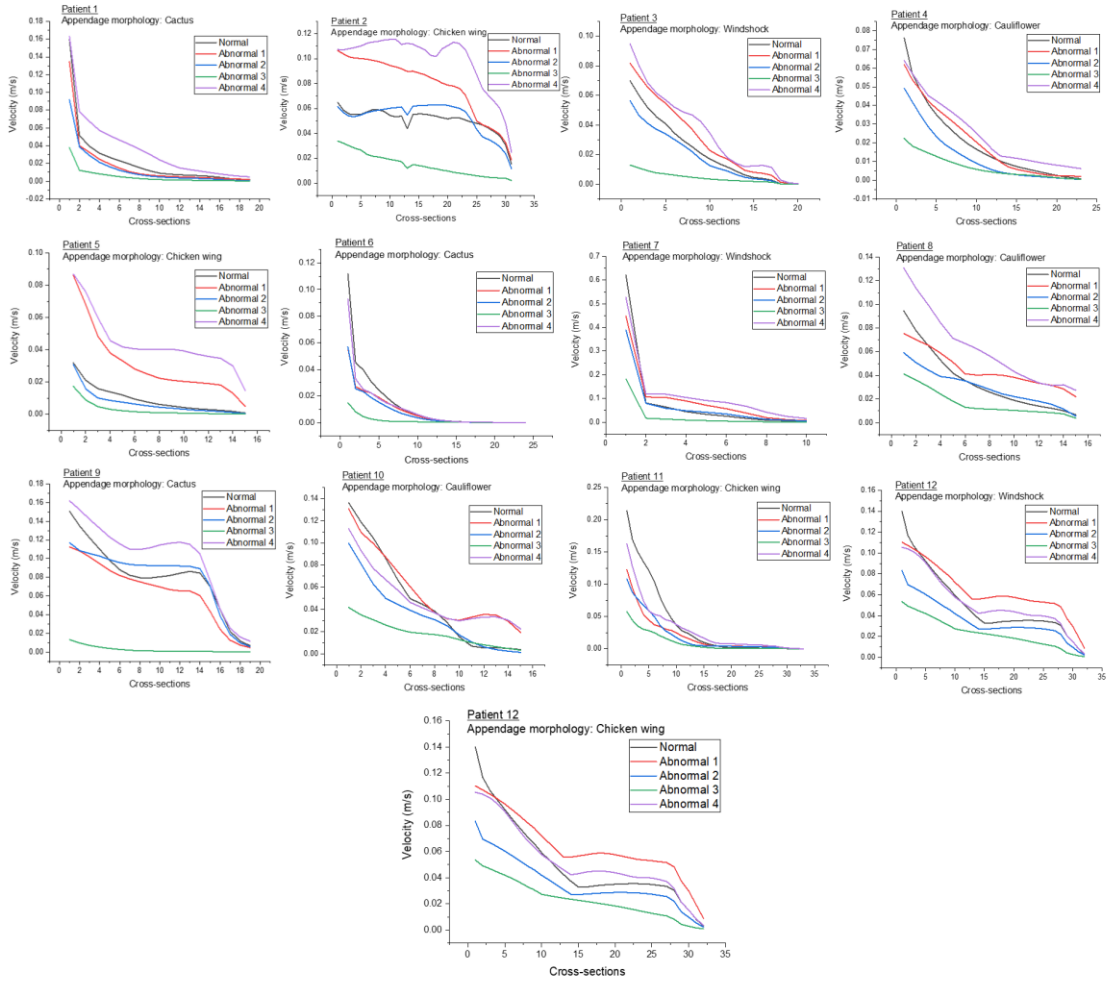

Figure 7.7. Velocity results for the LAA cavity, produced from the generated cross-sections.

Regarding the LAA, the results indicated a reducing velocity alongside its length, starting from the orifice to the tip. The examined parameters varied among different appendage morphologies, as the anatomical shape of the LAA has significant impact on the blood flow. As the results indicated, the morphology has very higher impact than the velocity profile at the flow conditions inside the appendage. In Figure 7.8 the patient-specific mean values of the velocity findings, calculated upon the cross-sections of all the appendages are depicted. The

values are demonstrated sorted in terms of largest to smallest velocities. A paradox can be observed as the cactus morphology is at the same time at the first and the last place. The only reason that patient's 9 cactus morphology has the first place, it's because this appendage has the largest diameter at the orifice d = 2.52 cm, while the other cactus morphology has d = 1.63 cm.

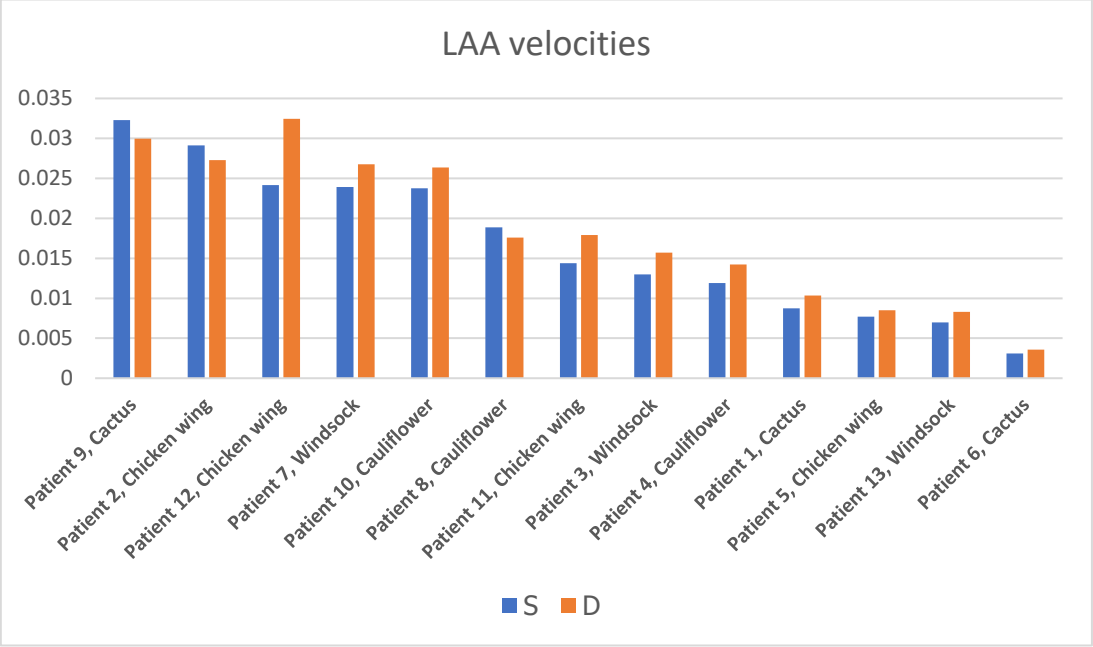

Figure 7.8. Calculated LAA velocities from all the appendages, sorted by the largest to the smallest value. The blue boxplot represents the S phase and the orange box plot represents the D phase.

All the velocity results (graphs) during the D phase can be found at the part A of the Appendix.

7.2 Wall shear stress (WSS)

At this section we are going to demonstrate the WSS results of the LA and LAA, as to examine the impact of the different implemented velocity profiles. The geometry of each patient will be demonstrated with colorful contour visualizations at each implemented velocity profile.

7.2.1 LA

The WSS values that we examined for the LA cavity were divided and demonstrated at the atrium's two major views, the anterior and the posterior. In order to describe an inter-observation among all the patients, the mean WSS values were calculated for each LA's side (anterior, posterior) at both phases. Afterwards a mean value for all the patients was used to visualize with colormap contours and the same scale, the WSS at each case. Table 4 demonstrates the WSS resulting values from all the velocity profiles that were used to visualize the WSS, independently for each patient.

Table 4. Mean LA WSS values.

Velocity profile	Anterior	Posterior
Normal	0.48	0.52
	0.29	0.28
Abnormal 1	0.33	0.33
	0.36	0.38
Abnormal 2	0.24	0.25
	0.35	0.37
Abnormal 3	0.07	0.07
	0.11	0.11
Abnormal 4	0.46	0.47
	0.67	0.71

Next, we are demonstrating the resulting WSS values at the LA area. All the WSS values are calculated only at the LA areas, as the appendage has been cut off from the rest geometry for these calculations' purposes. As we mentioned above, we examined the LAA separately for its two sides (posterior, anterior) and we compared them. Studies [16, 17] have indicated that the posterior has rough surface and it is more thick than the anterior wall. Studies have assessed that in practice [39] and they validated that the posterior side reveals higher WSS values. That occurs because of the characteristics of its anatomical morphology (thickness, curves, puddles) and its abnormal surface. Mostly, the results indicated higher WSS values at the posterior region, almost at all the different conditions of the velocity profiles.

In Figure 7.9 the WSS values at the anterior side of the LA during the S phase, are depicted for patients 1-5. Patient 2 indicated the higher WSS values as the contours at its surface are mostly red colored. On the other hand, patient 1 indicated the lowest values.

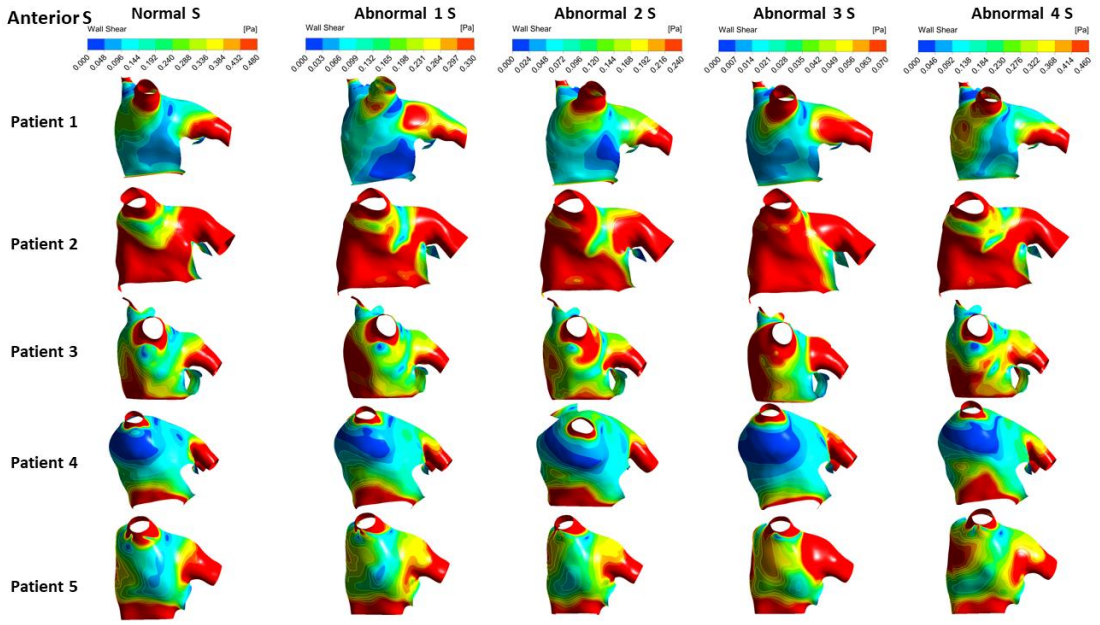

Figure 7.9. WSS values at the anterior side of the LA for patients 1-5.

Figure 7.10 presents the anterior WSS values for patients 6-10 during the S phase. Patient 8 here, same as previously with patient 2, indicated the highest WSS values as we can observe the colored contours on its surface. Patient 6 revealed the lowest values and specially at the normal velocity profile. Although, patient 6 indicated the lowest WSS values and particularly at the normal velocity profile. Patient 6 though, is a special occasion which we are going discuss at next section.

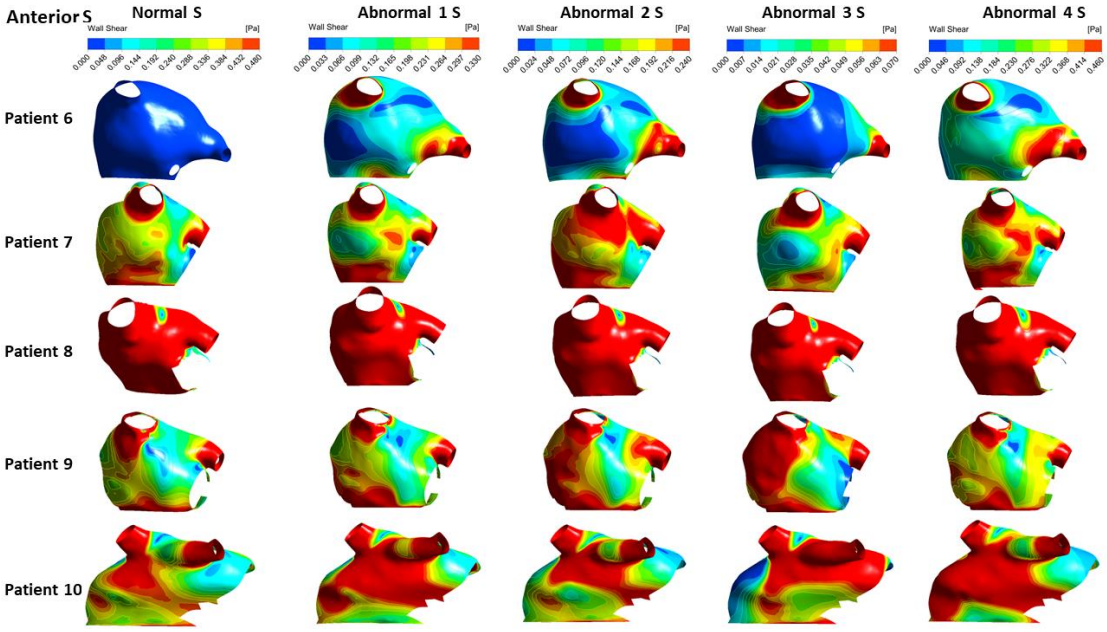

Figure 7.10. WSS values at the anterior side of the LA for patients 6-10.

In Figure 7.11 there are presented the last patients 11-13. These patients revealed high WSS values, where patients 11, 12 indicated high WSS at the whole LA area, instead patient 13 demonstrated mostly at the MV area.

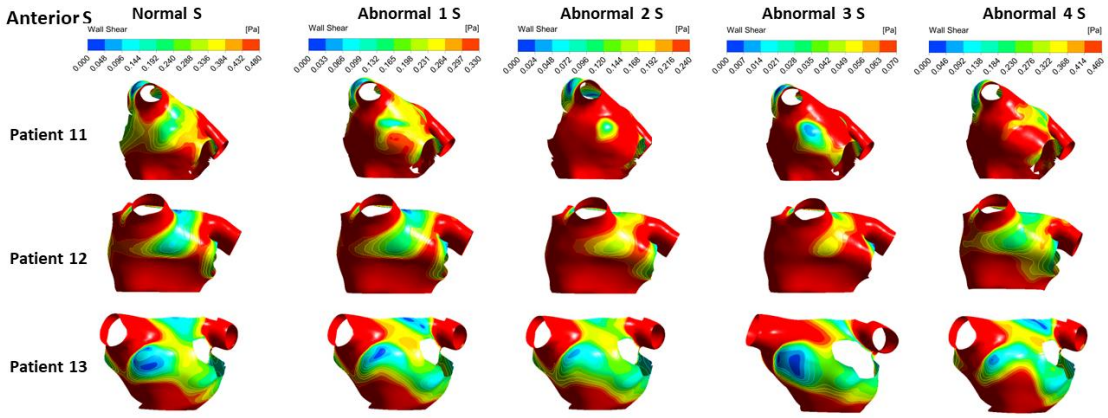

Figure 7.11. WSS values at the anterior side of the LA for patients 10-13.

Figure 7.12 depicts the WWS alterations of the posterior area of the LA for patients 1-5. Generally, we expect to see higher WWS values than the anterior area that we examined before. Here as we can observe from the contours, the red color is more dominant at most of the geometries, than the previous results at the S phase. Although, patient 2 again revealed the highest WSS values among the studied cohort.

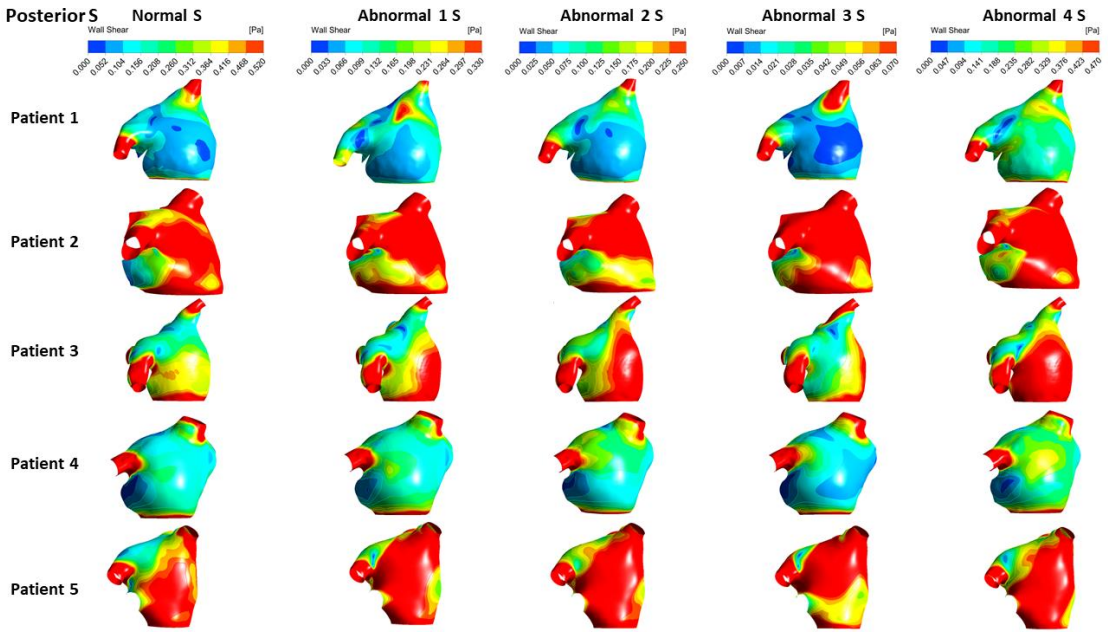

Figure 7.12. WSS values at the posterior side of the LA for patients 1-5.

In Figure 7.13 there are demonstrated the WSS alterations for patients 6-10. Here again patient 6 indicated the lowest values at the normal velocity profile and patient 8 indicated the highest values, with a diminishing area near at the LAA. This circumstance validates our assumption that near and inside the LAA the velocities are weakening.

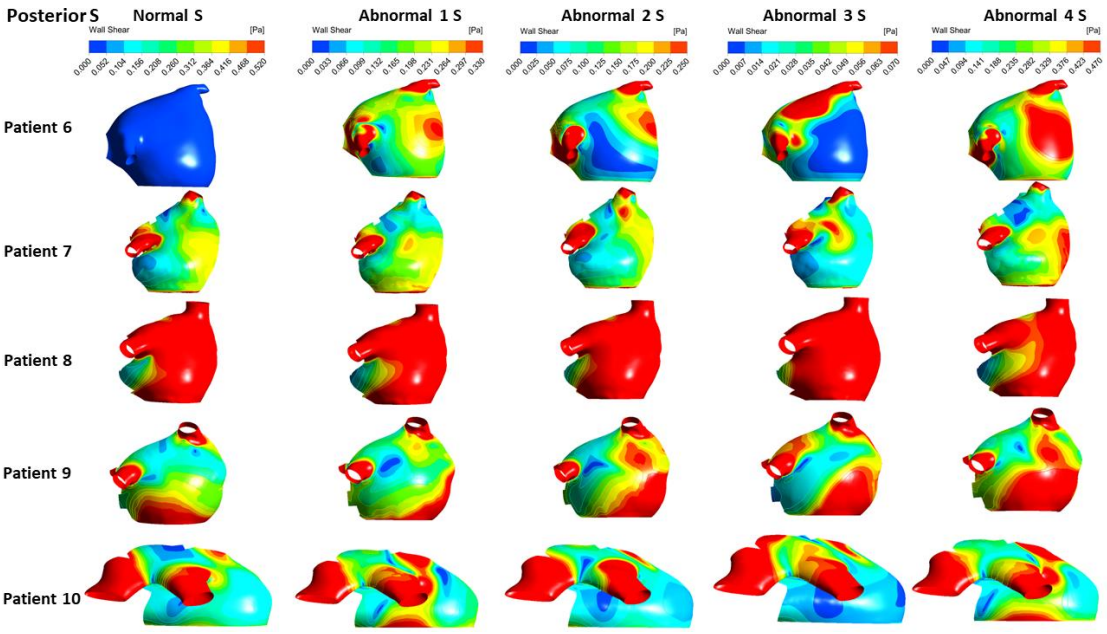

Figure 7.13. WSS values at the anterior side of the LA for patients 6-10.

The last patients 11-13 are demonstrated in Figure 7.14, where patient 11 and patient 12 revealed high WSS values at the whole area, while patient 13 indicated principally high WSS at the mitral valve area.

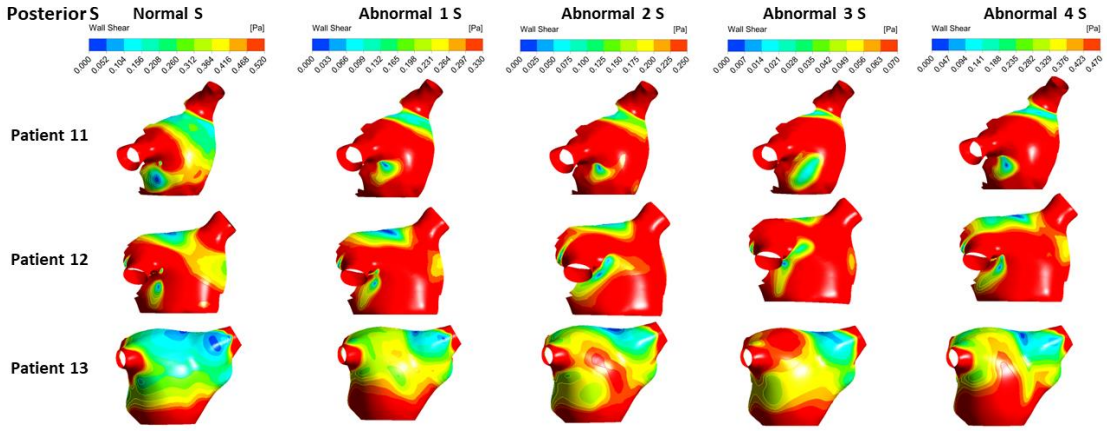

Figure 7.14. WSS values at the anterior side of LA for patients 10-13.

Above we examined and demonstrated the results for the WSS alterations during the implementation of different velocity profiles. All the above results are referring to the S phase of the cardiac cycle where the atrium works like a reservoir. The WSS values varied significantly at most of the cases in different regions of the same LA but also of the same LA.

All he visualizations of the WSS values regarding the D phase both for anterior and posterior areas can be found in the part A of the Appendix.

In Figure 7.15 is depicted with box plots, the mean values of the resulting WSSs at the posterior and the anterior area. The highest values were revealed at the implementation of the Abnormal

4 velocity profile and the lowest at the Abnormal 3 profile. As we can observe the boxes are indicating that the posterior area has higher values both at the two phases (S, D). The only one condition that the anterior area had higher values is at the Normal velocity profile with a tiny difference.

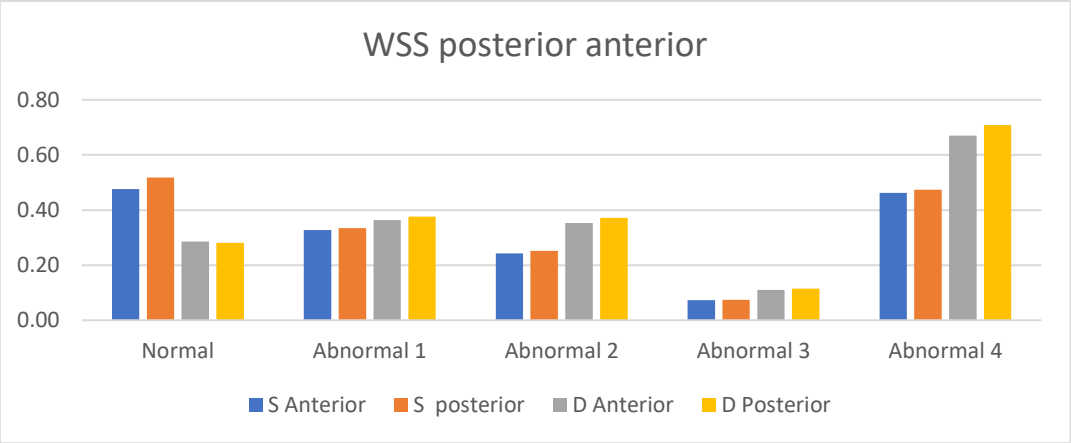

Figure 7.15. Mean WSS results for posterior and anterior views for the LA.

7.2.2 LAA

As we mentioned at Chapter 6, we developed a methodology to calculate more accurately the WSS values at the LAA cavity and demonstrate the results from the orifice to the tip area. In Figure 7.16 the mean WSS values, extracted from all the patients, regarding the implemented velocity profiles are depicted in a box plot. The highest WSS values revealed at the Abnormal 4 velocity profile at the D phase, where most of the velocity profiles had their maximum velocities. Once more, the Abnormal 3 profile indicated the lowest values.

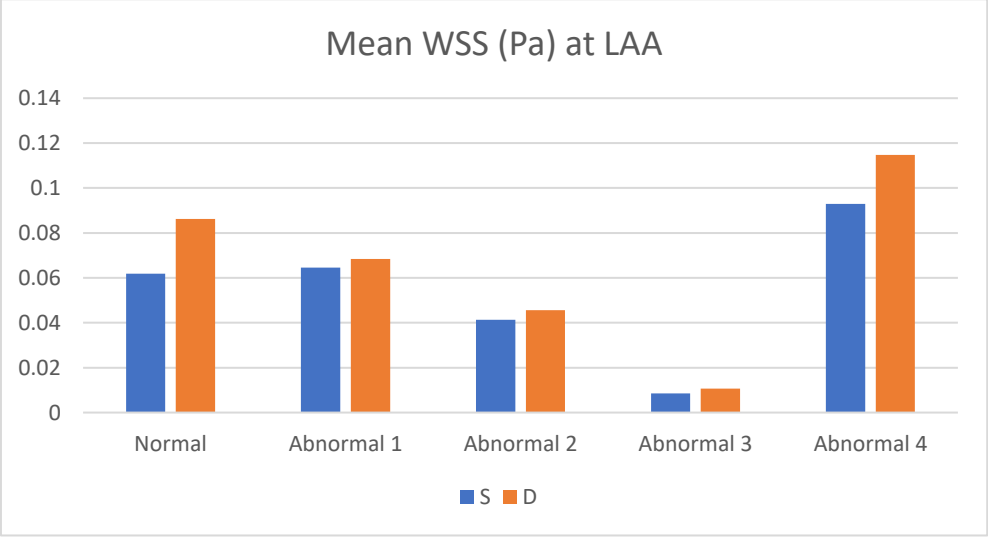

Figure 7.16. Mean values for WSS results extracted from the LAA's generated cross-sections.

Figure 7.17 presents graphs regarding the WSS results per cross-section upon the LAA surface. The results indicated that the lowest WSS values were extracted from the Abnormal 3 velocity profile. The other profiles and their resulting values varied among the different LAA morphologies. Moreover, regarding the WSS values patients 1, 3, 6, 7, 8, 11, 13 indicated an immediate dropdown before the middle area of the appendage. In contrast, patients 2, 4, 5, 9, 10, 12 maintained normal WSS values at the orifice and middle area, before they had their dropdown after the middle area and as reaching the tip.

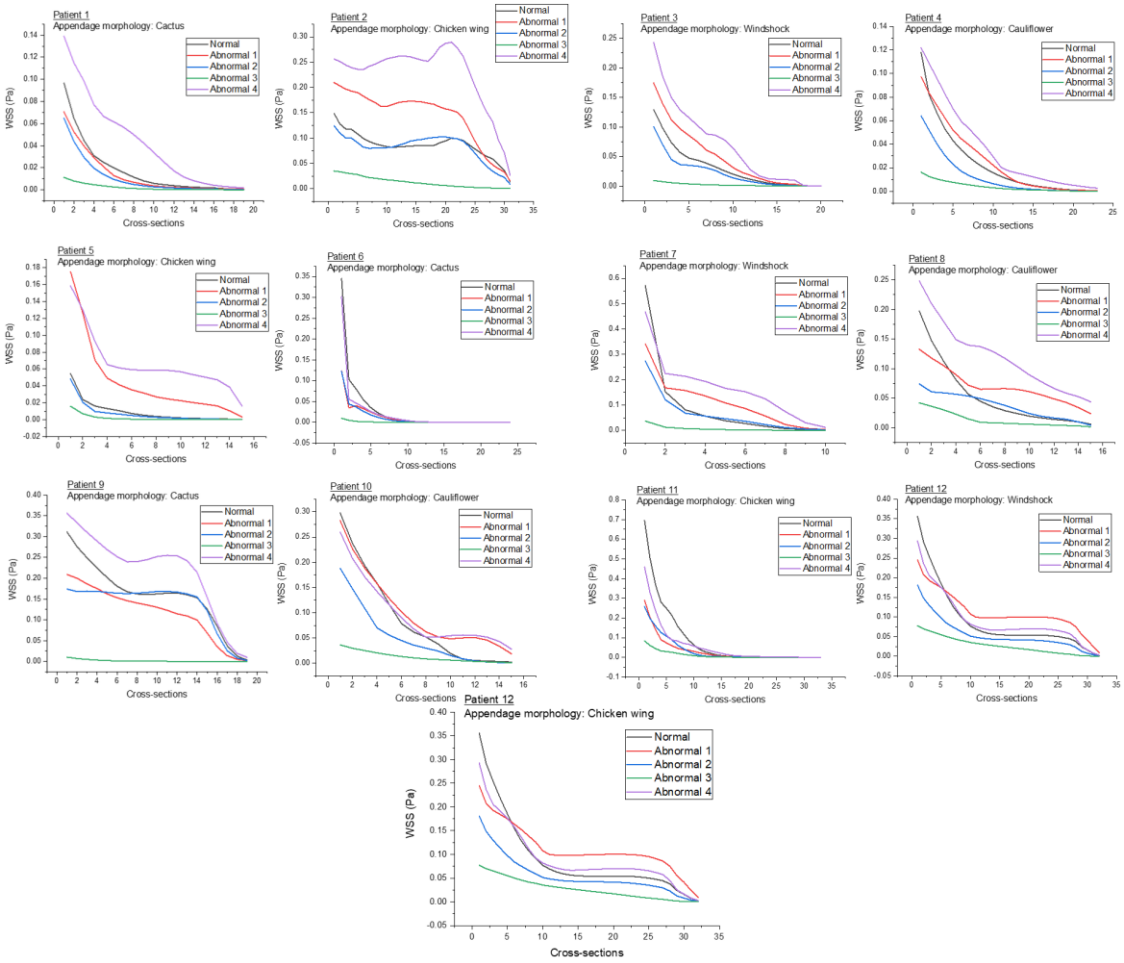

Figure 7.17. WSS results for the LAA cavity, produced from the generated cross-sections.

In Figure 7.18 the visualizations of the WSS for patients 1-5 at the S wave at the LAA cavity are demonstrated. All the patients indicated high WSS values at the orifice area of the appendage, some intermediate values at the mid area of the LAA and low values at the tip. The anatomical morphology here has significant impact as we can observe from the demonstrated distributions. Among all the morphologies, the chicken wing morphology at patient 2 indicated high WSS values almost at the whole LAA cavity, as a small area at the tip had low values. That indicates that the blood flow inside this type of morphology is quite normal and the chances for the blood to stagnate are low. On the other hand, all the other morphologies have

indicated a larger area with low WSS values, especially the windsock and the cauliflower morphologies.

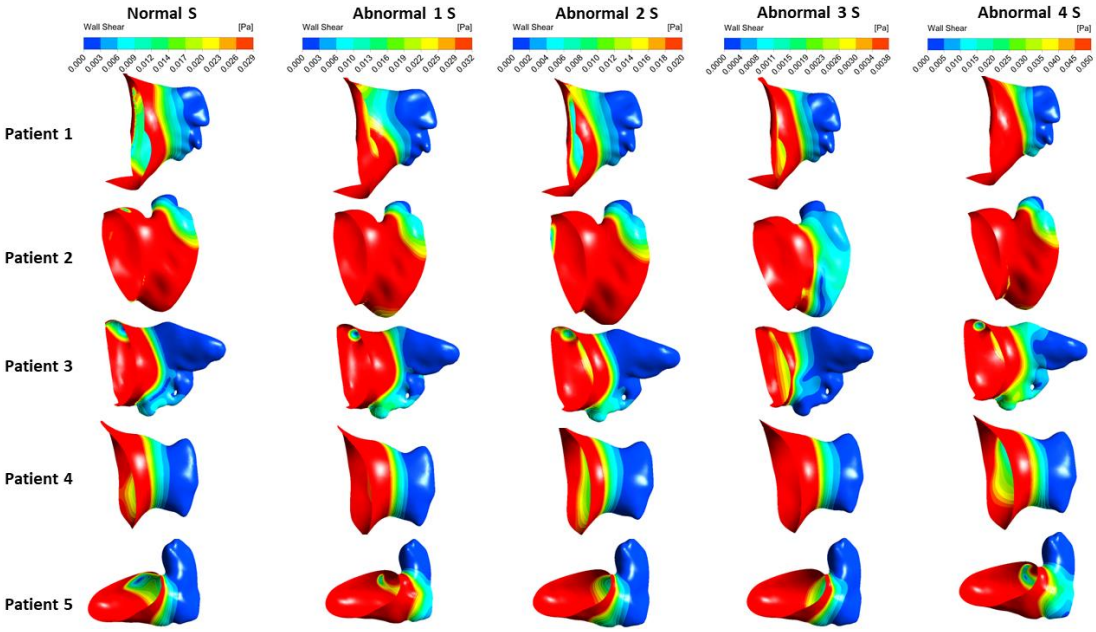

Figure 7.18. LAA WSS visualizations for patients 1-5.

Furthermore, the patients 6-10 are depicted in Figure 7.19. Again, here the lowest values have been indicated at the morphology of patient 6 which is a special occasion. The highest WSS values examined at patient 10 with the cauliflower morphology. The main cavity of the appendage indicated high WSS and a small area at the tip indicated intermediate values. Although, the lowest values can be observed at the tip area of the appendage from patient 7 with the windsock morphology.

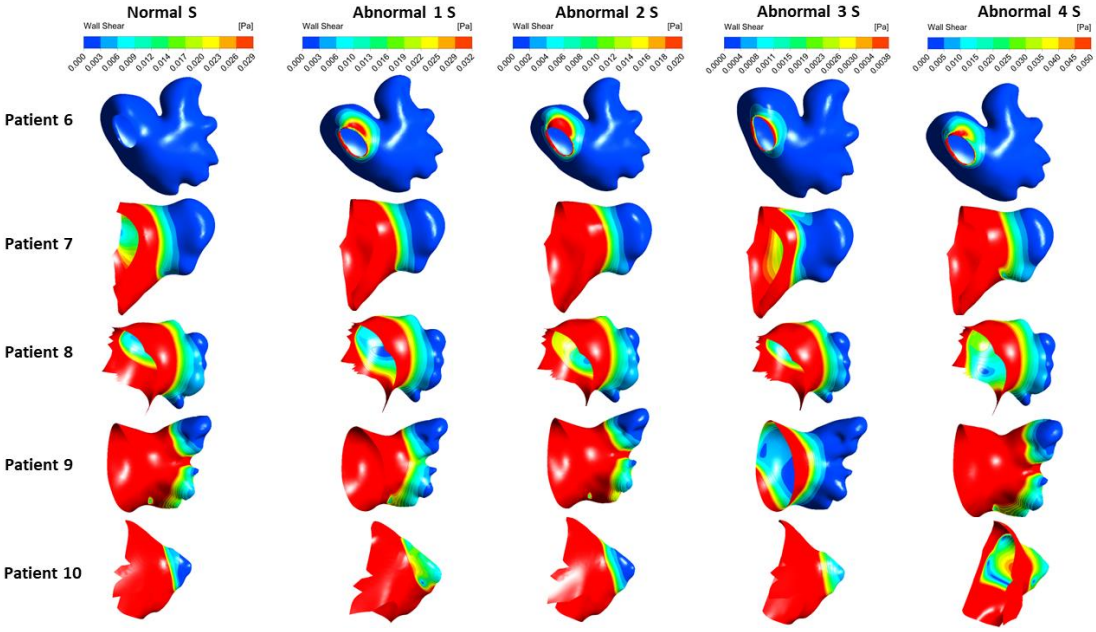

Figure 7.19. LAA WSS visualizations for patients 6-10.

The rest patients (patient 11-13) are demonstrated in Figure 7.20. Patients 11-12 indicated an overall large appendage and a large area with lows WSS values from its mid surface until the tip. Based on the long tubercular shape of these morphologies the tip area is critical for blood to stagnate. Moreover, patient 12 indicated quite good distributions with a very small tip area with low WSS values.

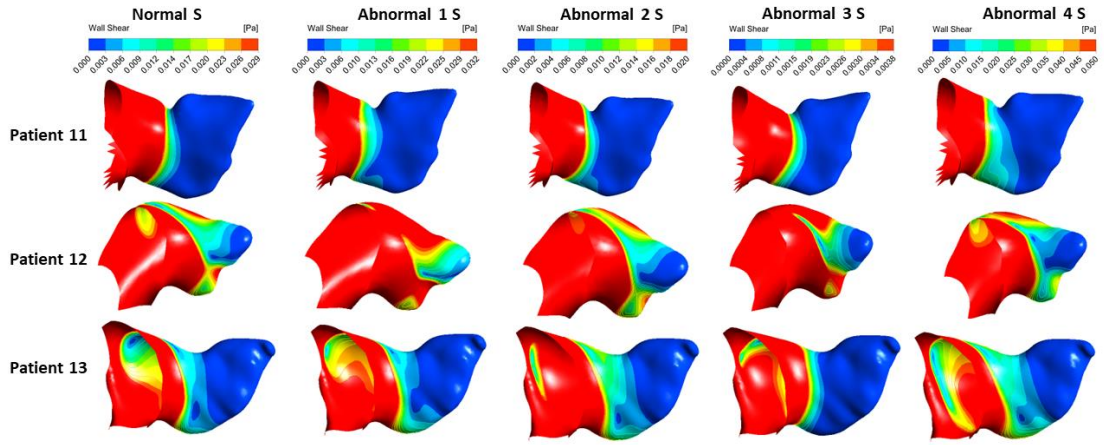

Figure 7.20. LAA WSS visualizations for patients 11-13.

At all the results at the LAA indicated overall high WSS values at the orifice area and low values at the tip. The distributions varied significantly among the different anatomical morphologies of the appendages.

Patient 6

The reconstructed patient's 6 anatomy consists a special occasion. Patient 6 provided by the clinicians to us as a black box case. The results from our reconstruction and our simulations verified and validated that this appendage had suffered from LAA surgical closure. Afterwards the assessment of the results, the clinical expert confirmed that had performed the surgery to that patient and the findings confirmed the patient's case. For that reason, patient's 6 appendage indicated the lowest velocities and WSS as its orifice area had its diameter (d = 0.074 cm) diminished to prevent the blood flow through the appendage cavity, as his condition was considered critical for thrombus formation.

The velocities and the WSS results indicated significant variability among the 13 patients. About the LA cavity, the results indicated that the PV and MV areas are consisted more critical as they indicated the highest WSS values. Moreover, the posterior side exhibited higher WSS values than the anterior side, at most of the implemented velocity profiles. Especially regarding the LAA the impact of the anatomical morphology is momentous. The highlight that the impact of the appendage morphology is significant, were signified by the abnormal WSS values regarding the input velocity profiles. More specifically, the highest velocity profile didn't always indicate the highest values among different anatomical morphologies.

7.2.3 Appendage morphological impact on thrombus formation

Above we examined and demonstrated the resulting velocity and WSS values. These parameters are critical, and they are directly connected with the thrombus formation. Low velocities with combination of an atrial disease such as AF, can lead to thrombus creation inside the LAA cavity. Our blood flow simulations confirmed the literature and can classify the LAA morphologies responsible for high and low velocities as chicken wing > cauliflower > windsock > cactus. Furthermore, the strange tubercular morphology of the LAA and the low blood flow velocities, set up the perfect conditions for a thrombus creation. The LAA structure has complex internal characteristics and irregular tissue projections known as lobes. The tip is considered to have a more irregular shape than the orifice and for that reason is more prone to thrombosis [6, 25, 63]. Afterwards, a pathologic condition that is characterized by high velocities and high WSS values, can lead to a thrombus detachment which will lead to serious health complications. For that reason, diseases such as the AF are dangerous for thrombogenesis inside the LAA. Although, to examine more accurately the LAA's impact on thrombus formation, more parameters need to be included and examined in combination with a more realistic blood flow modeling.

Chapter 8. Conclusions and future work

The mathematical description of the CVD system is a much promising research field and the current technologies and tools can potentially provide information to pivot a step further. The results in the present thesis stem from 2 years of intensive work and exhibited a decent confirmation that the usage of CFD can provide a better interconnection between research and clinical practice.

At this study image processing, 3D reconstruction and CFD analysis were implemented to study the left atrium and to assess the behavior of the different anatomical morphologies of the LAA. The aim of this study was to develop an appropriate approach for patient-specific reconstruction and local hemodynamics characterization of LA and LAA. Reconstructed 3D models from 13 patients were presented. The CFD model that was developed, in order to study their hemodynamics was successfully implemented.

The results regarding the LA and the LAA, have shown good agreement with literature data as other computational and clinical studies have examined [28, 30, 33, 34]. By implementing different velocity profiles, we achieved to analyze the impact of different appendage morphologies on blood flow and their title role at thrombus formation through their homodynamic response. Results indicated that geometrical factors such as volume, length and especially LAA's anatomical characteristics, have significant impact on the hemodynamics.

The computational model we developed at this study, predicted the WSS values based virtuously on velocity input data and on the LA anatomy which considered to be a rigid wall. The calculated velocities for the same patient at the LA cavity didn't have much difference regarding the different implemented velocity profiles. Instead, the same velocity profile showed significant differences among different anatomic geometries from the different studied patients. The shape, the volume, the angle of the PVs and the height of the LA had massive impact on the resulting velocities, as these factors had impact on the visualizations. The WSS alterations varied significantly between patients and the implemented different velocity profiles. Most of the high WSS values raised at areas where the anatomy is quite abnormal and not a normal clean surface. Patients 2, 8, 12 indicated the highest WSS values because of their

abnormal anatomical shape. The PV area had constantly high WSS values at most of the patients cases, and that is a primal indication that the PVs can potentially get an excitatory response, as observations have examined [36, 67].

The LAA is considered to be a common area for thrombus formation specially in the setting of AF disease. The tip area of the LAA revealed much lower and WSS values instead of the orifice area. Regarding the complex morphology and our results, the LAA tip area is consisted to be more prone to blood stagnation as the blood cannot achieve a normal flow at the end of this cavity, and as we mentioned above WSS alterations confirmed that. Also, LAA's complex structure sets tough paths for blood to flow, as its abnormal structure can't provide normal laminar flow conditions. Low velocity and low WSS values have substantial impact on blood stagnation which is a critical factor for thrombogenesis.

Concluding, this study can potentially provide an applied procedure to shed light at the LA and LAA. Studies referring to the pathophysiology of the LA can include mathematical approaches and 3D models to enhance their impact and avoid invasive procedures.

All the above represent an opinion of the author. Certainly, further work should be done to provide better accuracy and realism to boost the outcomes. As a next step of this work is to develop a fully contractile atrial model including wall tissue mechanical material properties. Also, the model could be developed with a realistic moving MV or the whole left ventricle to generate a fully realistic functional 3D model to predict thrombosis at atriums that suffer from AF.

References

[1] P. D. Morris et al., “Computational fluid dynamics modelling in cardiovascular medicine,” Heart, vol. 102, no. 1, pp. 18–28, Jan. 2016, doi: 10.1136/heartjnl-2015-308044.

[2] A. A. Aksenov, S. A. Kharchenko, V. N. Konshin, and V. I. Pokhilko, “- FlowVision software: Numerical simulation of industrial CFD applications on parallel computer systems,” in Parallel Computational Fluid Dynamics 2003, A. Ecer, N. Satofuka, J. Periaux, and P. Fox, Eds. Amsterdam: Elsevier, 2004, pp. 401–408.

[3] L. Di Biase et al.., “Does the Left Atrial Appendage Morphology Correlate With the Risk of Stroke in Patients With Atrial Fibrillation?,” Journal of the American College of Cardiology, vol. 60, no. 6, pp. 531–538, Aug. 2012, doi: 10.1016/j.jacc.2012.04.032.

[4] “Heart Disease and Stroke Statistics—2019 Update: A Report From the American Heart Association,” p. 473.

[5] H. Hatze, “The meaning of the term ‘biomechanics,’” Journal of Biomechanics, vol. 7, no. 2, pp. 189–190, Mar. 1974, doi: 10.1016/0021-9290(74)90060-8.

[6] L. Di Biase, A. Natale, and J. Romero, “Thrombogenic and Arrhythmogenic Roles of the Left Atrial Appendage in Atrial Fibrillation: Clinical Implications,” Circulation, vol. 138, no. 18, pp. 2036–2050, Oct. 2018, doi: 10.1161/CIRCULATIONAHA.118.034187.

[7] A. Fyrenius, “Three dimensional flow in the human left atrium,” Heart, vol. 86, no. 4, pp. 448–455, Oct. 2001, doi: 10.1136/heart.86.4.448.

[8] H. Oertel, K. Spiegel, and S. Donisi, “Modelling the Human Cardiac Fluid Mechanics,” p. 46.

[9] W. P. Abhayaratna et al., “Left Atrial Size,” Journal of the American College of Cardiology, vol. 47, no. 12, pp. 2357–2363, Jun. 2006, doi: 10.1016/j.jacc.2006.02.048.

[10] F. D. Silva, “The role of R-spondin3 in coronary artery formation and novel roles for retinoic acid signaling in cardiac development and repair,” p. 197.

[11] L. Garrett, “The Heart and Cardiovascular Function,” p. 142, 2018.

[12] M. J. Kern, M. J. Lim, and J. A. Goldstein, Eds., Hemodynamic rounds: interpretation of cardiac pathophysiology from pressure waveform analysis, Fourth edition. Hoboken, NJ: Wiley, 2018.

[13] P. Ganesan, M. Sterling, S. Ladavich, and B. Ghoraani, “Computer-Aided Clinical Decision Support Systems for Atrial Fibrillation,” in Computer-aided Technologies - Applications in Engineering and Medicine, R. Udroiu, Ed. InTech, 2016.

[14] B. J. Gersh, Mayo Clinic heart book : the ultimate guide to heart health. New York : W. Morrow, 2000.

[15] M. J. Vieira, R. Teixeira, L. Gonçalves, and B. J. Gersh, “Left Atrial Mechanics: Echocardiographic Assessment and Clinical Implications,” Journal of the American Society of Echocardiography, vol. 27, no. 5, pp. 463–478, May 2014, doi: 10.1016/j.echo.2014.01.021.

[16] J. R. Mitchell and J.-J. Wang, “Expanding application of the Wiggers diagram to teach cardiovascular physiology,” Advances in Physiology Education, vol. 38, no. 2, pp. 170–175, Jun. 2014, doi: 10.1152/advan.00123.2013.

[17] N. M. Al-Saady, O. A. Obel, and A. J. Camm, “Left atrial appendage: structure, function, and role in thromboembolism,” Heart, vol. 82, no. 5, pp. 547–554, Nov. 1999, doi: 10.1136/hrt.82.5.547.

[18] S. Whiteman et al., “An anatomical review of the left atrium,” Translational Research in Anatomy, vol. 17, p. 100052, Nov. 2019, doi: 10.1016/j.tria.2019.100052.

[19] S. Y. Ho, J. A. Cabrera, and D. Sanchez-Quintana, “Left Atrial Anatomy Revisited,” Circulation: Arrhythmia and Electrophysiology, vol. 5, no. 1, pp. 220–228, Feb. 2012, doi: 10.1161/CIRCEP.111.962720.

[20] S. Qamruddin, J. Shinbane, J. Shriki, and T. Z. Naqvi, “Left atrial appendage: structure, function, imaging modalities and therapeutic options,” Expert Review of Cardiovascular Therapy, vol. 8, no. 1, pp. 65–75, Jan. 2010, doi: 10.1586/erc.09.161.

[21] N. Naksuk, D. Padmanabhan, V. Yogeswaran, and S. J. Asirvatham, “Left Atrial Appendage,” JACC: Clinical Electrophysiology, vol. 2, no. 4, pp. 403–412, Aug. 2016, doi: 10.1016/j.jacep.2016.06.006.
[22] M. Korhonen et al., “Left Atrial Appendage Morphology in Patients with Suspected Cardiogenic Stroke without Known Atrial Fibrillation,” PLOS ONE, vol. 10, no. 3, p. e0118822, Mar. 2015, doi: 10.1371/journal.pone.0118822.
[23] G. Ernst et al., “Morphology of the left atrial appendage: LEFT ATRIAL APPENDAGE,” The Anatomical Record, vol. 242, no. 4, pp. 553–561, Aug. 1995, doi: 10.1002/ar.1092420411.
[24] N. Y. Tan, O. Z. Yasin, A. Sugrue, A. El Sabbagh, T. A. Foley, and S. J. Asirvatham, “Anatomy and Physiologic Roles of the Left Atrial Appendage,” Interventional Cardiology Clinics, vol. 7, no. 2, pp. 185–199, Apr. 2018, doi: 10.1016/j.iccl.2017.12.001.
[25] F. Khan, C. Vaillancourt, and G. Bourjeily, “Diagnosis and management of deep vein thrombosis in pregnancy,” BMJ, p. j2344, May 2017, doi: 10.1136/bmj.j2344.
[26] R. Beigel, N. C. Wunderlich, S. Y. Ho, R. Arsanjani, and R. J. Siegel, “The Left Atrial Appendage: Anatomy, Function, and Noninvasive Evaluation,” JACC: Cardiovascular Imaging, vol. 7, no. 12, pp. 1251–1265, Dec. 2014, doi: 10.1016/j.jcmg.2014.08.009.
[27] O. H. Karatas and E. Toy, “Three-dimensional imaging techniques: A literature review,” European Journal of Dentistry, vol. 08, no. 01, pp. 132–140, Jan. 2014, doi: 10.4103/1305-7456.126269.
[28] S. P. Salzberg, M. Y. Emmert, and E. Caliskan, “Surgical techniques for left atrial appendage exclusion,” Herzschrittmachertherapie + Elektrophysiologie, vol. 28, no. 4, pp. 360–365, Dec. 2017, doi: 10.1007/s00399-017-0532-0.
[29] R. Deegan, C. R. Ellis, and J. M. Bennett, “Left Atrial Appendage Occlusion Devices,” Seminars in Cardiothoracic and Vascular Anesthesia, p. 18.
[30] G. Venkataraman et al., “Short-term safety and efficacy of left atrial appendage closure with the WATCHMAN device in patients with small left atrial appendage ostia,” p. 8.
[31] E. S. Di Martino, C. Bellini, and D. S. Schwartzman, “In vivo porcine left atrial wall stress: Computational model,” Journal of Biomechanics, vol. 44, no. 15, pp. 2589–2594, Oct. 2011, doi: 10.1016/j.jbiomech.2011.08.023.
[32] T. Otani, A. Al-Issa, A. Pourmorteza, E. R. McVeigh, S. Wada, and H. Ashikaga, “A Computational Framework for Personalized Blood Flow Analysis in the Human Left Atrium,” Annals of Biomedical Engineering, vol. 44, no. 11, pp. 3284–3294, Nov. 2016, doi: 10.1007/s10439-016-1590-x.
[33] V. Vedula, R. George, L. Younes, and R. Mittal, “Hemodynamics in the Left Atrium and Its Effect on Ventricular Flow Patterns,” Journal of Biomechanical Engineering, vol. 137, no. 11, Nov. 2015, doi: 10.1115/1.4031487.
[34] M. Markl et al., “Left atrial and left atrial appendage 4D blood flow dynamics in atrial fibrillation,” Journal of Cardiovascular Magnetic Resonance, vol. 18, no. Suppl 1, p. O90, 2016, doi: 10.1186/1532-429X-18-S1-O90.
[35] A. Masci et al., “Development of a Computational Fluid Dynamics Model of the Left Atrium in Atrial Fibrillation on a Patient Specific Basis,” presented at the 2017 Computing in Cardiology Conference, Sep. 2017, doi: 10.22489/CinC.2017.004-429.
[36] O. Hazan et al., “An innovative appendage invagination procedure to reduce thrombus formation – a numerical model,” Computer Methods in Biomechanics and Biomedical Engineering, vol. 21, no. 4, pp. 370–378, Mar. 2018, doi: 10.1080/10255842.2018.1466116.
[37] A. Satriano, E. J. Vigmond, D. S. Schwartzman, and E. S. Di Martino, “Mechano-electric finite element model of the left atrium,” Computers in Biology and Medicine, vol. 96, pp. 24–31, May 2018, doi: 10.1016/j.compbiomed.2018.02.010.
[38] G. M. Bosi et al., “Computational Fluid Dynamic Analysis of the Left Atrial Appendage to Predict Thrombosis Risk,” Frontiers in Cardiovascular Medicine, vol. 5, pp. 34–38, Apr. 2018, doi: 10.3389/fcvm.2018.00034.

[39] R. J. Hunter, Y. Liu, Y. Lu, W. Wang, and R. J. Schilling, “Left Atrial Wall Stress Distribution and Its Relationship to Electrophysiologic Remodeling in Persistent Atrial Fibrillation,” Circulation: Arrhythmia and Electrophysiology, vol. 5, no. 2, pp. 351–360, Apr. 2012, doi: 10.1161/CIRCEP.111.965541.
[40] Q. Tao, E. G. Ipek, R. Shahzad, F. F. Berendsen, S. Nazarian, and R. J. van der Geest, “Fully automatic segmentation of left atrium and pulmonary veins in late gadolinium-enhanced MRI: Towards objective atrial scar assessment: LA and PV Segmentation in LGE MRI,” Journal of Magnetic Resonance Imaging, vol. 44, no. 2, pp. 346–354, Aug. 2016, doi: 10.1002/jmri.25148.
[41] C. Ma, G. Luo, and K. Wang, “A Combined Random Forests and Active Contour Model Approach for Fully Automatic Segmentation of the Left Atrium in Volumetric MRI,” BioMed Research International, vol. 2017, pp. 1–14, 2017, doi: 10.1155/2017/8381094.
[42] M. Valinoti, C. Fabbri, D. Turco, R. Mantovan, A. Pasini, and C. Corsi, “3D patient-specific models for left atrium characterization to support ablation in atrial fibrillation patients,” Magnetic Resonance Imaging, vol. 45, pp. 51–57, Jan. 2018, doi: 10.1016/j.mri.2017.09.012.
[43] C. Jin et al., “Left atrial appendage segmentation and quantitative assisted diagnosis of atrial fibrillation based on fusion of temporal-spatial information,” Computers in Biology and Medicine, vol. 96, pp. 52–68, May 2018, doi: 10.1016/j.compbiomed.2018.03.002.
[44] M. Hadjicharalambous, J. Lee, N. P. Smith, and D. A. Nordsletten, “A displacement-based finite element formulation for incompressible and nearly-incompressible cardiac mechanics,” Computer Methods in Applied Mechanics and Engineering, vol. 274, pp. 213–236, Jun. 2014, doi: 10.1016/j.cma.2014.02.009.
[45] G. Farrar et al., “Atlas-based ventricular shape analysis for understanding congenital heart disease,” Progress in Pediatric Cardiology, vol. 43, pp. 61–69, Dec. 2016, doi: 10.1016/j.ppedcard.2016.07.010.
[46] W. E. Lorensen and H. E. Cline, “(~ ~ ComputerGraphics,Volume21, Number4,July1987,” p. 7.
[47] S. Osher and J. A. Sethian, “Fronts propagating with curvature-dependent speed: Algorithms based on Hamilton-Jacobi formulations,” Journal of Computational Physics, vol. 79, no. 1, pp. 12–49, Nov. 1988, doi: 10.1016/0021-9991(88)90002-2.
[48] M. Kass, A. Witkin, and D. Terzopoulos, “Snakes: Active contour models,” International Journal of Computer Vision, vol. 1, no. 4, pp. 321–331, Jan. 1988, doi: 10.1007/BF00133570.
[49] Chenyang Xu and J. L. Prince, “Snakes, shapes, and gradient vector flow,” IEEE Transactions on Image Processing, vol. 7, no. 3, pp. 359–369, Mar. 1998, doi: 10.1109/83.661186.
[50] O. Camara, M. Pop, K. Rhode, M. Sermesant, N. Smith, and A. Young, Eds., Statistical Atlases and Computational Models of the Heart: First International Workshop, STACOM 2010, and Cardiac Electrophysiological Simulation Challenge, CESC 2010, Held in Conjunction with MICCAI 2010, Beijing, China, September 20, 2010. Proceedings, vol. 6364. Berlin, Heidelberg: Springer Berlin Heidelberg, 2013.
[51] Y.-H. Kim, E. M. Marom, J. E. Herndon, and H. P. McAdams, “Pulmonary Vein Diameter, Cross-sectional Area, and Shape: CT Analysis,” Radiology, vol. 235, no. 1, pp. 43–49, Apr. 2005, doi: 10.1148/radiol.2351032106.
[52] L. Formaggia and A. Quarteroni, Eds., Cardiovascular mathematics: modeling and simulation of the circulatory system. Milano: Springer, 2009.
[53] The finite element method and applications in engineering using ansys. New York, NY: Springer Science+Business Media, 2014.
[54] J. F. Wendt, J. D. Anderson, and Von Karman Institute for Fluid Dynamics, Eds., Computational fluid dynamics: an introduction, 3rd ed. Berlin ; [London]: Springer, 2008.
[55] N. Bessonov, A. Sequeira, S. Simakov, Yu. Vassilevskii, and V. Volpert, “Methods of Blood Flow Modelling,” Mathematical Modelling of Natural Phenomena, vol. 11, no. 1, pp. 1–25, 2016, doi: 10.1051/mmnp/201611101.

[56] D. N. Ku, “Blood Flow In Arteries,” Annu. Rev. Fluid Mech., vol. 29, no. 1, pp. 399–434, 1997.
[57] T. G. Mezger, “For users of rotational and oscillatory rheometers,” p. 30.
[58] Y. A. Çengel and J. M. Cimbala, Fluid mechanics: fundamentals and applications, Third edition. New York: McGraw Hill, 2014.
[59] K. Courchaine and S. Rugonyi, “Quantifying blood flow dynamics during cardiac development: demystifying computational methods,” Philosophical Transactions of the Royal Society B: Biological Sciences, vol. 373, no. 1759, p. 20170330, Nov. 2018, doi: 10.1098/rstb.2017.0330.
[60] P. O. Bonetti, L. O. Lerman, and A. Lerman, “Endothelial Dysfunction: A Marker of Atherosclerotic Risk,” Arteriosclerosis, Thrombosis, and Vascular Biology, vol. 23, no. 2, pp. 168–175, Feb. 2003, doi: 10.1161/01.ATV.0000051384.43104.FC.
[61] A. M. Malek, “Hemodynamic Shear Stress and Its Role in Atherosclerosis,” JAMA, vol. 282, no. 21, p. 2035, Dec. 1999, doi: 10.1001/jama.282.21.2035.
[62] J. J. Hathcock, “Flow Effects on Coagulation and Thrombosis,” Arteriosclerosis, Thrombosis, and Vascular Biology, vol. 26, no. 8, pp. 1729–1737, Aug. 2006, doi: 10.1161/01.ATV.0000229658.76797.30.
[63] A. Sakellarios et al., “Prediction of atherosclerotic disease progression using LDL transport modelling: a serial computed tomographic coronary angiographic study,” Eur Heart J Cardiovasc Imaging, vol. 18, no. 1, pp. 11–18, Jan. 2017, doi: 10.1093/ehjci/jew035.
[64] V. V. Genkel, A. O. Salashenko, T. N. Shamaeva, V. A. Sumerkina, and I. I. Shaposhnik, “Association between Carotid Wall Shear Rate and Arterial Stiffness in Patients with Hypertension and Atherosclerosis of Peripheral Arteries,” International Journal of Vascular Medicine, vol. 2018, pp. 1–8, Aug. 2018, doi: 10.1155/2018/6486234.
[65] S. Ricci, A. Swillens, A. Ramalli, M. Cinthio, P. Segers, and P. Tortoli, “Improved Wall Shear Rate method for robust measurements,” in 2014 IEEE International Ultrasonics Symposium, Chicago, IL, USA, Sep. 2014, pp. 432–435, doi: 10.1109/ULTSYM.2014.0107.
[66] J. R. Womersley, “Method for the calculation of velocity, rate of flow and viscous drag in arteries when the pressure gradient is known,” The Journal of Physiology, vol. 127, no. 3, pp. 553–563, Mar. 1955, doi: 10.1113/jphysiol.1955.sp005276.
[67] “Image Digitizer.” https://www.mathworks.com/matlabcentral/fileexchange/49009-image-digitizer (accessed Jul. 15, 2020).
[68] M. Bansal and R. R. Kasliwal, “Echocardiography for left atrial appendage structure and function,” Indian Heart Journal, vol. 64, no. 5, pp. 469–475, Sep. 2012, doi: 10.1016/j.ihj.2012.07.020.
[69] R. Leischik et al., “Echocardiographic Evaluation of Left Atrial Mechanics: Function, History, Novel Techniques, Advantages, and Pitfalls,” BioMed Research International, vol. 2015, pp. 1–12, 2015, doi: 10.1155/2015/765921.
[70] E. J. Shaughnessy, I. M. Katz, and J. P. Schaffer, Introduction to fluid mechanics. New York: Oxford University Press, 2005.
[71] U. Barbero and S. Y. Ho, “Anatomy of the atria: A road map to the left atrial appendage,” Herzschrittmachertherapie + Elektrophysiologie, vol. 28, no. 4, pp. 347–354, Dec. 2017, doi: 10.1007/s00399-017-0535-x.
[72] M. Handke, A. Harloff, A. Hetzel, M. Olschewski, C. Bode, and A. Geibel, “Left Atrial Appendage Flow Velocity as a Quantitative Surrogate Parameter for Thromboembolic Risk: Determinants and Relationship to Spontaneous Echocontrast and Thrombus Formation–A Transesophageal Echocardiographic Study in 500 Patients with Cerebral Ischemia,” Journal of the American Society of Echocardiography, vol. 18, no. 12, pp. 1366–1372, Dec. 2005, doi: 10.1016/j.echo.2005.05.006.
[73] V. Delgado et al., “Structure and Function of the Left Atrium and Left Atrial Appendage,” Journal of the American College of Cardiology, vol. 70, no. 25, pp. 3157–3172, Dec. 2017, doi: 10.1016/j.jacc.2017.10.063.

[74] J. Kalifa et al., “Intra-Atrial Pressure Increases Rate and Organization of Waves Emanating From the Superior Pulmonary Veins During Atrial Fibrillation,” Circulation, vol. 108, no. 6, pp. 668–671, Aug. 2003, doi: 10.1161/01.CIR.0000086979.39843.7B.

Publications

1. Grigoriadis et al. "Computational Fluid Dynamics of Blood Flow at the Left Atrium and Left Atrium Appendage". In: Henriques J., Neves N., de Carvalho P. (eds) XV Mediterranean Conference on Medical and Biological Engineering and Computing - MEDICON 2019. MEDICON 2019. IFMBE Proceedings, vol 76. Springer, Cham, 2019, doi.org/10.1007/978-3-030-31635-8_114.
2. G. I. Grigoriadis et al., "Wall shear stress alterations at left atrium and left atrial appendage employing abnormal blood velocity profiles," 2020 42nd Annual International Conference of the IEEE Engineering in Medicine & Biology Society (EMBC), Montreal, QC, Canada, 2020, pp. 2565-2568. doi: 10.1109/EMBC44109.2020.9175235.
3. V. C. Pezoulas, G. I. Grigoriadis, N. S. Tachos, F. Barlocco, I. Olivotto and D. I. Fotiadis, "Generation of virtual patient data for in-silico cardiomyopathies drug development using tree ensembles: a comparative study," 2020 42nd Annual International Conference of the IEEE Engineering in Medicine & Biology Society (EMBC), Montreal, QC, Canada, 2020, pp. 5343-5346, doi: 10.1109/EMBC44109.2020.9176567.
4. Kosmidou et al., "Development of a novel computational fluid dynamics model applied on cardiac computed tomography for the assessment of regional hemodynamic changes in the LAA during AF or sinus rhythm", Journal of the American College of Cardiology (JACC), vol. 75, no. 11, p. 3494, Mar. 2020, doi: 10.1016/S0735-1097(20)34121-8.

APPENDIX

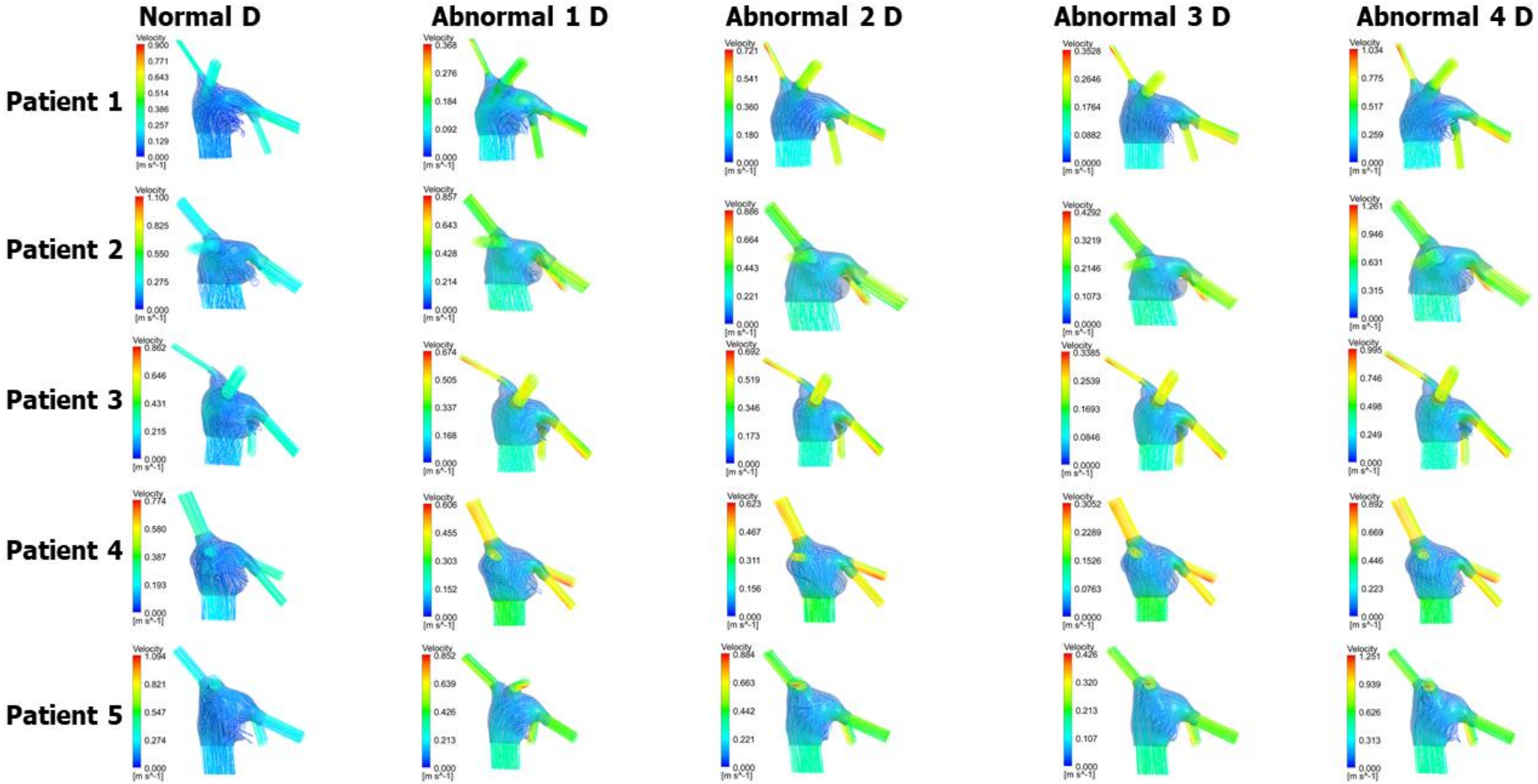

Figure. 1: Velocity streamlines regarding D phase (Patients 1-5).

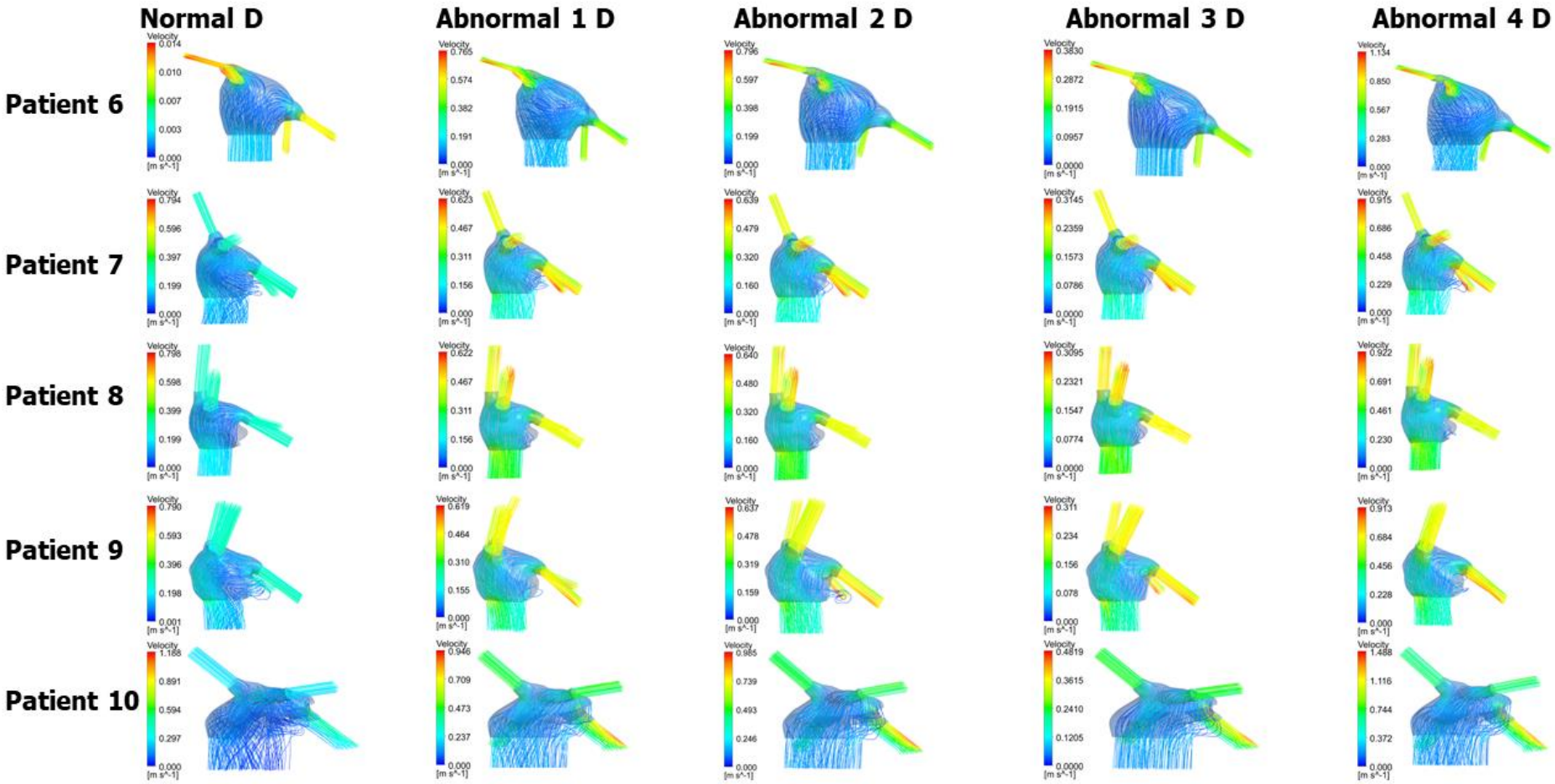

Figure. 2: Velocity streamlines regarding D phase (Patients 6-10).

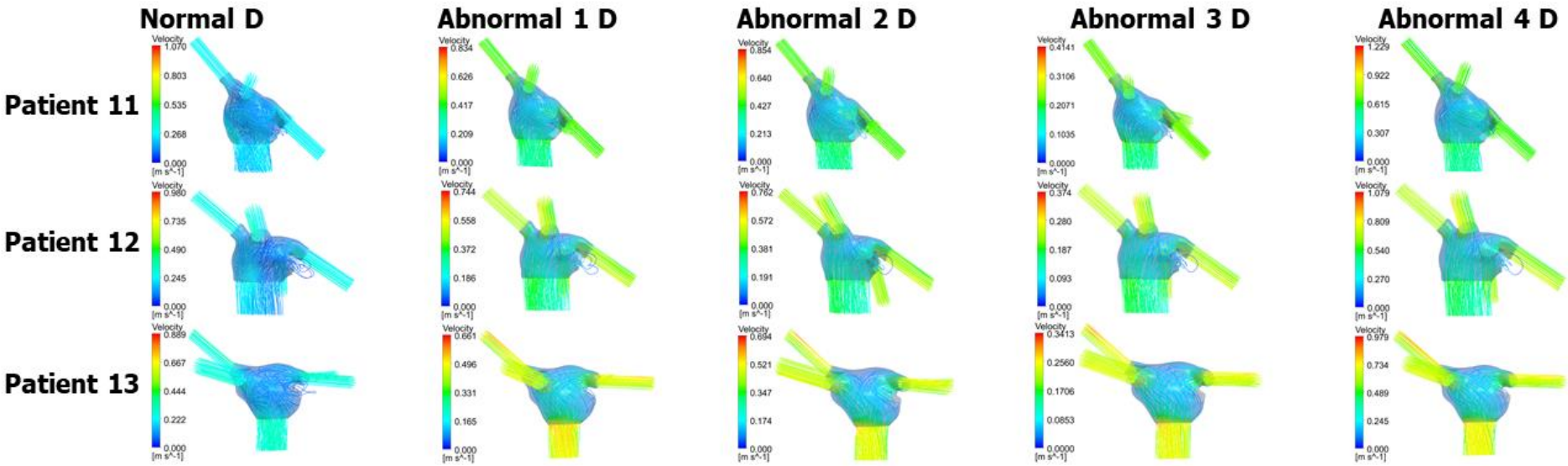

Figure. 3: Velocity streamlines regarding D phase (Patients 11-13).

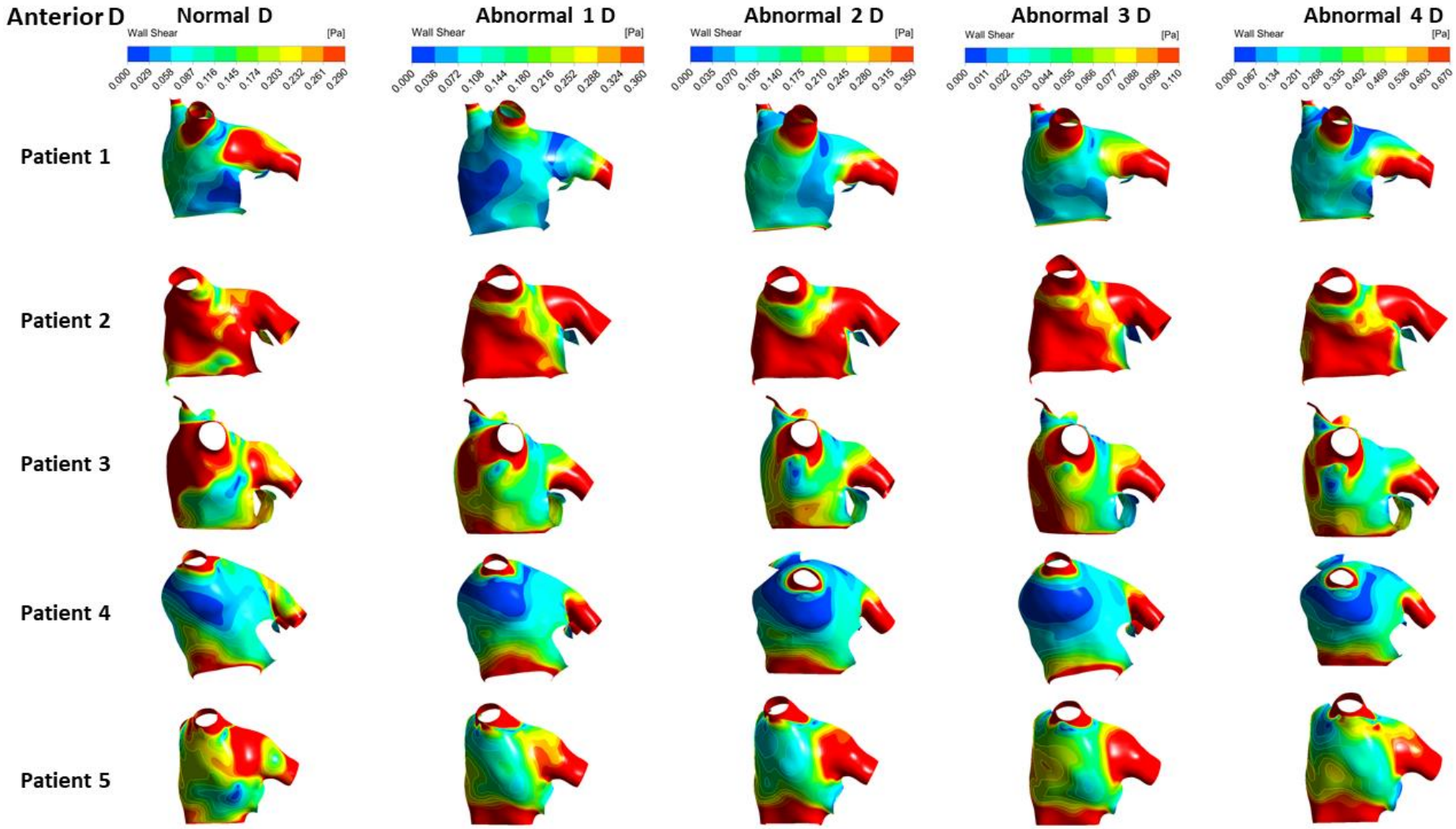

Figure. 4: Anterior WSS alterations regarding D phase (Patients 1-5).

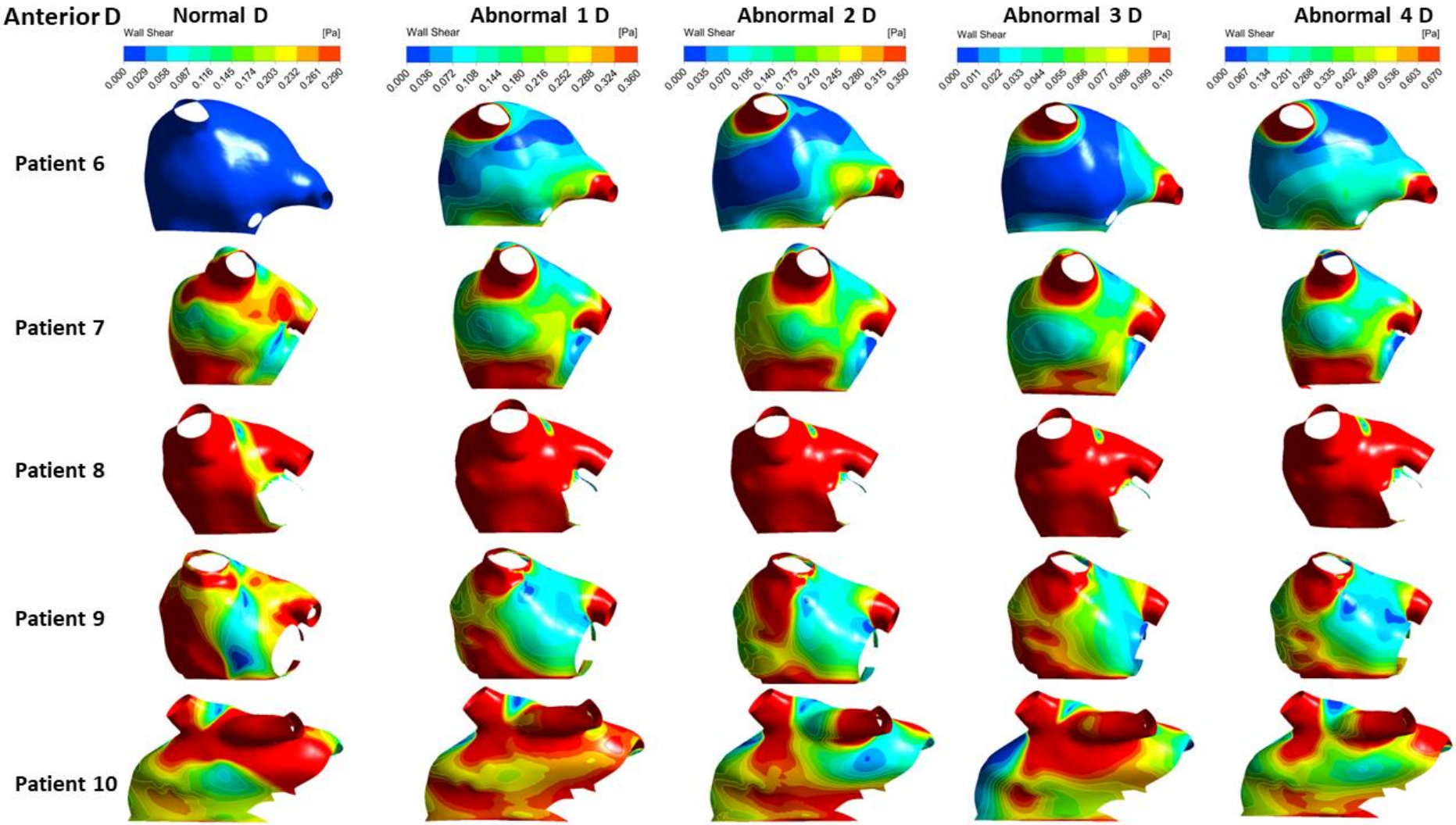

Figure. 5: Anterior WSS alterations regarding D phase (Patients 6-10).

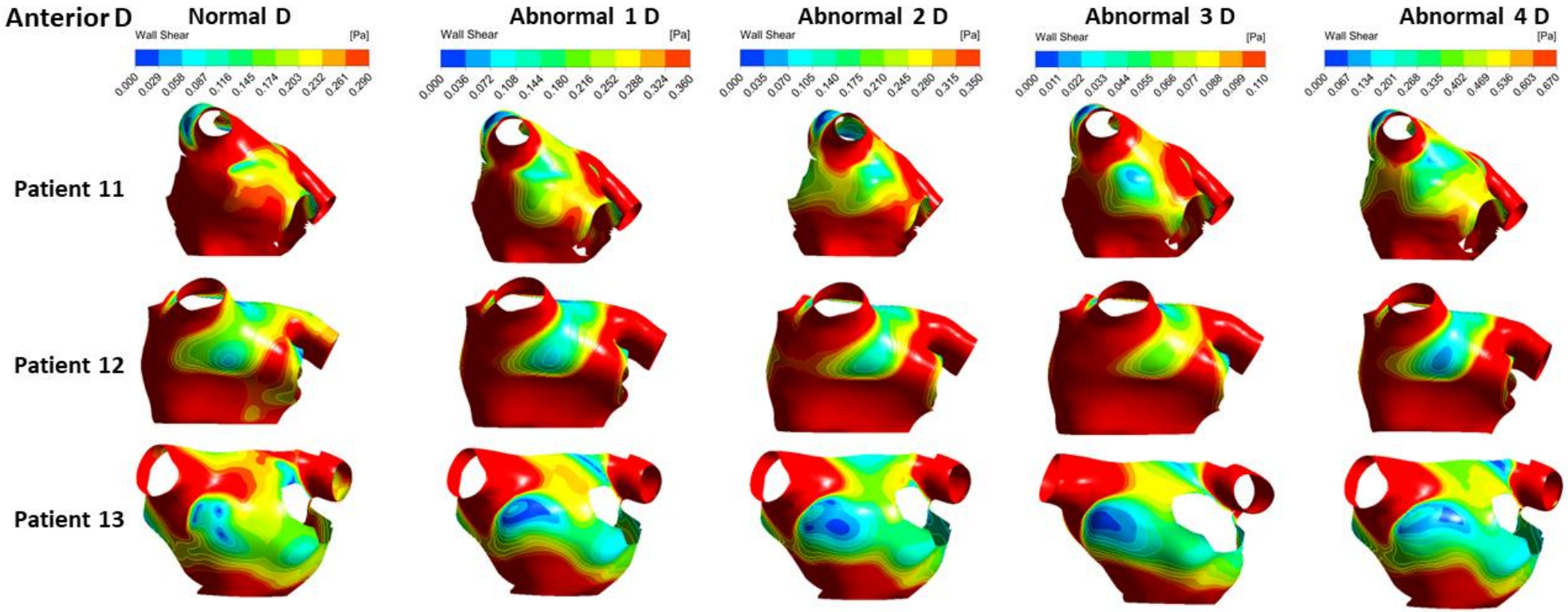

Figure. 6: Anterior WSS alterations regarding D phase (Patients 11-13).

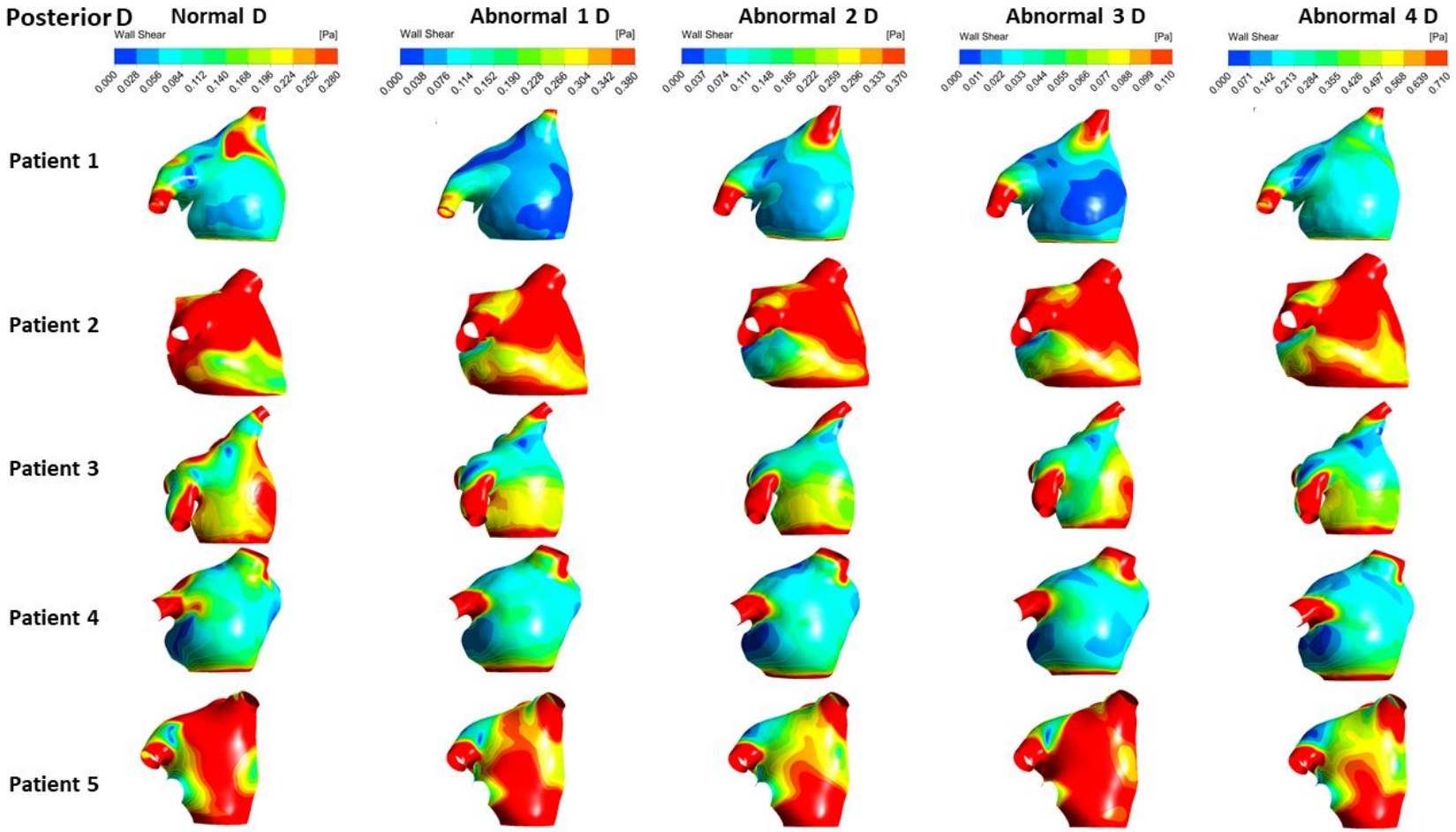

Figure. 7: Posterior WSS alterations regarding the D wave (Patients 1-5).

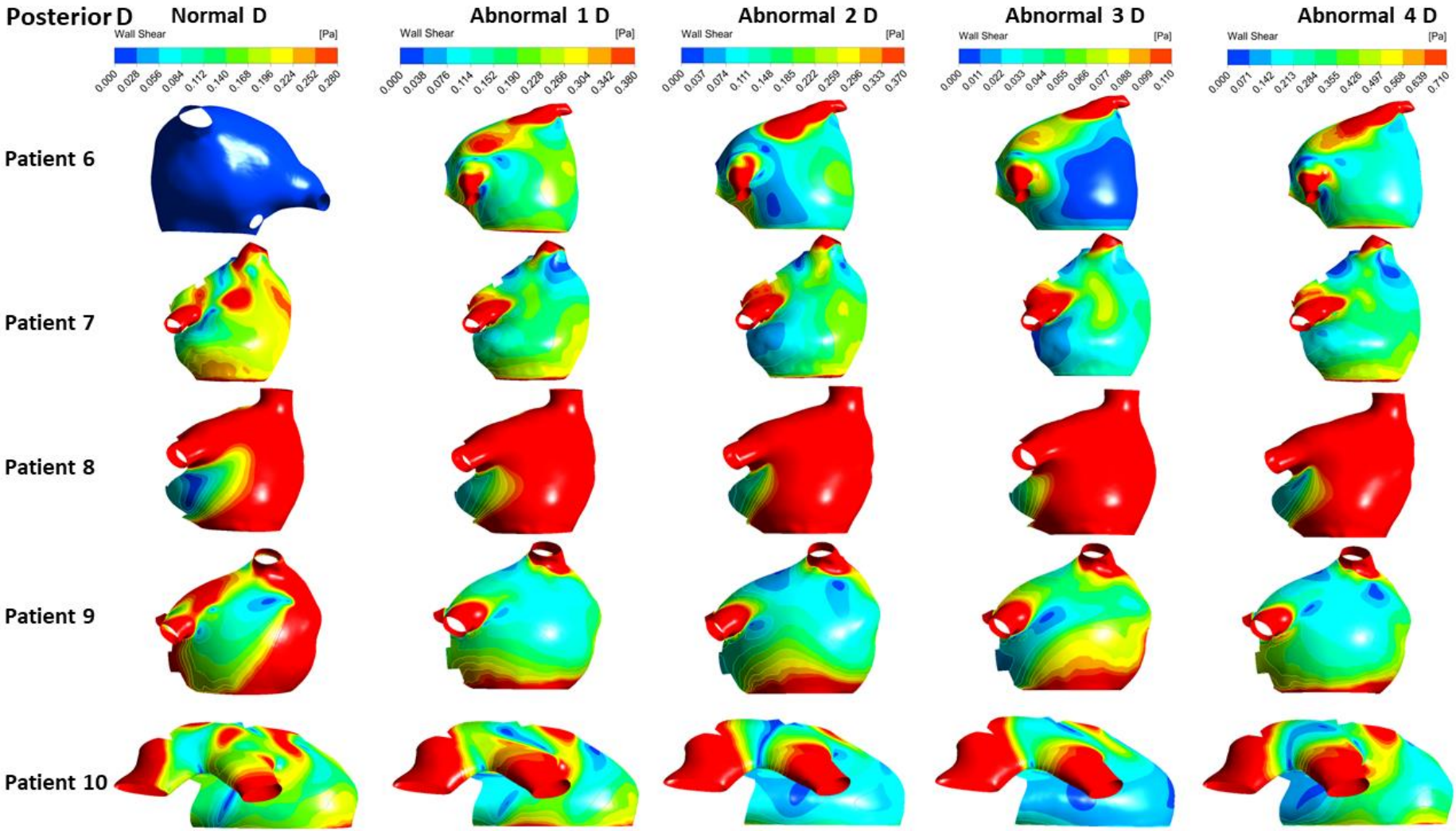

Figure. 8: Posterior WSS alterations regarding the D wave (Patients 6-10).

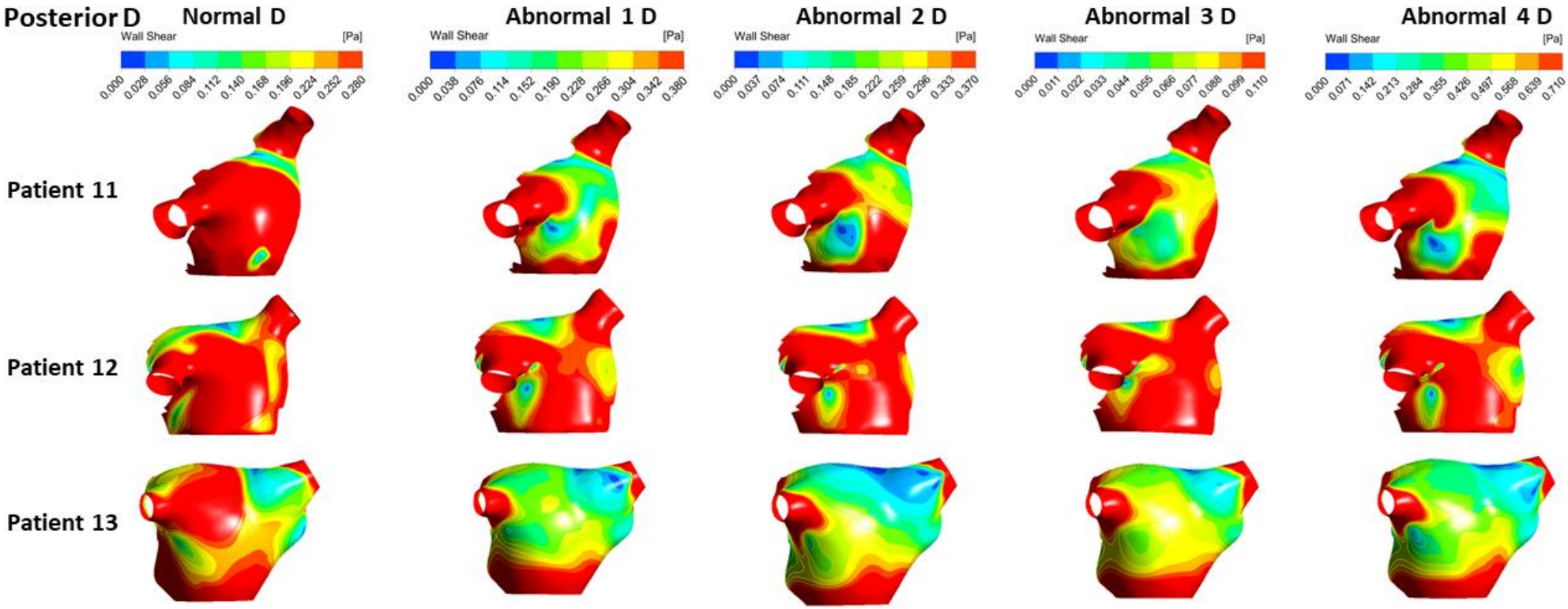

Figure. 9: Posterior WSS alterations regarding the D wave (Patients 11-13).

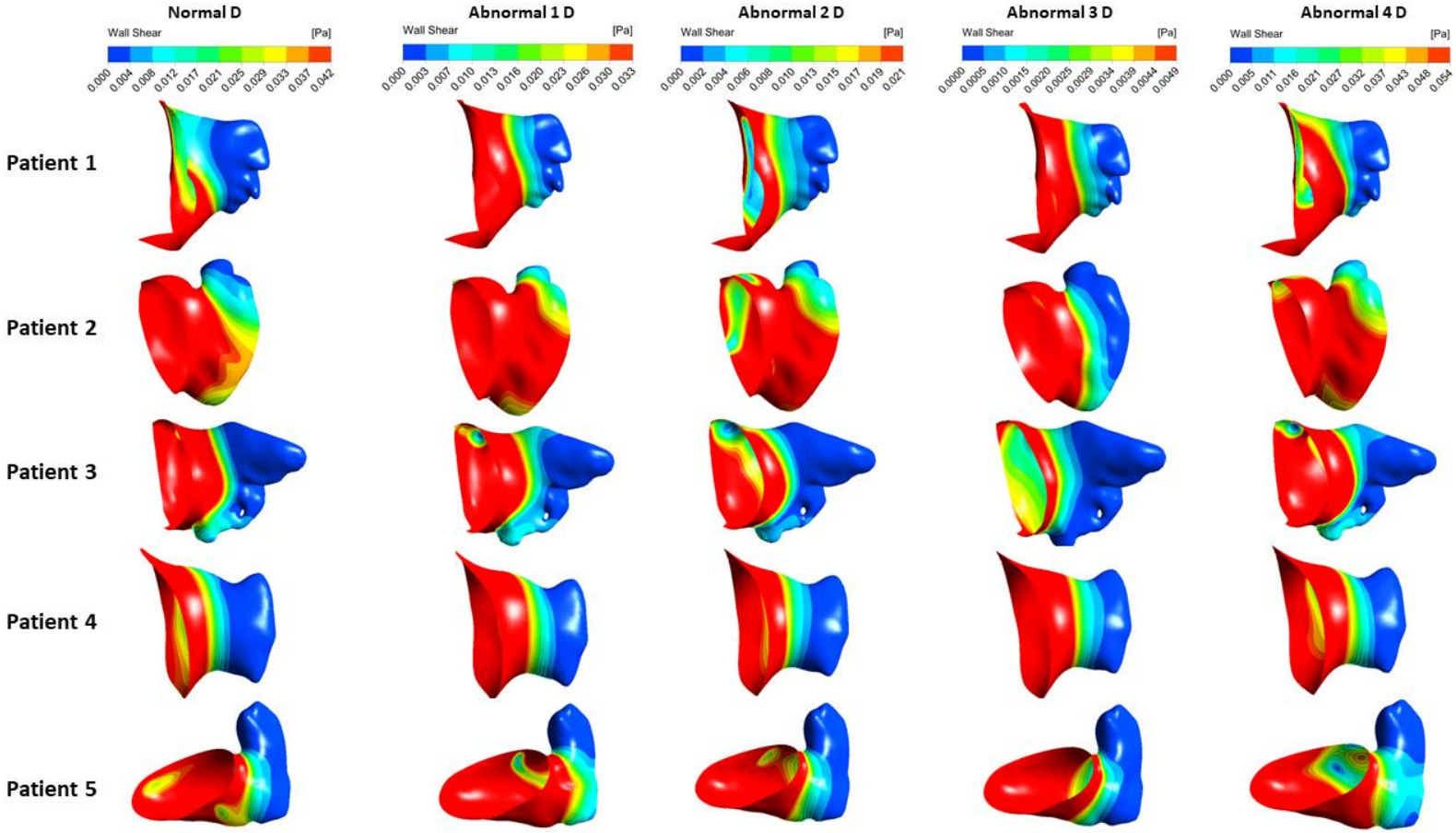

Figure. 10. LAA WSS alterations regarding the D wave (Patients 1-5).

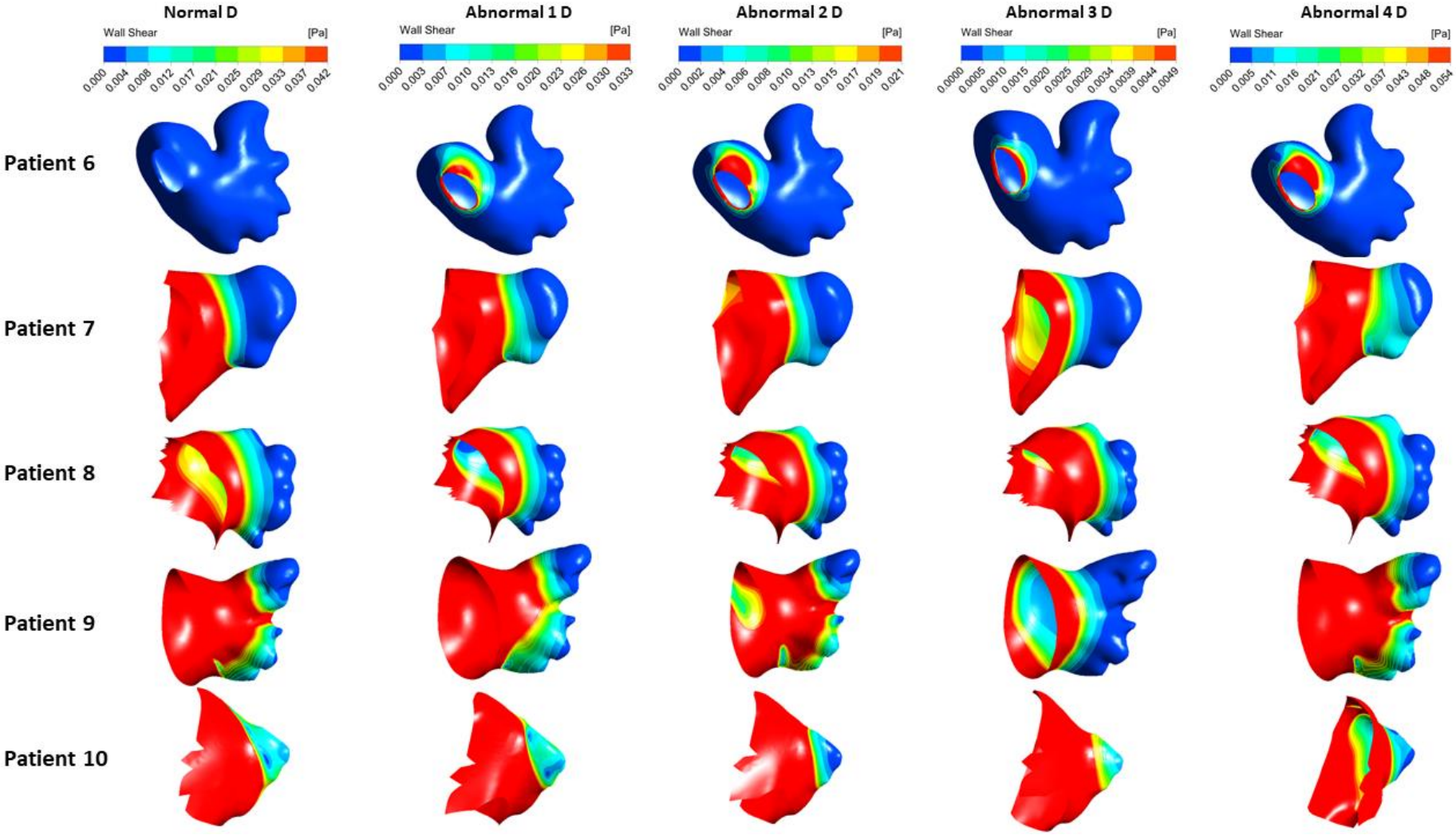

Figure. 11: LAA WSS alterations regarding the D wave (Patients 5-10).

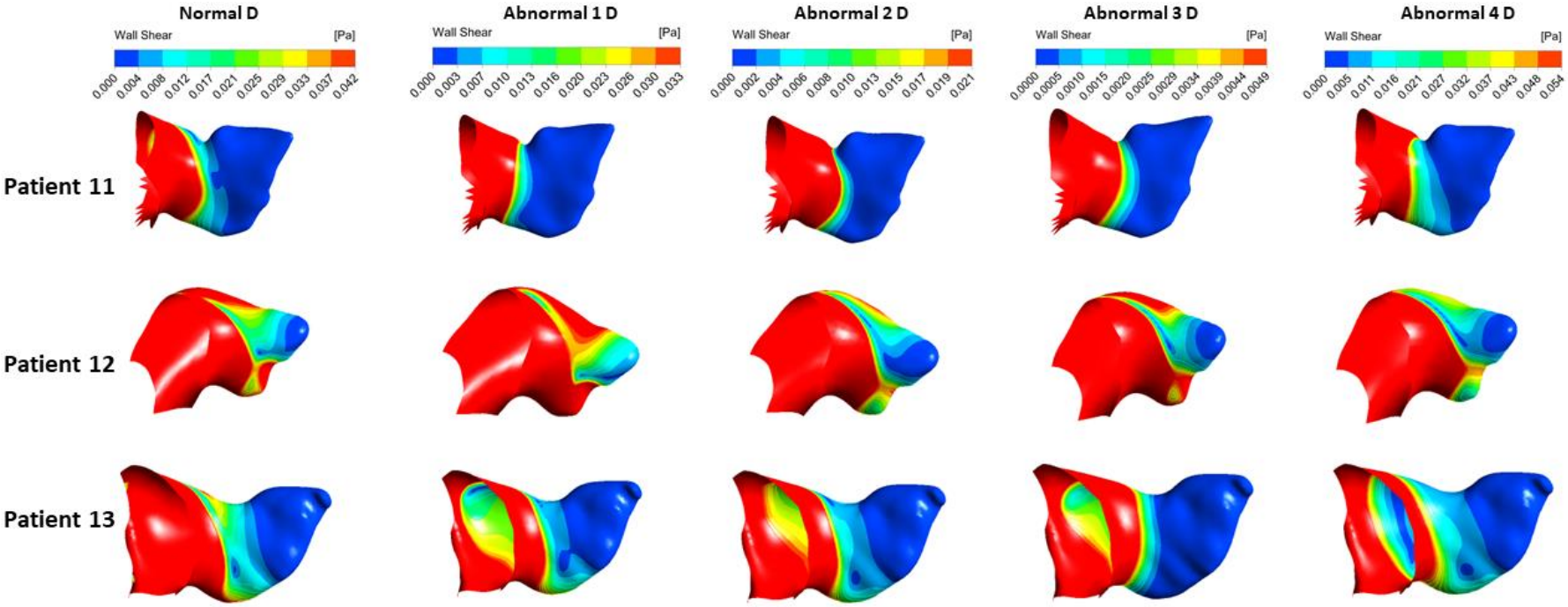

Figure. 12. LAA WSS alterations regarding the D wave (Patients 11-13).